A new design of an Electrochemical (bio)sensor: **High Aspect Ratio Fin-FET**

Serena Rollo

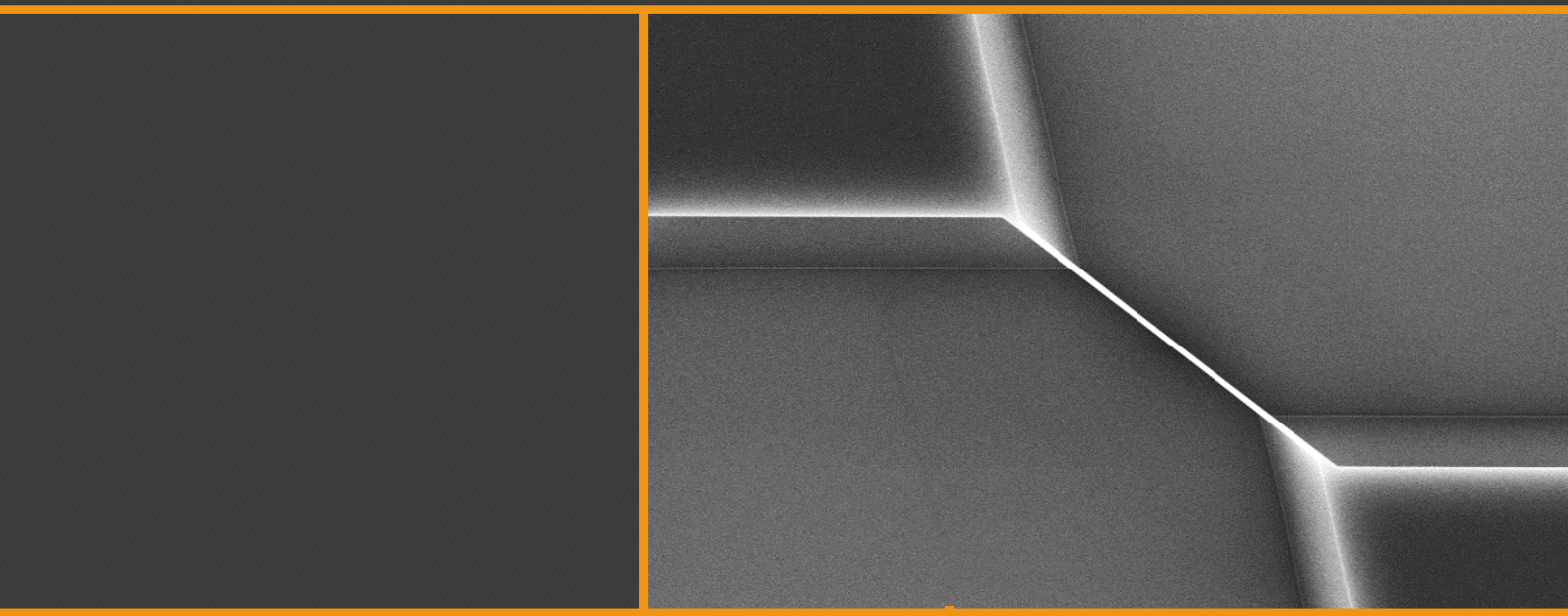

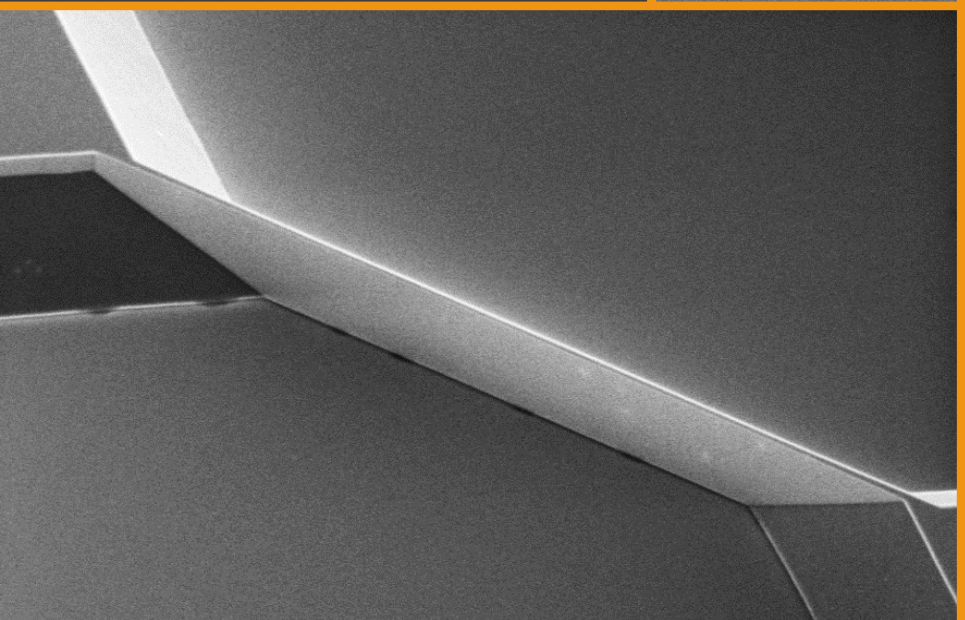

22/11/2019

A NEW DESIGN OF AN ELECTROCHEMICAL (BIO)SENSOR:

High Aspect Ratio Fin-FET

Serena Rollo

A NEW DESIGN OF AN ELECTROCHEMICAL (BIO)SENSOR: High Aspect Ratio Fin-FET

DISSERTATION

to obtain
the degree of doctor at the University of Twente,
on the authority of the rector magnificus,
prof.dr. T.T.M. Palstra,
on account of the decision of the graduation committee,
to be publicly defended
on Friday the 22 of November 2019 at 16.45 hours

by

Serena Rollo

born on the 30th June 1989
in Monopoli, Italy

This dissertation has been approved by:

Promotors:
Prof. Dr. W. Olthuis
Prof. Dr. Ir. A. van den Berg

Co-Promotor:
Dr. C. Pascual García

The research described in this thesis was carried out at the Luxembourg Institute of Science and Technology (LIST), Luxembourg, and the University of Twente, The Netherlands. This work was part of the project NANOpH financially supported by the Luxembourg National Research Fund (FNR) under the Attract program, fellowship number 5718158.

Title: A new design of an electrochemical (bio)sensor: High Aspect Ratio Fin-FET
Author: Serena Rollo
Cover design: Serena Rollo
Printed by:
ISBN: 978-90-365-4863-2
DOI: 10.3990/1.9789036548632
URL: https://doi.org/10.3990/1.9789036548632

Graduation Committee

Chairman: Prof. Dr. J.N. Kok

Members:
Prof. Dr. J. Schmitz
Prof. Dr. S.J.G. Lemay
Dr. P. Estrela
Prof. Dr. Y. Joseph

“There is nowhere you can be that isn’t where you’re meant to be.”

John Lennon

Contents

Chapter 1 Introduction.....11

1.1 Project aim and description.....11

1.2 Outline of thesis.....14

References.....16

Chapter 2 From planar FETs, to Silicon Nanowires to Fin-Field Effect Sensors.....18

2.1 Ion Sensitive Field Effect Transistors (ISFETs) and Silicon Nanowires FET sensors basics.....19

2.2 pH sensing principles and introduction to Bio-FETs.....25

2.2.1 pH sensing.....25

2.2.2 Introduction to Bio-FETs.....28

2.2.3 Limitations of biosensing.....30

2.3 High aspect ratio Fin-FETs.....31

References.....35

Chapter 3 High aspect ratio Fin-Ion Sensitive Field Effect Transistor: compromises toward better electrochemical biosensing.....39

3.1 Abstract.....40

3.2 Introduction.....40

3.3 Results and discussion.....43

3.3.1 Transfer characteristics of pH response.....46

3.3.2 Output characteristics of pH response.....49

3.3.3 Theoretical and experimental data correlation.....50

3.3.4 Drift and response time.....54

3.4 Conclusions.....57

References.....60

Supplementary Information.....65

Chapter 4 High Performance Fin-FET electrochemical sensors with high-K dielectric materials.....78

4.1 Abstract.....79

4.2 Introduction.....79

4.3 Experimental Methods.....84

4.3.1 Silicon Fin-FETs fabrication.....84

4.3.2 pH sensitivity characterization.....86

4.3.3 Measurements of acidity in citrus juices.....86

4.4 Results and discussion.....86

4.4.1 Surface sensitivity of Fin-FETs with SiO_2, Al_2O_3, HfO_2.....86

4.4.2 Relevance of Fin-FETs integration with high-k dielectrics 91

4.4.3 Stability of the oxides in different acidic media.....94

4.5 Conclusions.....96

References.....98

Supplementary Information.....103

Chapter 5 Single step fabrication of Silicon resistors on SOI substrate used as Thermistors.....107

5.1 Abstract.....108

5.2 Introduction.....108

5.3 Materials and methods.....110

5.3.1 Sample patterning.....111

5.3.2 TMAH wet etching 111

5.3.3 Calibration of the <110> silicon wet etching rates.....111

5.3.4 Ohmic contacts.....112

5.3.5 Electrical and Thermal characterization.....112

5.4 Results and discussion……113
5.4.1 Design and fabrication of differently shaped wires within a single process……113
5.4.2 Transport and temperature dependent performance of the silicon wires……118
5.5 Conclusions……120
References……122
Supplementary Information……125
Chapter 6 Conclusions and Outlook……129
6.1 Conclusions……129
6.2 Outlook on Biosensors Market……131
Contributions……133
Samenvatting……134
Appendix……136
Acknowledgements……139
Publications List……142

Chapter 1

INTRODUCTION

1.1 Project aim and description

This thesis entitled "A new design of an electrochemical (bio)sensor: high aspect ratio Fin-FET" was part of the project NANOpH financed by the Luxembourg National Research Fund (FNR). The research interest is motivated by the rapid growth of the fields of genomics[1,2] and proteomics[3,4] in which hospitals and private institutions are investing[5]. Label-free detection of DNA and its protein expression is a powerful tool for the study of diseases like cancer[6,7], drug discovery[8], and the development of therapies with the best outcomes considering the genetic differences among individuals[9]. Different kind of biosensors combining a bio recognition element and a transductor element exist, differing from the way the bio conjugation event is transduced by the sensor into a recognisable signal[10]. Among these, Bio-Field Effect Transistors (Bio-FETs) are a category where the transducing element is provided by the capacitance effect of a dielectric material in contact with an electrolyte[11]. The FET principle is supported by the fact that it is possible to choose the doping of the semiconductor substrate and fabricate the channel with dimensions which would result in the highest transconductance of the charge of the analyte to detect, improving the sensitivity[11,12]. Using the right molecules for the bio-recognition component they are able to detect biomarkers of interest at low concentrations[13,14]. Bio-FETs are able to cater small size, large multiplexing capabilities, label-free sensing, real-time detection depending on sensor configuration, and selectivity, all with the potential to reduce the costs of fabrication thanks to the well-established fabrication techniques from the electronic industry.

Despite all the appealing features there are issues to overcome when bringing Bio-FETs from the laboratory to the industry[11,15]. The high sensitivity and

shorter times for detection promised by nano Bio-FETs due to their geometry (efficiency at capturing diffusing molecules) and high surface to volume ratio comes at the expense of losing reliability of performance among devices, providing lower ratio of the signal to noise and difficulties to implement the functionalization of the bio recognition element. In this scenario, there is a pivotal challenge to solve related to the development of a FET sensor with sufficient sensitivity to detect (bio) molecules at their physiological concentrations that would be also reliable towards defects introduced by the fabrication and bio-functionalisation processes when scaled up and which would provide enough output signal to be easily readable by the measurement apparatus.

While the current prevailing approaches to deal with the challenge of reliability are the optimization of the fabrication methods and materials, this thesis tackles a modification of the FET design that considers the optimization of the whole process of sensing. Our research takes into account the development of a design for a new device geometry, as well as the optimization of the fabrication protocol and integration with dielectric materials providing chemical stability and high dielectric constants for an enhanced transconductance. In relation to the problems of signal to noise ratio and reliability, we considered a geometry allowing lower resistivity and thus enhanced output currents before and after the biorecognition event. We also considered the influence of the mass transport of analytes toward the sensor. The capture of molecules for sensing depends on the diffusion. As the molecules bind to the sensor a concentration gradient forms between the sensor surface and the bulk of the solution, and the steady signal is reached when the sensor surface is in equilibrium with the bulk concentration. New designs should consider the time that is needed to reach the equilibrium, which affects the duration of the assay, especially for slow diffusive molecules at low concentrations. Sensor designs profiting of the diffusion of the analyte in multiple directions are able to capture the necessary amount of molecules for detection more efficiently providing a faster response and reducing the time for the biological assay.

Considering the global picture of biosensing, in this work we propose a new FET design with a fin geometry for which we optimised the fabrication protocol resulting in reproducible devices with controlled dimensions where the width of the sensors could be tailored in a range from 100 nm to few micrometres. The developed configuration addresses the problems of signal to noise ratio, and reliability to fabrication and functionalization, without compromising much on the sensitivity and time of response offered by current nano devices. The particular geometry of the FET channel also benefits of an intrinsic improved linearity of the transduction with concentration when the linearity does not come from the dielectric used as sensing layer. Integration with high dielectric constant materials addresses the problem of chemical stability into the fluid environment and influences the transconductance through an enhancement of the capacitive effect.

The main topics covered by this thesis are:

1) Design, development and optimization of a fabrication protocol for silicon Fin-FETs using conventional cleanroom fabrication techniques resulting in reproducible devices.
2) Modelling of the electrochemical transduction of the chemical interaction at the dielectric sensing layer surface with protons into a variation of the conductance of the devices.
3) Investigation of different dielectric materials and their impact on sensors performance.

As another application of the developed devices we studied them as temperature sensors (silicon thermistors). In this thesis we show how to apply the fabrication protocol developed for the Fin-FETs on Silicon On Insulator substrates <110> oriented for the simultaneous fabrication of silicon thermistors with different shapes on a chip, and we study their dependence of the resistance on temperature. The possibility of tailoring the shape of the sensor during the fabrication to control the thermalization, and the possibility to combine temperature sensitive devices with electronic circuits are appealing features of silicon based thermometers, which can also be

monolithically integrated with other sensing components. Different shapes shares a different surface area with the surrounding and the substrate, affecting heat propagation. The proposed method allows the choice of the shape of the temperature sensor to better thermalize with the environment or the substrate and circuit, depending on the scope.

1.2 Outline of thesis

In chapter 2 I present a general review of the basics of FET electrochemical sensors focusing on planar Ion Sensitive Field Effect Transistors (ISFETs) and Silicon Nanowires (Si-NWs). I explain the principle of pH sensing and introduce Bio-FETs and the limitations in biosensing. I present the concept of Fin-FETs and their interesting features for applications as biosensors.

In Chapter 3 we approach the study of the Fin-FETs using them as pH sensors. I present the design and fabrication of such devices as well as an electrochemical model to describe their pH sensitivity as variation of the conductance with the proton concentration. I studied the sensitivity of the silicon oxide (SiO_2) sensing layer and the pH dependent output characteristics. I considered devices with different widths and comment about relative variation of the conductance with pH, and linearity. I fitted the experimental data with the developed electrochemical model and I compared theoretically the Fin-FETs with Si-NWs, as well as experimentally with data reported in literature. Finally I studied the response time of the devices to variation of proton concentration talking about diffusion.

In chapter 4 I explored different dielectrics, such as SiO_2, aluminium oxide (Al_2O_3) and hafnium oxide (HfO_2) as pH sensitive layer. I compared the pH sensitivity of such oxides and relate it to intrinsic material parameters. We comment on the influence of high-k dielectrics on the transconductance considering similar Fin-FETs devices with different materials. I studied the output characteristics of Fin-FETs with SiO_2 and HfO_2 at different pH and established the highest performances of HfO_2. I fitted the experimental data

with the developed electrochemical model as described in chapter 3 to extrapolate the dielectric constant of HfO_2. I used the devices as pH sensor in citric juices and comment on their chemical stability.

In chapter 5 I applied the study for the development of the fabrication protocol for the Fin-FETs to produce silicon resistors with different shapes which we tested as temperature sensors. First I studied the etching rates and etching profiles on Silicon On Insulator substrates <110> oriented depending on the mask position with respect to the primary flat of the wafer, and I used these information to fabricate resistors with rectangular and triangular cross section on the same substrate in a single wet etching process. I studied the temperature dependent variation of the resistance of the devices and established their accuracy. We comment on the influence of a different shape of the sensor on heat propagation and thermalization.

Chapter 6 gives a summary of the presented work and future research, and an outlook on the biosensors market.

References

1. https://www.grandviewresearch.com/industry-analysis/genomics-market
2. Lockhart, D.J.; Winzeler, E.A. Genomics, gene expression and DNA arrays, Nature, 405, 827-836, 2000
3. https://www.alliedmarketresearch.com/proteomics-market
4. Chandramouli, K.; Qian, P-Y. Proteomics: Challenges, Techniques and Possibilities to Overcome Biological Sample Complexity, Human Genomics & Proteomics, 2009
5. Stevens, R.; Yokoyama, S.; Wilson, A. Global Efforts in Structural Genomics, Science, 294 (5540), 89-92, 2001
6. Ladd, J.; Taylor, A.D.; Piliarik, M.; Homola, J.; Jiang, S. Label-free detection of cancer biomarker candidates using surface plasmon resonance imaging, Analytical and Bioanalytical Chemistry, 393 (4), 1157-1163, 2009
7. Stern, E.; Vacic, A.; Rajan, N.K.; Criscione, J.M.; Park, J.; Illic, B.R; Mooney, D.J.; Reed, M.A.; Fahmy, T.M. Label-free biomarker detection from whole blood, Nature Nanotechnology, 5 (2), 138-142, 2009
8. Xi, B.; Yu, N.; Wang, X.; Xu, X.; Abassi, Y.A. The application of cell-based label-free technology in drug discovery, Biotechnology Journal, 3, 484-495, 2008
9. Whirl-Carrillo, M.; McDonagh, E.M.; Hebert, J.M.; Gong, L.; Sangkuhl, K.; Thorn, C.F.; Altman, R.B.; Klein, T.E. Pharmacogenomics Knowledge for Personalizes Medicine, Clin. Pharmacol. Ther., 92 (4), 414-417, 2013
10. Mehrotra, P. Biosensors and their applications-A review, Journal of Oral Biology and Craniofacial Research, 6 (2), 153-159, 2016
11. Matsumoto, A.; Miyahara, Y. Current and emerging challenges of field effect transistor based bio-sensing, Nanoscale, 5 (22), 10702-10718, 2013
12. Tabata, M.; Goda, T.; Matsumoto, A.; Miyahara, Y. Field-Effect Transistors for Detection of Biomolecular Recognition, Intelligent

Nanosystems for Energy, Information and Biological Technologies, Spriger Japan, 13-25, 2016

13. Hahm, J.; Lieber, C.M. Direct Ultrasensitive Detection of DNA and DNA Sequence Variations Using Nanowire Nanosensors, Nano Letteres, 4 (1), 51-54, 2004
14. Kim, K.S.; Lee, H-S.; Yang, J-A.; Jo, M-H.; Hahn, K. The fabrication, characterization and application of aptamer-functionalized Si-nanowire FET biosensors, Nanotechnology, 20 (23), 2008
15. Scheller, F.W. et al. Future of Biosensors: A Personal View, Advances in Biochemical Engineering / Biotechnology, Springer, 2013

Chapter 2

FROM PLANAR FETS, TO SILICON NANOWIRES TO FIN-FIELD EFFECT SENSORS

This chapter reviews the basics of FET based electrochemical sensors focusing on planar Ion Sensitive Field Effect Transistors (ISFETs) and Silicon Nanowires (Si-NWs). I explain the pH sensing principle and discuss about Bio-FETs and the limitations in biosensing. At the end of the chapter I introduce the concept of Fin-FETs with the interesting features related to their geometry for applications as biosensors.

2.1 Ion Sensitive Field Effect Transistors (ISFETs) and Silicon Nanowires FET sensors basics

An Ion-Sensitive Field-Effect Transistor is a field-effect transistor used for measuring ions/molecules concentrations in solutions. The structure and principle of operation is similar to the Metal Oxide Semiconductor Field Effect Transistor (MOSFET) but the metal gate electrode is replaced by a solution in direct contact with the oxide. This electro-chemical device transduces the variation of charge close to the sensor surface resulting from a chemical reactions occurring at the gate in contact with the liquid into an electrical signal. In an ISFET, like in a MOSFET, the current flows between the source and drain contacts, and it is controlled by the gate voltage. To close the circuit a reference electrode immersed into the solution is used to bias the electrolyte. In a planar ISFET with a lightly p-type doped body (positively charged holes as majority carriers) and n-type source and drain contacts (negatively charged electrons has majority carriers) the application of a positive gate potential (V_{gs}) affects the positive holes under the oxide, creating a depleted region which is populated by negative fixed charges due to the ionized dopant atoms. When V_{gs} becomes higher than the threshold voltage (V_t) the depleted region with fixed negative charges can be populated by mobile electrons which contribute to the current in this negative inversion layer (I_{ds}) when a voltage is applied between the source and drain contacts (V_{ds}). In this configuration the current into the inversion channel depend on the V_{gs}. Figure 2.1 (a) shows a cross section of an ISFET device with the two source and drain contacts passivated with an insulating material to avoid the contact with the liquid, and the gate oxide in direct contact with the electrolyte biased through a reference electrode. Figure 2.1 (b) and (c) shows a plot of I_{ds} vs V_{gs} and I_{ds} vs V_{ds} respectively. The three regions of operation of a p-body type ISFET with n-doped contacts depending on the relative values of V_{gs}, V_t and V_{ds} are shown. When $V_{gs}<V_t$ there is no channel between the source and drain terminals, the device is OFF and no current is measured (the red shadowed part in fig. 2.1 (b)). This is called cut-off region. When $V_{gs}>V_t$

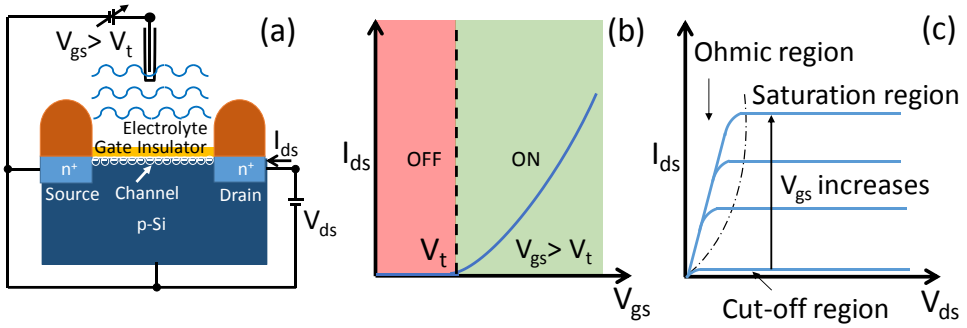

Figure 2.1 (a) Schematic of the cross section of an ISFET. The n-channel forms at the semiconductor/gate insulator interface upon application of a $V_{gs}>V_t$ and the current I_{ds} flows between the source and drain contacts. The gate insulator is in contact with the solution which is biased through a reference electrode. The contacts are passivated with an insulating material to avoid contact with the liquid. (b) Schematic of the I_{ds} vs V_{gs} curves at fixed V_{ds}. The device is initially off and there is no current flowing into the channel. When V_{gs} becomes higher that the threshold voltage the channel forms, the device is on, and the current flows between source and drain. (c) Schematic of the three regions of operation of the transistor depending on V_{ds} and V_{gs}.

the channel is formed beneath the oxide (the green shadowed part in fig. 2.1 (b)) and the device is now ON. For $V_{ds}<V_{gs}$ the device is in its constant resistance region, where the resistance is controlled by the gate voltage which influence the width of the channel. This is referred as the ohmic region and the current is given by eq. 2.1[1,2]:

$$I_{ds} = \frac{C_{ox}\mu W}{L}\{(V_{gs} - V_t) - 1/2V_{ds}\} \cdot V_{ds} \qquad \text{Eq.2.1}$$

Where C_{ox} is the gate insulator capacitance per unit area, μ is the mobility of the electrons in the inversion channel, and W and L are the width and length of the channel respectively. As V_{ds} increases the two electric field along the channel and perpendicular to it cause an accumulation of charges at the source and a diminution at the drain. This phenomenon is called pinch off. In this condition the current through the channel does not depend anymore on V_{ds} and the transistor is its constant current region (the saturation region in fig. 2.1 (c)). Contrary to a MOSFET where V_t is a constant determined by the materials properties and the presence of charges in the device, in an ISFET this parameter is also influenced by the presence of charges at the electrolyte/oxide interface. In both MOSFETs and ISFETs the gate potential at

which there is no electric field in the semiconductor is called flat band voltage (V_{FB}) and V_t depends on V_{FB} through eq. 2.2:

$$V_t = V_{FB} - \frac{Q_B}{C_{ox}} + 2\phi_F \quad \text{Eq.2.2}$$

Where Q_B is the fixed charge in the depleted region in the semiconductor body and ϕ_F is the fermi level.

In an ISFET V_{FB} can be expressed in terms of the interfaces between the solution and the reference electrode, and the solution and the oxide on one side, and the oxide and the semiconductor on the other side to keep the balance, so that there is no charge inside the semiconductor. The equation for the flat band voltage in an ISFET is given by eq.2.3:

$$V_{FB} = V_{ref} - \Psi_0 + \chi_{sol} - \frac{\phi_{si}}{q} - \frac{Q_{ss} - Q_{ox}}{C_{ox}} \quad \text{Eq.2.3}$$

Where V_{ref} represents the contribution of the reference electrode, χ_{sol} is the surface dipole potential of the solution, which is constant, ϕ_{Si} is the silicon electron work function and q is the elementary charge. Q_{SS} represents the fixed charges at the semiconductor surface and interfaces states, Q_{ox} represents fixed charges in the oxide, and C_{ox} represents the gate capacitance per unit area. All the above mentioned parameters can be considered constant in aqueous solutions except for the surface potential Ψ_0 which results from a chemical reaction of the oxide surface groups. It is this parameter that makes V_{FB} and thus V_t dependent on the analytes charge. Following eq. 2.1, 2.2 and 2.3 the variation of the surface potential $\Delta\Psi_0$ due to the analyte binding can be estimated directly from the shifting of V_t in the I_{ds} vs V_{gs} curves at constant V_{ds}.

Si-NWs electrochemical sensors also operate as field effect transistors since the current in the channel is affected by the gate voltage. Homogeneously doped Si-NWs consists of an either p-doped or n-doped channel connected to the two source and drain terminals. The typical configuration in Si-NWs differs from the ISFET heterojunction configuration by the fact that the FET

channel has the same kind of doping as the contacts. Thus, when no gate voltage is applied the current can flow between the source and drain contacts according to the ohmic law.

Usually they are fabricated on Silicon on Insulator (SOI) substrates in such a way that the silicon channel is isolated from the silicon substrate by a buried oxide (BOX) layer. Like in an ISFET the solution is in direct contact with the oxide and it is biased by a reference electrode. The voltage applied to the solution through the reference electrode is referred as V_{ref}. A schematic of a homogeneously doped p-type Si-NW is represented in fig. 2.2 (a). As in an ISFET a voltage between the source and drain contacts passivated with an insulating material is applied, and the current in the channel is measured. Similarly to the previously described ISFETs, chemical sensing is achieved when there is a change of the potential at the oxide surface ($\Delta\Psi_0$) deriving from a chemical interaction which is transduced through a capacitive effect of the dielectric. In a p-type Si-NW channel where the majority carriers are positively charged, a positive or negative change of surface potential will result in a repelling or attractive field for the carriers, respectively. Therefore the cross section (S) of the channel available to the conduction will shrink or open depending on $\Delta\Psi_0$, affecting the conductance. Figure 2.2 (b) shows a cross-section of a p-type device like the one schematised in fig. 2.2 (a). When the voltages applied at the reference electrode and between the two contacts are kept constant, the current through the channel is modulated by the surface potential. Starting from the condition where the channel is completely open (at the surface potential Ψ_s) upon a positive change $\Delta\Psi_0$ the positive carriers in the semiconductor experience a repelling field which pushes them far from the interface with the dielectric reducing the conducting cross section and therefore the current passing through the channel. The area depleted of majority carriers (W_D) in the semiconductor is called depletion region W_D and it is represented in yellow. On the other side, a negative $\Delta\Psi_0$ will cause an accumulation of the positive carriers at the semiconductor/dielectric interface. In this case the conductance will be the

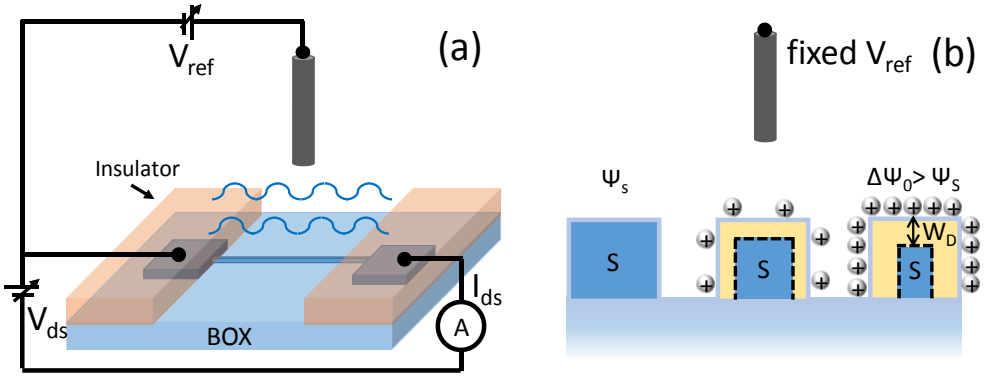

Figure 2.2 (a) Schematic of a Si-NW. The channel stands on the buried oxide (BOX) and it extends between the two contacts which are passivated through an insulating material. The current in the wire is measured upon application of a voltage between source and drain (V_{ds}). The solution is biased through a reference electrode (V_{ref}) (b) Schematic of the effect of a change in the surface potential $\Delta\Psi_0$ on the cross section available for the conduction in a p-doped channel. A positive $\Delta\Psi_0$ causes a reduction of the dimensions of the channel due to the repelling field experienced by the positive carriers, compared to the situation where the channel is completely open at Ψ_s. The depleted area in the semiconductor is called depletion region W_D, depicted in yellow.

sum of the channel conductance and the accumulation layer conductance[3]. When the device operates in the depletion mode analytes can be sensed by the effect that their charge produces on the depletion region and therefore on the dimensions of the channel. The transduction involves a capacitive effect through the dielectric material. In depletion mode of operation, other than from the surface potential Ψ_0 the depletion region (thus the conductance) of the wires depends also on the doping density of the semiconductor substrate (N_A) and the device dimensions, and the thickness, reactivity of the surface and dielectric constant of the dielectric layer (t_{ox}, ε_{ox}). In a wire with a squared cross section the variation of the conductance upon a change of the concentration of the analyte can be expressed depending on the dimensions of the channel decreased by the depleted region, and thus according to the ohmic law as in eq. 2.4:

$$\Delta G = \frac{1}{\Delta R} = \frac{q\mu N_A}{L}\Delta S = \frac{q\mu N_A}{L}(w - 2W_D(\Psi_0, N_A, t_{ox}, \varepsilon_{ox}))(h - W_D(\Psi_0, N_A, t_{ox}, \varepsilon_{ox})) \qquad \text{Eq.2.4}$$

Where q and μ represent the elementary charge and the mobility of the carriers respectively. The product $q\mu N_A$ represents the conductivity of the FET

channel. W, h and L are the width, height and length of the conducting channel respectively. The two terms in brackets refers to the variation of the cross section actually available to the conduction upon a change of the depletion width induced by the analyte. An expression for W_D can be obtained considering the electrostatic coupling of the Si-NW interface with the electrolyte, which is influence by the chemical activity on the gate surface. A detailed expression depending on the fabrication parameters of doping density of the silicon substrate, thickness and dielectric constant of the dielectric material and surface potential Ψ_0 will be described in the supporting information of chapter 3.

From eq. 2.4 it is possible to obtain the optimum fabrication parameters to optimise the sensitivity in a given dynamic range. This sensitivity in Si-NWs devices working in depletion is maximized fabricating devices with a channel width to achieve full depletion in the dynamic range of the measurement (w=2W_D). On the other side, as per eq. 2.1 to 2.3, a planar ISFET in the constant current operation, directly detect the variation of the surface potential from the shifting of the I_{ds} vs V_{gs} curves.

Like ISFETs, where changes of the surface potential affect the threshold voltage of the device (eq. 2.2 and 2.3), Si-NWs chemical sensors transduce the variation of charges at the dielectric surface by their effect on the depletion width, and thus by the change in conductance produced by the change in the dimensions of the channel (eq.2.4). Both planar ISFETs or Si-NWs can be configured as biosensors by functionalizing the gate dielectric with receptors for the biomarkers of interest (small molecules, DNA, proteins…). In both cases the $\Delta\Psi_0$ coming from the receptor-analyte binding will result in an output electrical signal dependent upon $\Delta\Psi_0$, enabling the sensing.

2.2 pH sensing principles and introduction to Bio-FETs

Recent years have seen the deployment of FET type sensors for sensing biomolecules like peptides and proteins, and nucleic acids (DNA and RNA). In biosensing functionalization with bio receptors is essential for a selective sensing, which is the ability of discriminating the target analyte among all the substances which may be present in a complex mixture . The binding of a charged analyte to its receptor functionalized at the dielectric surface results in detectable effect on the threshold voltage or the conductance in planar FETs and Si-NWs respectively, allowing the sensing. This binding phenomenon is analogous to changing the applied voltage to the gate. In the following sections I first revise the mechanism of pH sensing as simple case of ion sensing, then I introduce Bio-FETs and the limitations in biosensing.

2.2.1 pH sensing

In an ISFET-type sensor the oxide is in direct contact with the electrolyte which is biased through a reference electrode immersed in the solution. The gate oxide, for example SiO_2, has silanol groups (Si-OH) on its surface which are exposed to the liquid and can be neutral, positively charged (protonated) or negatively charged (deprotonated) depending on the pH behaving in an amphoteric way as illustrated by the following reactions occurring at the oxide/electrolyte interface:

$$\text{—Si–OH} + H_2O \leftrightarrow \text{—Si–O}^- + H_3O^+ \quad (K_a)$$

$$\text{—Si–OH}_2^+ + H_2O \leftrightarrow \text{—Si–OH} + H_3O^+ \quad (K_b)$$

At each of these reactions correspond a dissociation constant (acid dissociation constant K_a, basic dissociation constant K_b) which indicates the probability of the surface groups to take or lose a proton. Each dielectric material is characterized also by a certain number of reactive groups, or sites, on its surface (N_s) which depends on its chemical composition. Figure 2.3 (a) shows a schematic of the dielectric/electrolyte interface considering silicon

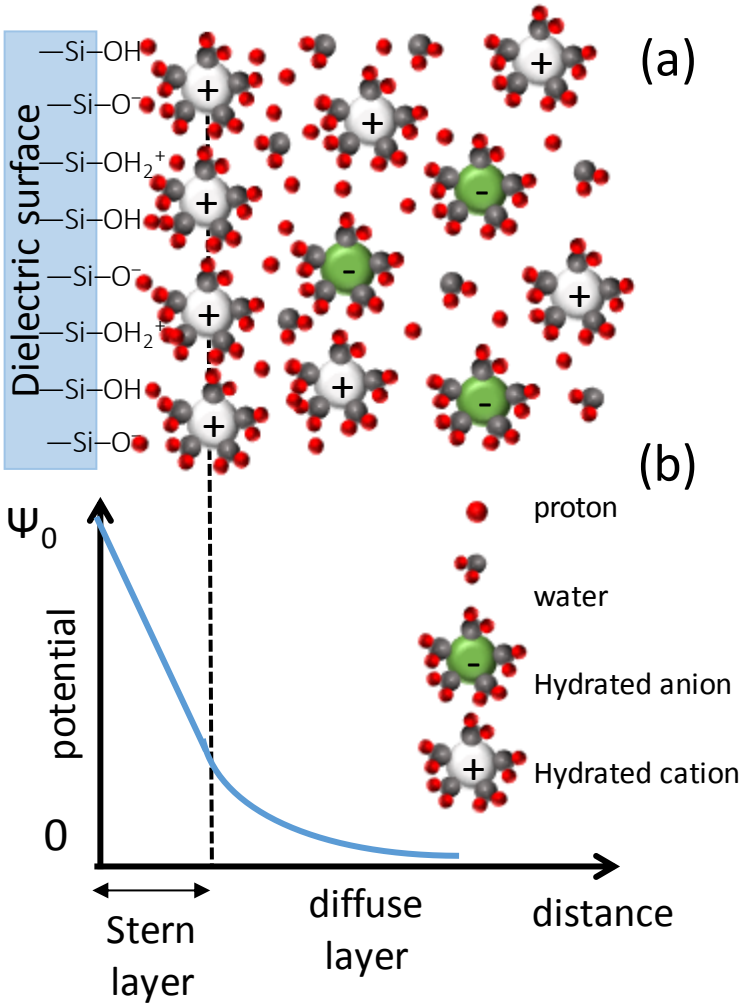

Figure 2.3 (a) Schematic of the GCS model. The dielectric surface has a certain charge due to protonation and deprotonation of the reactive surface sites which attracts ions of opposite charge in the solution. The layer of ions closest to the surface forms the Stern layer. Further the other ions in the solution form a diffuse layer to neutralize the charge at the dielectric surface. (b) Potential distribution from the dielectric surface to the bulk of the electrolyte. The biggest drop of potential happens in the Stern layer. Further the potential decreases exponentially until 0 in the bulk.

oxide. The interaction between the dielectric surface and the ions in the liquid can be described by the Site Binding (SB) model[4] which uses the dissociation constants and the surface density (number of sites/area) of reactive sites on the oxide surface to describe the grade of ionization (protonation or

deprotonation) of the surface chemical groups of the dielectric barrier. This surface response can be linked to the electrolyte through the Gouy-Chapman

$$\frac{\partial \Psi_0}{\partial pH_B} = -2.303 \frac{kT}{q} \alpha \qquad \text{Eq.2.5}$$

Stern model[5] which describes the electrical double layer that forms into the electrolyte. Ions are attracted to the charged dielectric surface forming a compact layer in equilibrium with the surface called as Stern layer. Further a diffuse layer is formed to neutralize the charge at the dielectric surface. The voltage difference between the dielectric surface and the bulk is referred to as the surface potential Ψ_0. As shown in fig. 2.3 (b) as we leave the surface, the potential drops off roughly linearly in the Stern layer and then exponentially through the diffuse layer, approaching zero in the bulk. The combination of the Site Binding model with the Gouy-Chapman-Stern model leads to a relationship between the bulk pH (pH_B) and the potential at the oxide/electrolyte interface Ψ_0:

$$\alpha = \frac{1}{\frac{2.303kTC_{diff}}{q^2 \beta_{int}} + 1} \qquad \text{Eq.2.6}$$

Where k, T and q represent the Boltzmann constant, absolute temperature and elementary charge respectively. α is a dimensionless sensitivity parameter with a value between 0 and 1 which depends on the intrinsic buffer capacity of the oxide (β_{int}) and the double layer capacitance C_{diff}. β_{int} is linked to the ability of the oxide to buffer small changes of surface charge and depends on K_a, K_b, and N_s, C_{diff} is linked to the ability of the electrolyte to adjust to variations of the surface potential and it depends on the solvent and ionic strength[5]. Small values of C_{diff} and high values β_{int} are related to higher sensitivities. In ideal conditions of α=1, the sensor shows the so-called nernstian sensitivity of -59.2 mV/pH at 298 K (25 °C). The surface potential change per unit variation of the pH is related to the dielectric properties through the sensitivity parameter α. Despite its easy fabrication, silicon oxide has drawbacks such as poor buffer capacity, as well as susceptibility to

leakage currents and drift[6,7] compared to dielectric materials with higher dielectric constant (k) such as aluminium oxide (Al_2O_3), and hafnium oxide (HfO_2). Using high-k dielectrics reduces leakage currents and improve the gate capacitance, thus the transconductance. Silicon oxide typically shows pH sensitivities of 20 to 40 mV/pH[8,9] depending on the quality of the grown layer, and a nonlinear response in a wider pH range due to its low intrinsic buffer capacity at acidic pH, close to the point of zero charge (pH_{pzc}). On the other end, the above mentioned Al_2O_3 and HfO_2 have shown sensitivities equal or higher than 55 mV/pH, and an improved linear variation of the surface potential with the pH in wide pH range[3,10,11].

2.2.2 Introduction to Bio-FETs

ISFETs were introduced as the first miniaturized silicon based electrochemical sensors for proton concentration sensing[12]. Over the time, variations on the ISFET have been developed to allow the detection of different analytes. The general term used to address such variations is Bio-FET. A more accurate classification is made upon the functionalization of the dielectric with the bio recognition element used for detection. Examples of Bio-FET are CHEMFETs, DNA-FETs, ImmunoFET, Enzyme FETs (ENFETs) and Cell based BioFETs[13,14]. CHEMFETs can sense other ions than protons. Unlike pH sensing, where bare dielectric surfaces are used for direct detection, sensing of other species such as Ca^{2+}, K^+, Na^+, Cl^- and heavy-metal ions requires functionalization with an ion-reactive or ion selective layer to impact selectivity. DNA-FET are used in applications where DNA or related molecules are involved. When DNA strands bind to the complementary ones functionalized at the dielectric surface, changes in the gate potential occur due to the negative charge of DNA, thereby allowing label-free detection of DNA. Limits of detection for these kind of modified planar FETs are in the range of few tenths of micromolar[15,16]. An immune-ISFET is composed of an antibody coated onto the gate material recognizing its antigen. ENFETs are based on the principle of pH-sensitive ISFETs where the detected concentration of hydrogen ions during an enzymatic reaction is proportional to the analyte. Numerous

species have been sensed in this way (glucose[17], penicillin[18], urea[19]). Cell-based sensors systems have been considered for biomedical and pharmacological applications with attention to integrating living cells with silicon-based FET devices. Main fields of application regard exploring neuronal network and transmission paths of ionic channels in the cells membrane. Over the last few decades the interest in nano Bio-FETs has evolved, including nanowires, nanoribbons and nanoplates[20-22]. These devices share with their planar ancestors characteristics such us compatibility with Complementary Metal Oxide Semiconductor (CMOS) fabrication processes, multiplexing, possibility of functionalization. The research interest has been mainly driven by the improved current sensitivity ($\Delta I/I$) upon binding and unbinding events compared to planar FETs due to the large surface area-to-volume ratio, which allows to decrease the limits of detection from few tens of micromolar to femtomolar[23,24]. However, when measuring low concentrations of samples the characteristic that determine the smallest resolvable ΔI is the current noise of the sensor (δi) and smaller devices may not be the better choice[25,26,27]. Considering the number fluctuation model the signal to noise ratio ($\Delta I/\delta i$) has been reported in the following form[28]:

$$SRN \propto \frac{CONSTANT\ x\ \Delta Q}{\sqrt{A}} \qquad \text{Eq.2.7}$$

Where Q and A represent the charge binding on the surface and the surface area of the sensor respectively. For common diagnostic applications of determination of the concentration of a certain analyte the probability of binding (ΔQ on the sensor surface) scales linearly with the surface area available, therefore larger area devices would be desirable. Indeed, noise studies of pH measurement performance have demonstrated the advantage of larger area devices[28]. From a device perspective the detection limit is determined by the device noise, however the detection limit of the entire system depends also on the rate of the diffusion of the analyte to the surface and the affinity of the analyte/receptor interaction, which set the lower bound of the dynamic range of the sensor where information on analyte concentration can be extracted from the signal change at equilibrium[29,30].

Nano biosensors offer advantages compared to planar Bio-FETs for detecting lower concentrations, down to femto/picomolar, as demonstrated for detection of DNA hybridization and proteins in low ionic strength buffers[23,24,31,32] due to the 2D diffusion of the analyte towards the sensor which allows the sensor to collect in a shorter time to amount of molecules which are necessary to the signal.

2.2.3 Limitations of biosensing

In the previous paragraph I mentioned the signal to noise ratio as one of the limitations of nano Bio-FETs to determine the minimum detectable variation of the output signal and thus the limit of detection. But this is not the only issue. When it comes to clinical application of Bio-FET sensors a limitation is represented by the Debye screening length, which refers to the effect of screening of the charged analyte by dissolved ions in the solution. The Debye screening length depends on the ionic strength of the electrolyte varying from less than 1 nm to 10 nm from 1M to 1mM. Since biomolecular interaction events usually occur beyond 10 nm from the gate surface (the length of the attached probe) this effect represents a drawback for medical applications[33,34]. Most of the biological samples are highly concentrated which reduces the Debye length even further. The solution normally implemented is the reduction of the ionic strength of the sample to extend the Debye length which requires complex procedures and may affect the stability and activity of biological species. Another issue regards the non-specific binding. Very few studies have been directed to the detection of biomarkers directly into blood or serum because of the complexity of these media in which different components (cells, proteins, salts) interacting among each other are present, and the exact composition in unknown. Passivation of the sensor surface[35] and integration of microfluidic filters chip[36] have been explored as solutions to the issue. A limitation is also represented by the time for the assay. When the analyte binds to the sensor surface a concentration gradient forms into the solution and the analytes further from the sensor must travel though the concentration gradient to

interact with the bioreceptors functionalized on the sensor surface. The steady state signal is provided after a certain concentration at the sensor surface, sufficient to provide a readable signal, has reacted and the equilibrium with the solution is reached. Theoretical studies supported by experimental results have shown that the time needed to reach the equilibrium and read a signal depends on sensor dimensionality[29,37]. Nano wires provide faster response since they can sense molecules coming from the two dimensions parallel and perpendicular to the sensor surface, while planar FET can only collect molecules diffusing parallel to their surface.

2.3 High aspect ratio Fin-FETs

As discussed, nano biosensors can provide higher sensitivity linked to their high surface/volume ratio and to their dimensionality that reduces the time for the assay. Also, the limitation of signal to noise ratio in nano devices has been discussed; due to their small dimensions NWs usually show high resistances resulting in low currents to be measured, which are difficult to attribute to the analyte binding to its receptor rather than fluctuations coming from the electrolyte environment or the device itself. I also presented an expression of the signal to noise dependent on the charge of the analyte to detect and the surface area of the sensor. For those applications where it is needed to sense low concentrations rather than single molecule devices with a big surface area are preferable. A bigger area is also easier to functionalize and a higher number of bio receptors could be immobilized increasing the probability of binding of the analyte to the sensor. In this work I introduce a high aspect ratio configuration of Fin-FET sensors fabricated on <110> oriented Silicon On Insulator (SOI) substrates. Figure 2.4 (a) and (b) show Scanning Electron Microscope (SEM) pictures of a fabricated device and a schematic of the cross section representing the simplest case where the p-type silicon body is surrounded by a SiO_2 sensing layer. The dimensions of the fabricated devices are also reported where w and h represent the widths and

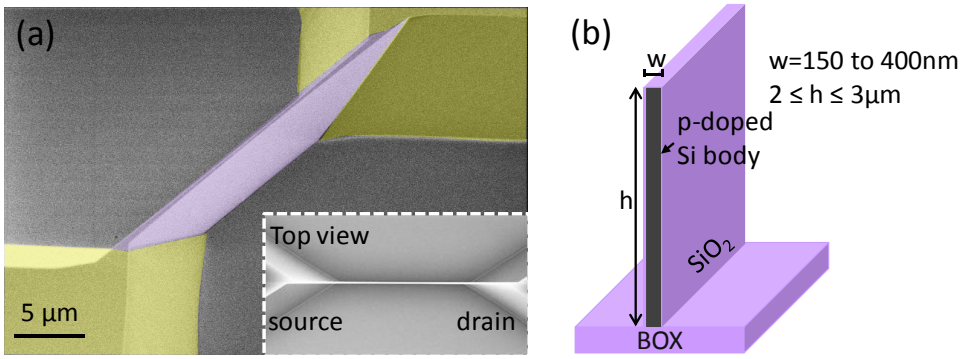

Figure 2.4 (a) SEM pictures of a Fin-FET device. The fin body standing on the buried oxide is shadowed in violet, the contacts are shadowed in yellow. The inset shows a top view with the 2D channel standing between the source and drain contacts. (b) Schematic of a cross section of a device with a p-doped body channel and with SiO_2 as sensing layer. The typical dimension of width (w) and height (h) of the fabricated devices are reported.

heights respectively. In the SEM images it is possible to see the thin fin coloured in violet standing on the buried oxide between the source and drain contacts coloured in yellow. The inset in fig. 2.4 (a) shows a top view of the fin. As can be noticed the Fin-FETs have a high surface area available for functionalization with bioreceptors while occupying the same footprint as nanowires. Their 2D channel configuration improves the total cross sectional area available to the conduction and thus higher currents are measured improving the signal to noise ratio. The 2D geometry can make them efficient at capturing the analytes from the two dimensions parallel and perpendicular to the substrate with reduced time for the assays. No data are reported in literature where such kind of devices are deployed as biosensors. Therefore we tried to place our Fin-FETs in the current Bio-FETs sensors scenario by collecting literature data of DNA sensing which we report in fig. 2.5 as time of the biological assay versus the concentration of detected DNA. We restricted the study to planar and Si-NWs Bio-FETs. The ranges of concentrations detectable through the two sensors configuration are shadowed in blue and orange for the planar FETs and nanowires respectively. References are reported in Table 2.1 for the planar FETs and nanowires. We observe that planar FETs take a longer time for the detection at any concentration, which

Table 2.1. Reference papers on DNA sensing for nanowires and planar FETs as reported in fig.2.5.

Sensor type		References
Nanowires FETs	Single	Adam and Hashim 2015; Duan et al. 2012; Gao et al. 2012; Hahm and Lieber 2004; Li et al. 2004; Lin et al. 2009; Zheng et al. 2010
	NW arrays	Lu et al. 2014; Zhang et al. 2015
Planar FETs		Braeken et al. 2008; Freeman et al. 2007; Sakata et al. 2005; Shin et al. 2004; Uno et al. 2007; Xu et al. 2016; Zafar et al. 2018; Zayats et al. 2006

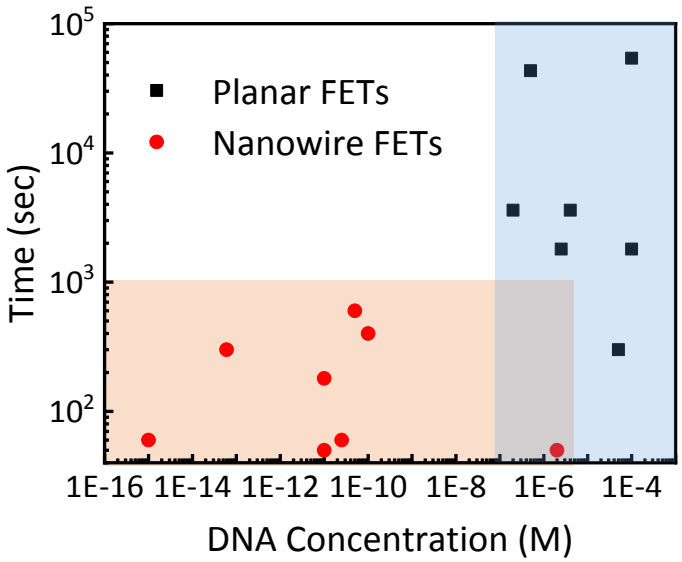

Figure 2.5 Data from literature of DNA sensing using planar FETs and Si-NWs FETs. The time needed for detection is reported versus the DNA concentration.

we attribute to their low dimensionality (1D diffusion towards the sensor). Few studies have been reported for planar FETs detecting concentrations lower than micromolar. On the other side nanowires provide faster response and lower limit of detection which can be attributed to their higher dimensionality according to the theory explained by Nair et al[29,30]. We believe that in this scenario the Fin-FETs would stand in the middle, performing more

like nanowires at low concentrations taking advantage of the 2D dimensionality. Fin-FETs devices may represent a good compromise between planar FETs and NWs in terms of signal to noise ratio, footprint, reliability, limits of detection and time for the assay for applications as biosensors.

References

1. Pao, H.C.; Sah, C.T. Effect of diffusion current on characteristics of metal-oxide (insulator)-semiconductor transistors, Solid State Electronics, 9, 927-937, 1966.
2. Bergveld, P. The operation of an ISFET as an electronic device, Sensors and Actuators, 1, 17-29, 1981.
3. Chen, S.; Bomer, J.; Carlen, E.T.; Van der Berg, A. Al_2O_3/Silicon NanoISFET with Near Ideal Nernstian Response, Nano Lett., 2011, 11, 2334-2341
4. Yates, D.E.; Levine, S.; Healy, T. Site-binding model of the electrical double layer at the oxide/water interface, Journal of the Chemical Society, Faraday Transactions 1, 70, 1807-1818, 1974
5. Van Hal, R.E.G.; Eijkel, J.C.T.; Bergveld, P. A general model to describe the electrostatic potential at the electrolyte oxide interfaces, Advances in Colloid and Interface Science, 69, 31-62, 1996
6. Park, I.; Li, Z.; Pisano, A.P.; Williams, R.S. Top-down fabricated silicon nanowire sensors for real-time chemical detection, Nanotechnology, 21, 2010
7. Kum, S.; Kwon, D.W.; Kim, S.; Lee, R.; Kim, T-H.; Mo, H-S.; Kim, D.H.; Park, B.G. Analysis of current drift on p-channel pH-sensitive SiNW ISFET y capacitance measurement, Current Applied Physics, 18, 568-574, 2018
8. Kim, S. et all, Silicon nanowire ion sensitive field effect transistor with integrated Ag/AgCl electrode: pH sensing and noise characteristics, *Analyst*, 136, 5012, 2011
9. Chen, S.; Bomer, J.; Van der Wiel, W.; Carlen, E.T.; Van der Berg, A. Top-Down Fabrication of Sub-30 nm Monocrystalline Silicon Nanowires Using Conventional Microfabrication, ACS Nano, 3 (11), 3485-3492, 2009
10. Dorvel, B.R.; Reddy, B.; Go, J.; Guevara, C.D.; Salm, E.; Alam, M.A.; Bashir, R. Silicon Nanowires with High-k Hafnium Oxide Dielectrics for

Sensitive Detection of Small Nucleic Acid Oligomers, ACS Nano, 2012, 6(7), 6150-6164

11. Bedner, K. et all, pH Response of Silicon Nanowire Sensors: Impact of Nanowire Width and Gate Oxide, Sensors and Materials, 2013, 25 (8), 567-576
12. Bergveld, P. Thirty years of ISFETOLOGY. What happened in the past 30 years and what may happen in the next 30 years, Sensors and Actuators B, 88, 1-20, 2003
13. Schoning, M.J.; Poghossian, A. Bio FEDs (Field-Effect Devices): State-of-the-Art and New Directions, Electroanalysis, 18, 19-20, 1893-1900, 2006
14. Lazcka, O.; Del Campo, F.J.; Munoz, X.F. Pathogen detection: A perspective of traditional methods and biosensors, Biosensors and Bioelectronics, 22, 1205-1217, 2007
15. Uno, T.; Tabata, H.; Kawai, T. Peptide-Nucleic Acid Modified Ion-Sensitive Field-Effect Transistor-Based Biosensor for Direct Detection of DNA Hybridization, Analytical Chemistry, 79 (1), 52-59, 2007
16. Mahdavi, M.; Samaeian, A.; Hajmirzaheydarali, M.; Shahmohammadi, M.; Mohajerzadeh, S.; Malboobi, M.A. Label-free detection of DNA hybridization using a porous poly-Si ion-sensitive field effect transistor, The journal of the Royal Society of Chemistry Advances, 4, 36854-36862, 2014
17. Park, K-Y.; Choy, S-B.; Lee, M.; Sohn, B-K.; Choi, S-Y. ISFET glucose sensor system with fast recovery characteristics by employing electrolysis, Sensors and Actuators B, 83, 90-97, 2002
18. Poghossian, A.; Schoning, M.J.; Schroth, P.; Simonis, A.; Luth, H. An ISFET penicillin sensor with high sensitivity, low detection limit and long lifetime, Sensors and Actuators B, 76, 519-526, 2001
19. Soldatkin, A.P.; Montoriol, J.; Sant, W.; Martelet, C.; Jaffrezic-Renault, N. A novel urea sensitive biosensor with extended dynamic range based on recombinant urease and ISFETs, Biosensors and Bioelectronics, 19, 131-135, 2003

20. Lee, M.; Lucero, A. One-dimensional Nnaomaterials for Field Effect Transistor (FET) Type Biosensor Applications, TRANSACTIONS ON ELECTRICAL AND ELECTRONIC MATERIALS, 13 (4), 165-170, 2012
21. Li, Z.; Chen, Y.; Li, X.; Kamins, T.I.; Nauka, K.; Williams, R.S. Sequence-Specific Label-Free DNA Sensors Based on Silicon Nanowires, Nano Letters, 4 (2), 245-247, 2004
22. Hahm, J.; Lieber, C.M. Direct Ultrasensitive Electrical Detection of DNA and DNA Sequence Variations Using Nanowires Nanosensors, Nano Letters, 4 (1), 51-54, 2004
23. Gao, A.; Lu, N.; Dai, P.; Li, T.; Pei, H.; Gao, X.; Gong, Y.; Wang, Y.; Fan, C. Silicon-Nanowire-Based CMOS-compatible Field-Effect-Transistor Nanosensors for Ultrasensitive Electrical Detection of Nucleic Acids, Nano Letters, 11, 3974-3978, 2011
24. Tian, R.; Regonda, S.; Gao, J.; Liu, Y.; Hu, W. Ultrasensitive protein detection using lithographically defined Si multi-nanowire field effect transistors, Lab on a Chip, 11, 1952-1961, 2011
25. Bedner, k. et al. Investigation of the dominant 1/f noise source in silicon nanowire sensors, Sensors and Actuators B, 191, 270-275, 2014
26. Deen, M.J.; Shinwari, M.W.; Ranuarez, J.C.; Landheer, D. Noise considerations in field-effect biosensors, Journal of Applied Physics, 100, 074703, 2006
27. Rajan, N.K.; Routenberg, D.A.; Chen, J.; Reed, M.A. 1/f Noise of Silicon Nanowire BioFETs, IEEE ELECTRON DEVICE LETTERS, 31 (6), 615-617, 2010
28. Mu, L.; Chang, Y.; Sawtelle, S.D.; Wipf, M.; Duan, X.; Reed, M. Silicon Nanowire Field-Effect Transistors- A versatile Class of Potentiometric Nanobiosensors, IEEE Acces, 3, 287-302, 2015
29. Nair, P.R.; Alam, M.A. Performance limits of nanobiosensors, Applied Physics Letters, 88, 233120, 2006
30. Nair, P.R.; Alam, M.A. Dimensionally Frustrated Diffusion towards Fractal Adsorbers, Physical Review Letters, 99, 256101, 2007

31. Li, B.R.; Hsieh, Y-J.; Chen, Y-X.; Chung, Y-T.; Pan, C-Y.; Chen, Y-T. An Ultrasensitive Nanowire-Transistor Biosensor for Detecting Dopamine Release from Living PC12 Cells under Hypoxic Stimulation, JACS, 135, 16034-16037, 2013
32. Luo, X.; Lee, I.; Huang, J.; Yun, M.; Cui, X.T. Ultrasensitive protein detection using aptamer-functionalized single polyaniline nanowire, Chemical Communications, 47, 6368-6370, 2011
33. Chu, C-H. et al. Beyond the Debye length in high ionic strength solution: direct protein detection with field-effect transistors (FETs) in human serum, Scientific Reports, 7:5256
34. Elnathan, R.; Kwiat, M.; Pevzner, A.; Engel, Y.; Burstein, L.; Khatchtourints, A.; Lichtenstein, A.; Kantaev, R.; Patolsky, F. Biorecognition Layer Engineering: Overcoming Screening Limitations of Nanowire-Based FET Devices, Nano Letters, 12, 5245-5254, 2012
35. Chang, H-K.; Ishikawa, F.N.; Zhang, R.; Datar, R.; Cote, R.J.; Thompson, M.E.; Zhou, C. Rapid Label-Free Electrical Whole Blood Bioassay Based on Nanobiosensors Systems, ACS Nano, 5 (12), 9883-9891, 2015
36. Stern, E.; Vacic, A.; Rajan, N.K.; Criscione, J.M.; Park, J.; Illic, B.R.; Mooney, D.J.; Reed, M.A.; Fahmy, T.M. Label-free biomarker detection from whole blood, Nature Nanotechnology, 5 (2), 2010
37. Rajan, N.K.; Brower, K.; Duan, X.; Reed, M.A. Limit of detection of field effect transistors biosensors: effect of surface modification and size dependence, Applied Physics Letters, 104 (8), 2014

Chapter 3

HIGH ASPECT RATIO FIN-ION SENSITIVE FIELD EFFECT TRANSISTOR: COMPROMISES TOWARD BETTER ELECTROCHEMICAL BIOENSING

This chapter explores the Fin-FETs as pH sensors. I present the design and fabrication of such devices as well as an electrochemical model to describe their pH sensitivity. pH sensitivity will be described in terms of variation of the surface potential with the pH, strongly related to the properties of the dielectric material used for sensing, or as variation of the conductance with the proton concentration. The symbols $\Delta\Psi_0/\Delta pH$ and $\Delta G/\Delta pH$ will be used to refer to the two pH sensitivities, respectively. I study the sensitivity of the silicon oxide (SiO_2) sensing layer and the pH dependent output characteristics. I consider devices with different widths and comment about relative variation of the conductance with pH, and linearity. I fit the experimental data with the developed electrochemical model and I theoretically compare the Fin-FETs with Si-NWs. Finally I study the response time of the devices to variation of proton concentration and I discuss on the advantages of such devices for sensing in diffusion limited processes.

This chapter is based on the publication S. Rollo, D. Rani, R. Leturcq, W. Olthuis, C.P. García, "High Aspect Ratio Fin-Ion Sensitive Field Effect Transistor: Compromises toward Better Electrochemical Biosensing", *Nano Lett.*, 19 (5), 2019, 2879-2887.

3.1 Abstract

The development of next generation medicines demand more sensitive and reliable label free sensing able to cope with increasing needs of multiplexing and shorter times to results. Field effect transistor-based biosensors emerge as one of the main possible technologies to cover the existing gap. The general trend for the sensors has been miniaturisation with the expectation of improving sensitivity and response time, but presenting issues with reproducibility and noise level. Here we propose a Fin-Field Effect Transistor (Fin-FET) with a high height to width aspect ratio for electrochemical biosensing solving the issue of nanosensors in terms of reproducibility and noise, while keeping the fast response time. We fabricated different devices and characterised their performance with their response to the pH changes that fitted to a Nernst-Poisson model. The experimental data were compared with simulations of devices with different aspect ratio, stablishing an advantage in total signal and linearity for the Fin-FETs with higher aspect ratio. In addition, these Fin-FETs promise the optimisation of reliability and efficiency in terms of limits of detection, for which the interplay of the size and geometry of the sensor with the diffusion of the analytes plays a pivotal role.

3.2 Introduction

Silicon nanowire-Ion Sensitive Field Effect Transistors (Si-NW-ISFETs) based on the capacitance field effect of an electrolyte-insulator-semiconductor junction to detect the analytes are one of the candidates to be among the building blocks of the next generation molecular diagnostic devices as they offer label-free detection, are miniaturized and thus can be integrated on a microfluidic platform for rapid and low-cost assays[1-3]. Their three-dimensional configuration makes them more efficient than planar FETs to detect ultra-low concentrations of analytes due to a better gating effect[4-6]. There is a

second advantage linked to their geometry. The species contributing to the sensing signal are detected after binding to the functionalized surface of the device depleting the medium, which creates a concentration gradient. In order to reach the equilibrium signal the analytes must diffuse and bind to the surface of the sensor. At low concentrations, the diffusion of the molecules towards the sensor requires longer incubation times to reach the limits of detection that provide a readable signal. In a planar sensor, like a traditional ISFET, the remaining analytes can only diffuse in one dimension perpendicular to its surface. In Si-NWs the diffusion occurs in the two dimensions perpendicular to the wire (hemicylindrical), which results in a much faster adsorption of analytes[7-9]. Si-NWs have shown low limits of detection for different biomarkers comprising DNA[10-14] and proteins[2, 15-17] in different media including biological fluids[18-21] and tissues[22,23]. Owing to the well-known nanofabrication methods, and low operational power, Si NW-FETs can be easily integrated into CMOS chips where transducers and necessary circuits for signal processing are integrated on a single chip[2, 10, 15, 24]. Such devices bring promises in order to have cost effective point of care (POC) and highly multiplexed sensors for personalised precision medicines[25].

The transducing response of Si-NW-FET is faster than the diffusion and binding, which would qualify them for real-time sensing. However, the main limitation for real-time measurement is the Debye screening, which causes a limitation of the sensing region due to the counter-ions present and shielding the species at high ionic strength electrolytes[26, 27]. For this reason, many of the experiments reported in literature do not measure in physiological conditions, and consist first of an incubation step followed by washing and measurement at lower ionic strengths, which results in an end-point result detrimental for the biological potential of Si-NW's because they cannot evaluate kinematic constants like the molecular affinity[28-30].

Regardless of all their perspectives and the intense research activities during the last decades, Si-NW-FET still have not been introduced into any clinical application, mainly due to their problems of repeatability and reliability. Due to their small size, they are intrinsically sensitive to the fabrication defects that cause variations between devices, or more radical effects like the decrease in the effective dimensions of the conduction channel. In nano devices it is also more difficult to control the functionalisation with bio-receptors due to the small area available, which affects reproducibility of nano sensors. The current approaches are directed to improve the fabrication methods and the material reliability from the quality control on larger production batches[5, 31] and the control of composition homogeneity of the dielectric sensitive layer[32-34]. However, the current trend is the miniaturisation of NWs to exploit the advantages of small size and the three dimensional geometry, disregarding the difficulties to achieve reliable homogeneous functionalisation in single devices with few tenths of nanometres. Due to the small cross section of the conductive channels, Si-NWs carry relatively small currents, which makes their integration also more difficult due to the required voltage necessary to polarise high resistive devices. The requirements of more accurate instrumentation in small devices, together with their lack of reliability increases their production costs that cannot cope with the required quality control that would be necessary. NW arrays measured in parallel can increase the total signal, and mitigate some of the lack of reliability due to the averaged device variability, but this increases the overall device footprint, which limits their efficiency at low analyte concentrations in diffusion-limited processes[7-9,35] and jeopardizes the viability of massive multiplexing due to the increase of footprint.

In this work we approach the problem from the point of view of the design by combining advantages of nano sensors with the reliability of planar devices, being able to keep the advantages of three dimensional biosensors. We propose a novel Fin configuration for a FET with a high aspect ratio of

width (*W*) and height (*h*) of the device. Figure 3.1 (a) and (b) schematically show the proposed Fin-FET and the cross section at different ion concentrations, respectively. Setting *W* close to twice the maximum depletion region (W_D) expected during the dynamic range, the physical aspect ratio *h:W* and the electrostatic parameters specifying the channel doping, the dielectric constant and the thickness of the oxide are related. This relationship between the shape of the device and the electrostatic parameters has deep consequences for the performance of the wire in terms of total signal and linearity. We tested the operation of the Fin-FET against pH sensitivity. Our p-doped Fin-FETs work in depletion mode for positive charges like protons Considering the doping density of the starting SOI substrate, we designed our wires to switch from fully conductive (no depletion) to nearly fully depleted in a pH range of ~ 8 units (represented in fig. 3.1 (b)). The advantage of this configuration is that it offers larger total surface area compared to Si-NWs to decrease the impact of charge point defects and offer large output current with an improved linear response. In addition, the improvement in the output current would contribute to a higher signal to noise ratio and the 2D conductivity of the vertical Fin would improve the reliability decreasing the sensitivity to local defects. We also argue with geometrical reasons linked to the diffusion time, that the increased size of our sensor along the height with respect to NW's would not decrease significantly the detection limits. Finally, the increased size in the vertical direction enhances the total surface area of the sensor, which would also facilitate bio-functionalisation.

3.3 Results and discussion

Figure 3.1 (c) shows a SEM image of a representative device with the schematic representation of the measurement set-up. We fabricated our Si Fin-FETs by anisotropic wet etching on a p-doped silicon on insulator (SOI) substrate with a 2.2 ± 0.1 µm thick silicon device layer (<110> oriented) with resistivity of 0.115 Ω·cm (equivalent doping

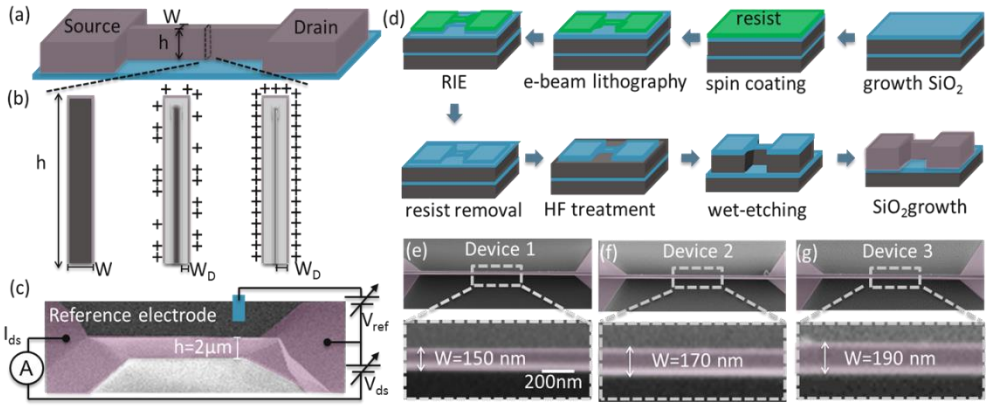

Figure 3.1 (a) Schematic representation of the Fin-FET. (b) Representation of the FIN-FET from low ion concentration to higher ion concentrations, switching from fully conductive to almost fully depleted. The darker grey represents in this case the region populated with positive carriers, while the lighter grey the depleted region. (c) SEM tilted picture of a representative device with the schematic representation of the measuring setup. (d) Summary of the fabrication process: 1x1 cm^2 diced samples of <110> SOI were used. Fifty nanometers of thermal SiO_2 were grown on top the SOI substrate. We spin casted a negative resist and exposed the Fin-FET mask design with e-beam lithography. We transferred the patterns by RIE leaving a few nm of oxide that was later removed by HF. Vertical walls were achieved by anisotropic wet etching of the <111> facets. The mask was removed by HF before contacting the samples. (e) to (g) Top view images of three representative devices reported in the article, with heights of 2.16 µm and top widths 150, 170 and 190 nm respectively , referred as devices 1 to 3 respectively. A zoomed region showing details of the top surface is also shown.

$10^{17}/cm^3$) and a 1 µm thick buried SiO_2 procured from Ultrasil Corporation. P-type channels FETs have shown higher sensitivity in terms of variation of the conductance and signal to noise ratio[36]. The overall fabrication process is illustrated in fig. 3.1 (d). Briefly, we lithographed the mask of the wires on a thermally grown thin SiO_2 that was transferred by Reactive Ion etching and then treated with HF to obtain smooth surface. The anisotropic etching was achieved with a 25 % wt Tetramethylammonium hydroxide, 8.5 %vol of isopropanol water solution using the proper orientation to obtain vertical walls. For ease of fabrication we used 20 nm of thermally grown SiO_2 to have a pH sensitive layer. The ohmic contacts were defined by optical lithography and e-beam evaporation. The devices were contacted with lithographically designed leads and the sample was protected with an epoxy (SU8) layer leaving open the region of the Fin-FET's. The sample

was mounted on a PCB, and wire bonded for measuring. The bonded wires were protected with a medical grade epoxy glue (details of fabrication in SI 3.1).

The resulting wires had a length of 14 µm at the middle of the Fin-FET, which we use later as the average length for calculations. We fabricated two samples each consisting of eleven Fin-FETs all showing coherent data with similar transfer characteristics and consistent output behaviour. Here we report the results from three representative devices from one of the samples where we carried out a more extensive characterisation. The height of the samples was measured 2.16 µm at the source and drain before the ohmic contacts with a KLA Tencor P-17 profilometer. The three considered devices are characterized by top widths (W) of 150, 170 and 190 nm, which account for aspect ratio $h:W$ of 15, 13 and 12, respectively, herein referred as devices 1 to 3 from the smallest to the biggest (figs. 3.1 (e) to (g)). After implementing ohmic contacts, metal leads and passivation of the contacts with optical lithography, the samples were measured in an electrolyte consisting of a solution of KH_2PO_4, citric and boric acids at 0.1 M all, mixed with a KNO_3 0.1 M solution in equal volume proportion, which had a final pH of 2.5. More basic pH were obtained by titration using a 0.1 M solution of KOH. With this procedure, the total ionic strength remained constant at 0.1 M (details in SI 3.2).

The SiO_2 surface of our wires is sensitive to the proton concentration, which changes the potential at the interface (Ψ_0) depleting the channel region of positive carriers. The non-depleted region contributes to the conductance with an ohmic contribution so that the total conductance is calculated from the remaining cross section, length and conductivity of the non-depleted region using a Nernst-Poisson model (we present detailed description in supporting information SI 3.6). In order to find the working range of drain source (V_{ds}) and reference electrode (V_{ref}) voltages in which the response of the devices can be described in terms of ohmic contribution of the non-

depleted region we run an electrical characterization at neutral pH. The drain source currents (I_{ds}'s) from the three devices were recorded within V_{ds} between -300 and 300 mV at different fixed values of V_{ref} between -300 and 300 mV separated by steps of 100 mV (details of the electrical characterization and data from a representative device is shown SI 3.3-3.4). We observed a linear behaviour of the output characteristics in V_{ds} voltages around the range between -100 and 100 mV at V_{ref} between -200 and 200 mV. We restricted our study to a more conservative working range for V_{ds} between of -50 to 50 mV where our samples regardless the low working potentials, exhibited a good signal to noise ratio. As expected from the Nernst-Poisson model, I_{ds} increased with lower V_{ref} due to the attraction of negative potentials on the positive carriers. From these results we identified the working range within $-50 < V_{ds} < 50$ mV and $-200 < V_{ref} < 200$ mV where the electrical transport of the Fin-FET devices can be described by the ohmic contribution of the non-depleted region using a Nernst-Poisson model.

3.3.1 Transfer characteristics of pH response

After the neutral pH characterization of the Fin-FET devices, they were deployed for electrolyte pH sensing. We measured the transfer characteristics sweeping V_{ref} at a fixed V_{ds}' (50 mV) and varying the electrolyte pH by manual titration from acidic towards basic values. Figures 3.2 (a) to (c) show the transfer I_{ds} vs. V_{ref} characteristics at eight different electrolyte pH values from 3 to 10 in steps of 1 represented with the green colour scale shown in (b) for devices 1 to 3, respectively. As expected from the wider cross-section, the devices with bigger width had higher currents than the smaller ones. The drain current increases with increase in pH of the electrolyte solution, because higher pH induces more negative surface potentials at the silicon oxide sensing layer surface, which in turns creates an attractive electric field for the positive charges inside the channel. In terms that are more standard for ISFETs operation, there is a shift needed of the reference electrode to keep the same depletion region.

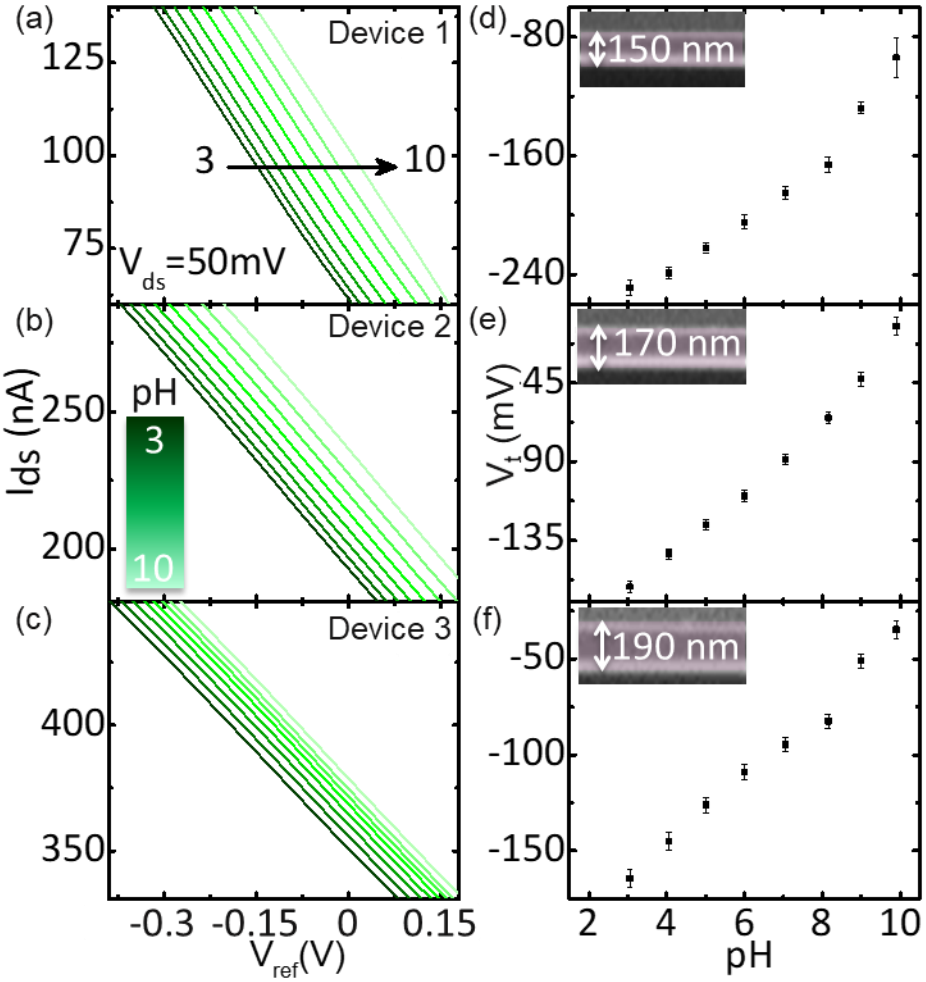

Figure 3.2 (a) to (c) are the transfer I_{ds} vs. V_{ref} characteristics at eight different electrolyte pH values from 3 to 10 in steps pf 1 represented with the green colour scale shown in (b) for devices 1 to 3, respectively. (d) to (f) are the evaluated shifts of the threshold voltage at different pH for devices 1 to 3, respectively.

The shift of the surface potential Ψ_0 was evaluated from the threshold voltage shift (V_t) calculating the minimum of the first derivative of the transfer curves at different electrolyte pH values (details of the procedure to derive V_t shown in SI 3.5). The variation of the threshold voltage as a function of the pH of the electrolyte is shown in fig. 3.2 (d) to (f) for the three devices. The threshold voltage of the Fin-FETs shifted

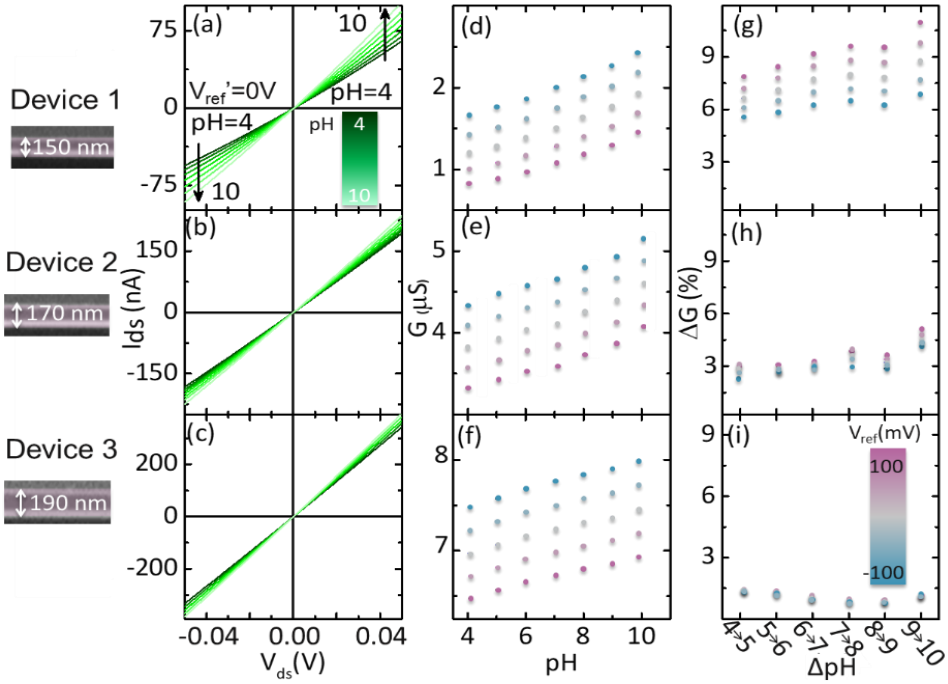

Figure 3.3 Output characteristics of devices 1 to 3: (a) to (c) I_{ds}-V_{ds} curves at a fixed V_{ref}' =0 V and different electrolyte pH, from 4 to 10 in step of 1. The curves evaluated at each pH are shown using the green colour scale shown in the inset of (a); (d) to (f) conductance as a function of pH at different V_{ref}', varying from -100 to 100 mV in steps of 50 mV shown using the colour scale shown in (i); (g) to (i) relative conductance change percentage per unit change in electrolyte pH at different V_{ref} voltages shown with the colour scale shown in (i).

towards more positive values with increase in electrolyte pH due to the deprotonation of the surface hydroxyl groups at the gate oxide, followed by an increase in majority charge carriers (holes) through the transistor channel linked to the decrease of the depletion region. We obtained an average shift in the threshold voltage with pH for the three devices of 22 mV/pH with a standard deviation in the different devices of ± 1 mV/pH. We attribute this deviation to inhomogeneity in the sensing oxide of the different devices. The pH response of Fin-FETs was reproducible over time and different experimental runs. The obtained sensitivity is lower in comparison to values reported in literature (~30 to 35 mV/pH for SiO_2 while the Nernst limit is ~ 59 mV/pH)[37,38]. In our case this could be due to defects introduced during the growth of the

sensing oxide since we could not use a dedicated chamber for the process. The change in Ψ_0 was ~ 175 mV in the studied pH range in all devices, which at the working point of V_{ref}' = 0 is falling within the working range that was chosen in characterisation of the devices at neutral pH.

3.3.2 Output characteristics of pH response

The output characteristics I_{ds} vs. V_{ds} of the three Fin-FETs at a fixed V_{ref}' = 0 V varying the electrolyte pH are shown in figs. 3.3 (a) to (c) with each curve corresponding to different pH values represented with the colour scale shown in (a). The I_{ds} *vs.* V_{ds} characteristics of the wires remained linear through all the electrolyte pH ranges exhibiting a good ohmic behaviour for all devices for the studied range between -50 and 50 mV. The conductance through the wire decreased with lower pH due to the repulsion of positive charge carriers by the protons adsorbed on the surface at more acidic concentrations and the subsequent increase of the depleted region. We evaluated the conductance values in this range at different electrolyte pH from the slope of the I_{ds} vs. V_{ds} curves.

The variation in conductance as a function of electrolyte pH at different fixed values of V_{ref}' from -100 mV to 100 mV in steps of 50 mV are shown in figs. 3.3 (d) to (f) using the same colour scale shown in the inset of fig. 3.3 (i). An increase in conductance of the devices for decreasing V_{ref}' was observed because of the attracting field experienced by the positive charge carriers in the semiconductor and consecutively the larger conducting cross section of the wires. The effect of increasing V_{ref}' is equivalent to lowering the pH, and the conductance of the devices increased with the increase of the pH of the electrolyte with a nearly linear response, which is coherent with what was observed in the transfer characteristics. We evaluated the relative change in conductance $\Delta G\% = ((G-G_0)/G_0))\ \%$ for each pH step at the different V_{ref}' (figs. 3.3 (g) to (i)). $\Delta G\%$ was higher for smaller width Fin-FETs, owing to the smaller dimensions resulting in an increasing impact of the depleted

region on the closure/disclosure of the channel. This is in contrast to the observed behaviour in the transfer characteristics where the change in the surface potential of the oxide provided similar sensitivity for all the devices. Devices 2 and 3 showed an approximately constant behaviour of $\Delta G\%$ reflecting a linear dependence of the output characteristics with respect to pH changes. Device 1 showed a less constant behaviour of the relative change in conductance in the investigated pH range, but with a total variation of $\Delta G\%$ of 2% in the pH range 4 to 9 it could still be considered more linear than NWs found in literature, with variation of ~ 12% in the same pH range[1,39]. As shown in fig. 3.1 (a) and (b) in our case with aspect ratio above 10, the depleted region (W_d) affects the conductance in the horizontal direction (along the width) but its effect is negligible in the vertical direction (along the height of the device the relative change $(h\text{-}W_d)/h$ is much smaller than the change $(W\text{-}W_d)/W$). These results suggest that due to the improved linearity in the output current, these devices could be measured by using their output characteristics rather than their transfer, since the small dimensions enhance the sensitivity in terms of $\Delta G\%$.

3.3.3 Theoretical and experimental data correlation

Higher currents require less amplification and thus facilitate the integration within measurement circuits. Also, the signal to noise ratio (output current divided by current noise amplitude) which is a limiting factor for ion/biosensitive FETs sensors is improved, because higher output currents would be less affected by instabilities coming from electrolyte fluctuations (concentration, composition, pH…) or the intrinsic device quality, which contribute to the current noise amplitude[40]. In fig. 3.4 (a) the conductance of the Fin-FET device 2 (width of 170 nm) versus the change in the surface potential is shown as black dots (showing the equivalent pH change in the top scale). We considered device 2 since its transfer characteristic allows the comparison with our Nernst-Poisson electrochemical model (details of model in SI 3.6) in a wider range where the shift of the transfer characteristics at

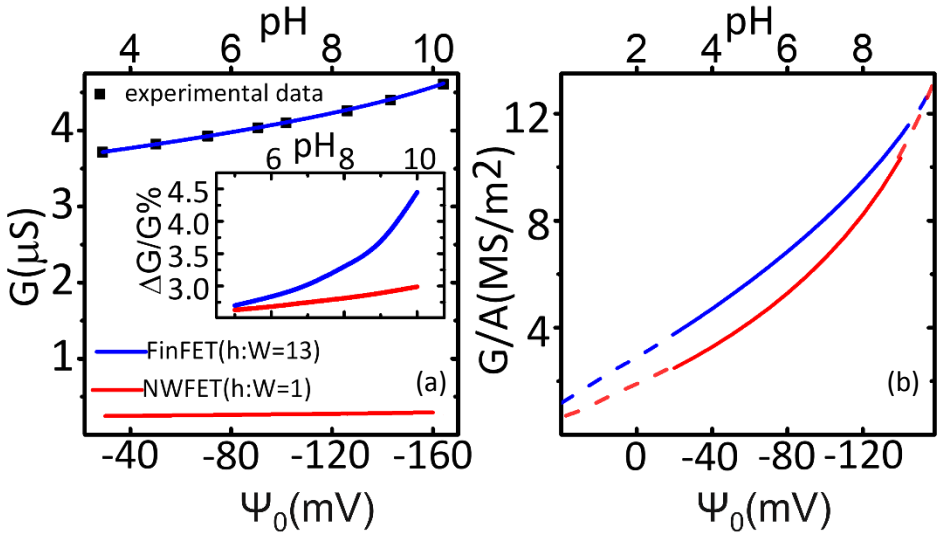

Figure 3.4 (a) Device conductance vs change in surface potential: for our device the experimental points are represented with black dots and the blue line is the data fitted with our Nernst-Poisson model. In red the calculation of the conductance for a wire with aspect ratio 1:1 using the same parameters is shown. The inset reports the relative variation of the conduction of the same data. (b) Conductance normalised to the cross section area vs change in surface potential for a high aspect ratio Fin-FET (black) and a 1:1 aspect ratio NW (red). In both graphs the pH corresponding to the surface potential is represented on top scale.

different pH values is almost linear and the dependence of Ψ_0 can be described with the Nernst equation[13]:

$$\frac{\partial \Psi_0}{\partial pH_B} = -2.303 \frac{kT}{q} \alpha \qquad \text{Eq.3.1}$$

where k, T and q are the Boltzmann constant, absolute temperature and elementary charge, respectively. The sensitivity parameter α ($0 \leq \alpha < 1$) as introduced in the previous chapter, is related to the buffer capacity of the oxide that also includes other parameters like the surface charges. The Poisson equation provides the charge distribution and the width of the depleted region of the device for a $\Delta\Psi_o$ associated to a ΔpH given the doping concentration and the sensing oxide thickness that was measured by ellipsometry on a flat sample processed with the wires. We fitted the experimental data to our model shown in blue for the

used Fin-FET with an aspect ratio of ~ 13. Since the Debye screening length corresponding to the carrier density in our device (~10 nm) falls within the error of the measurement of *W*, and considering that the capacitance effect is enhanced in Si respect to SiO_2 due to the higher dielectric constant (~3 times higher in Si), we neglected the effect of charge depletion at the interface. Within this model, the parameters of the oxide thickness and channel doping obtained were in good agreement with the experimental data. We obtained 20 nm for the oxide thickness both in the fitting and the experimental data obtained from the ellipsometry calibration of a probe sample used during the growth of the oxide. For the doping we obtained 2 x 10^{17} cm^{-3} from the fitting compared to 1-3 x 10^{17} cm^{-3} declared from the provider of the SOI substrate.

To analyse the response of our sensors with respect to traditional NWs, we compared the measured results of the Fin-FET with calculations on a device with an aspect ratio *h:W* equal to 1:1 therefore with a square cross section. The curve calculated with the same parameters obtained for the Fin-FET is also shown in red in figure 3.4 (a). As expected, the response of the NW is much lower as the curve is nearly flat for the considered change in surface potential. Essentially we observed that the conductance of the Fin-FET is proportional to the cross-section and thus to the aspect ratio. The inset in figure 3.4 (a) shows the calculated relative change of the conductance (ΔG/G%) of the same data which is also favourable to the Fin-FET.

In figure 3.4 (b) we show the conductance normalized to the cross-sectional area from the simulations with aspect ratios 13 and 1 (blue and red, respectively). This is equivalent to comparing our device with the signal from a NWs array of 13 wires that would reach approximately the same cross section. The curves have been extended beyond the experimental range to show the effect where the devices would be fully conductive ($W_D = 0$) and fully depleted ($2W_D = W$) with the dotted part of the graphs. Both devices have the same dynamic range because the depleting region is the same, and since they have the same width the electrical transport is closed at the same

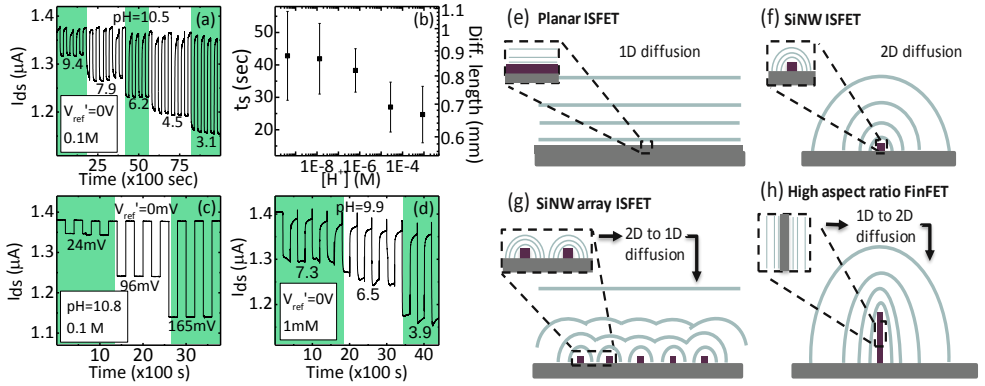

Figure 3.5 (a) Real time measurement of I_{ds} changing abruptly the pH from low proton concentration (pH 10.5) to higher proton concentration (changing successively to pH 9.4, 7.9, 6.2,4.5,3.1) without rinsing. Ionic concentration during the experiment was 0.1 M. (b) Result of the corresponding settling time and diffusion length derived from fitting (a) to a characteristic settling time (details of calculations in SI3.8). The large error bars correspond to the experimental dispersion originated in the difficulty of moving the sensor between different buffers without creating turbulences in the system. (c) Real time measurement of I_{ds} changing abruptly V_{ref} 24, 96 and 165 (mV) equivalent to changes in the surface potential produce by the pH changes of 1, 4, and 7 at ionic concentration 0.1 M. (d) Real time measurement of I_{ds} changing abruptly the pH from low proton concentration (pH 9.9) to higher proton concentration (changing successively to pH 7.3, 6.5 and 3.9) without rinsing. Ionic concentration during the experiment was 1 mM. (e) to (h) Schematic representation of the diffusion lines of equal concentration for an ISFET with much larger dimensions than the diffusion length, Si-NW, Si-NWs array and Fin-FET respectively. The sensor is represented in purple, the substrate in grey and the diffusion lines of equal concentration in light blue.

Ψ_0. In addition to the enhanced current shown in fig. 3.4 (a), in this case we note that the Fin-FET offers a reason for the increased linearity which was anticipated during the explanations of the changes in the relative conductivity. In the nanowire the depletion has the same relevance in the two physical dimensions of the wire (W and h), meanwhile in the Fin-FET the depletion in the direction of the width has a bigger impact in the conducting cross section. The doping density, the dielectric constant and thickness of the oxide determine the dynamic range in which the sensor switches from fully conducting ($W_D = 0$) to fully depleted ($2W_D = W$), which establishes the link between the physical aspect ratio and the electrostatic parameters. Comparing the two devices, we can conclude that while an array of 13 NWs in parallel would provide similar current, the Fin-FET has an improved linearity in a smaller footprint, and minor loss of sensitivity at acidic pH (<5). The comparison of the high aspect ratio Fin-FET to the h:W =1 geometry is

consistent with the comparison of the Fin-FET with other NWs reported in literature (shown in SI 3.7).

3.3.4 Drift and response time

We studied the current versus time characteristics of device 2 (width of 170 nm) implementing a real-time drain current measurement at fixed V_{ds}' (200 mV) and V_{ref}' (0 V). At a fixed pH 3 I_{ds} was stable over 3000 seconds time with observed drift lower than 1 nA (ca.1.5%) (data shown in SI 3.8). The pH of the electrolyte was also changed in a range from ~3 to ~11 in multiple cycles to study the hysteresis. We observed a change between cycles with maximum value of 15 nA evaluated at pH 3, which is similar to other values reported for SiO_2 pH ISFETs[38,41].

Additionally, we carried out pH measurements in which the sensor was swapped between solutions with different pH values. During these experiments, the temperature of the electrolytes was kept close to 0 ˚C using an ice bath to slow down the diffusion of ions in solution. The Fin-FET response was reproducible when the pH of the electrolyte was swapped several times from the solution at 10.5 to lower pH solutions in a range from 9.4 to 3.1 (Fig 3.5 (a)). During these measurements, the current of the sensor reached equilibrium after a settling time lasting several seconds, which was also reported in other pH sensing FETs in literature[42,43]. Figure 3.5 (b) shows the calculated settling time as function of the higher final proton concentration when the sensor was swapped from the electrolyte at pH 10.5 to the other lower pH values, obtained fitting the time response with an exponential function with a characteristic time constant (calculations details shown in SI 3.9). To discard the origin of the settling time from a capacitive effect, we measured the real-time response by changing the reference voltage. Specifically, the reference electrode voltage was increased from 0 to 24, 96 and 165 mV in multiple cycles, which would be equivalent to the change in surface potential produced by pH changes. Figure 3.5 (c) reports I_{ds} vs. time at a fixed V_{ds} and pH value. I_{ds} was stable within each V_{ref} value and no settling time was observed. We also discarded a contribution to the

settling time from the ionic strength due to charge screening of the ions in solution or due to the double layer capacitance by measuring the real-time response at a different electrolyte concentration. Figure 3.5 (d) shows I_{ds} vs. time when the sensor was moved several times from the solution at pH 10.5 to the lower pH solutions at an ionic strength 1 mM, two orders of magnitude lower than the experiments in fig. 3.5 (a). The obtained real-time pH response at two different electrolyte concentrations was similar and therefore we concluded that the change in electrolyte concentration has a negligible influence[44].

We interpreted the settling time as an effect of the proton diffusion. As described in the introduction, the analytes adsorbed by the sensing substrate create a concentration gradient in the solution. In our case when the Fin-FET is introduced from the higher pH solution into the lower ones the protons adsorbed create a gradient. The protons diffuse towards the oxide sensing layer until the surface saturates and the equilibrium is reached with the observed steady electrical signal. The efficiency of a sensor will depend on the sensitivity, but also on the time needed to reach the equilibrium or a significant signal for sensing. Figure 3.5 (e) to (h) represent the different gradient geometries created by a traditional planar ISFET, a NW, a NW array and our Fin-FET, respectively, showing lines of equal concentration. In a traditional planar ISFET with a (much) larger sensing area than the diffusion length (fig. 3.5 (e)) these lines are parallel to the surface of the sensor, and the diffusion occurs in one dimension, perpendicular to it. In a NW (fig. 3.5 (f)) the created lines of equal concentration are parallel to the axis of the wire, thus the diffusion occurs in the two perpendicular dimensions as function of the higher final proton concentration, which has been shown to provide a much shorter settling time than the case of the planar sensor[7]. NW arrays have a mixed behaviour shown in fig. 3.5 (g). At high concentrations the equilibrium is reached relatively faster and the particles provide mostly from a distance close to the sensor, shown in the area zoomed close to the NWs. In this case, the equal concentration lines are similar to the ones shown from

the single wire in fig 3.5 (f). However, as the concentration decreases the molecules have to diffuse from further regions. At some point, the equal concentration lines become similar to the one of the planar sensor; this effect was described as dimensionally frustrated diffusion and decreases the overall efficiency of NW arrays because it extends the settling times to unpractical limits[35]. In a Fin-FET when the initial concentration is high, the analytes can reach the sensor from close to the surface, diffusing on planar concentration fronts parallel to the surface of the sensor with a double gating effect. At lower concentrations associated with long incubation times the analytes that will reach the sensor originate from further regions and the diffusion will switch to 2D (hemicylindrical) (fig. 3.5 (h)). However, for the same surface area between a Fin-FET and an ISFET, at low concentrations the planar FET will also have a small surface area with respect to the concentration gradient thickness behaving like a point-source (or sink), thus experiencing hemi-spherical (3D) diffusion.

In accordance with Brownian motion, we calculated the associated length (L_D) to the diffusion time (τ) of our sensors $L_D = \sqrt{2D\tau}$, using for the diffusion constant of protons in water $D = 9 \cdot 10^{-9}$ m^2/sec. We included the equivalent length scale of the diffusion time in fig. 3.5 (b). The further distance from which the protons diffuse towards the Fin-FET surface varies from half to one mm, which is three orders of magnitude larger than the height of the sensor. The reason for the small change of settling time observed in the Fin-FET (comparable to the standard deviation) is a consequence of the fast diffusion of protons. Other potential analytes of interest like DNA or proteins with slower diffusion constants and potential incubation times of hours, can potentially have a behaviour in which the diffusion occurs differently depending on the initial concentration. To provide a coarse comparison of the potential impact of FIN-FETs in the mass transport of other analytes, we used the diffusion coefficients of haemoglobin and DNA strands of 21 nucleotides, but considering that the molecules would contribute to the signal similarly to protons (same changes in the surface potential). Within this

approximation in 43 seconds FIN-FETs would detect concentrations in the order of three orders of magnitude less for these biomolecules than for protons (details of the approximation in the SI 3.10), while for detecting 0.1 nM (close to the proton concentration of pH 10) the time needed to reach equilibrium is in the order of 10^4 seconds. Using the same approximation we compared the results for planar ISFETs and a single NWs. For planar ISFETs we estimated that in 43 seconds concentrations in the order of µM would be detectable in the case of biomolecules, while for the NWs it would be above nM. Also, the time required to detect concentrations of 0.1 nM would be 10^6 and 10^3 seconds for planar ISFETs and NWs respectively. Thus, the Fin-FET changes from a traditional ISFET like behaviour to a more efficient diffusion in 2D, which would provide an advantage to measure slow diffusing molecules at low concentrations.

3.4 Conclusions

We presented a rational design of a novel Fin-FET device for electrochemical bio sensing in which the width *W* is connected to twice the depleted region in the dynamic range of the biosensor and has an aspect ratio *h:W* of at least 10. We fabricated different versions of these Fin-FETs with different aspect ratios. In this article we report data from three representative devices with different *W*. The developed Fin-FETs were characterized in liquid gate configuration and showed reproducible pH sensitivity on different devices and experimental runs. The obtained pH sensitivity response of the dielectric in terms of variations of V_{ref} (~ 21 ± 3 mV/pH) was low compared to the values reported earlier for silicon oxide sensing layer, but it was reproducible over different experimental runs and independent on device sizes. The pH sensitivity in terms of normalized variation of the conductance showed a dependence on the Fin-FETs width, increasing with decreasing *W*. This size dependent effect is inherent to the

configuration of the developed Fin-FET sensor and was correlated with theoretical simulations. In addition, we characterised the device time response, observing a dependence of the settling time attributed to the diffusion of protons.

Advantages related to the Fin-FETs configuration over Si-NWs which makes them more friendly towards integration are higher measured device current in the same sensor footprint and improved linearity of the transduction of changes of charge at the surface, for devices with the same dynamic range. In addition Fin-FETs offer more reliability compared to nano devices owing to the planar configuration of the conduction channel in which the influence of charge point defects on the sensor electrical conduction is localised and thus less compared to NWs having narrower conduction channels. The high-aspect ratio allows a larger total surface area compared to NWs, which is advantageous to achieve a homogeneous functionalization of possible bio-receptors. We observed a dependence of the response time on the concentration of protons that we attributed to the diffusion and, through a rough approximation for the case of molecules with diffusion constants similar to proteins and nucleotides, we estimated the change in equilibrium times and limits of detection. We compared the results with the ones obtained for a planar ISFET and a NWs. We obtained that at low concentrations Fin-FETs approaches the performance of NWs. In conclusion we argue that the proposed configuration of the device would be beneficial for applications where slow diffusing molecules are in low concentrations providing high output currents while the geometry would benefit of the diffusion in several dimensions towards the sensor.

All these characteristics provide our sensor with promising advantages for improving sensing towards label free electrochemical sensing of charged biomarkers. We have set these benefits as a relation between the aspect ratio of the device and the depleted region during the dynamic range attributed to the analyte charges. In the future, the implementation of high k dielectrics to increase transduction effects,

the optimisation of fabrication parameters to improve performance and reliability and the implementation of functional surfaces, promise that Fin-FETs can have a deep impact in the configuration of bio-FETs. The bio-functionalisation of the Fin-FETs is expected to provide soon quantification for all these potentials.

References

1. Cui, Y.; Wei, Q.; Park, H.; Lieber, C.M. Nanowire nanosensors for highly sensitive and selective detection of biological and chemical species. Science 2001, 293 (5533), 1289–1292
2. Stern, E.; Klemic, J.F.; Routenberg, D.A.; Wyrembak, P.N.; Turner-Evans, D.; Hamilton, A.D.; LaVan, D.A.; Fahmy, T.M.; Reed, M.A. Label-free immunodetection with CMOS-compatible semiconducting nanowires. Nature 2007,445, 519-522
3. Li, J.; He, G.; Ueno, H.; Jia, C.; Noji, H.; Qi, C.; Guo, X. Direct real-time detection of single proteins using silicon nanowire-based electrical circuits. Nanoscale 2016, 8 (36), 16172-16176
4. Knopfmacher, O.; Tarasov, A.; Wangyang, F.; Wipf, M.; Niesen, B.; Calame, M.;Schönenberger, C. Nernst Limit in Dual-Gated Si-Nanowire FET Sensors. *Nano Lett.* 2010, 10 (6), 2268–2274
5. Rani, D.; Pachauri, V.; Mueller, A.; Vu, X.T.; Nguyen, T.C.; Ingebrandt, S. On the use of scalable nanoISFET arrays of silicon with highly reproducible sensor performance for biosensor applications. ACS Omega 2016, 1 (1), 84–92
6. Rani, D.; Pachauri, V.; Ingebrandt, S. Silicon Nanowire Field-Effect Biosensors. Label-free Biosensing, Advanced Materials, Devices and Applications; Springer Series on Chemical Sensors and Biosensors; Springer, 2018; 16, pp 27-57
7. Alam, M.A.; Nair, M.A. Performance Limits of nanobiosensors. Appl. Phys. Lett. 2006, 88 (23), 233120
8. Sheehan, P.E.; Whitman, L.J. Detection Limits for Nanoscale Biosensors. Nano Lett. 2005, 5 (4), 803-807
9. Squires, T.M.; Messinger, R.J.; Manalis, S.R. Making It Stick: Convection, Reaction and Diffusion in Surface-Based Biosensors. Nat. Biotechnol. 2008, 26, 417–426
10. Gao, A.; Lu, N.; Dai, P.; Li, T.; Pei, H.; Gao, X.; Gong, Y.; Wang, Y.; Fan, C. Silicon-Nanowire-Based CMOS-Compatible Field Effect Transistor

Nanosensors for Ultrasensitive Electrical Detection of Nucleic Acids. Nano Lett. 2011, 11, 3974–3978

11. Li, Z.; Chen, Y.; Li, X.; Kamins, T.I.; Nauka, K.; Williams, R.S. Sequence-specific label-free DNA sensors based on silicon nanowires. Nano Lett. 2004, 4, 245–247
12. Lu, N.; Gao, A.; Zhou, H.; Wang, Y.; Yang, X.; Wang, Y.; Tie, L.Progress in Silicon Nanowire-Based Field-Effect Transistor Biosensors for Label-Free Detection of DNA.Chinese Journal of Chemistry, DNA tTechnology; Wiley-VCH, 2016; 34, pp. 308-316
13. Schöning, M.J.; Poghossian, A. Recent advances in biologically sensitive field-effect transistors (BioFETs). Analyst 2002, 127, 1137-1151
14. Bunimovich, Y.L.; Shin, Y.S.; Yeo, W.S.; Amori, M.; Kwong, G.; Heath, J.R. Quantitative Real-Time Measurements of DNA Hybridization with Alkylated Nonoxidized Silicon Nanowires in Electrolyte Solution. J. Am. Chem. Soc. 2006, 128 (50), 16323-16331
15. Pui, T.S.; Agarwa,l A.; Ye, F.; Huang, Y.; Chen, P. Nanoelectronic detection of triggered secretion of pro-inflammatory cytokines using CMOS compatible silicon nanowires. Biosens. Bioelectron. 2011, 26, 2746–2750
16. Kim, A.; Ah, C.S.; Park,C.W.; Yang, J.H.; Kim, T.; Ahn, C.G.; Park, S.H.; Sung, G.Y. Direct label-free electrical immunodetection in human serum using a flow-through-apparatus approach with integrated field-effect transistors. Biosens. Bioelectron. 2010, 25, 1767-1773
17. Mao, Y.; Shin, K.S.; Wang, X.; Ji, Z.; Meng, H.; Chui, C.O. Semiconductor electronic label-free assay for predictive toxicology. Sci. Rep. 2016, 6
18. Zhang, G.J.; Chai, K.T.C.; Luo, H.Z.H;, Huang, J.M.; Tay, I.G.K.; Lim, A.E.J.; Je, M. Multiplexed detection of cardiac biomarkers in serum with nanowire arrays using readout ASIC. Biosens. Bioelectron. 2012, 35, 218–223

19. Stern, E.; Vacic, A.; Rajan, N.K.; Criscione, J.M.; Park, J., Ilic, B.R.; Mooney, D.J.; Reed, M.A.; Fahmy, T.M. Label-free biomarker detection from whole blood. Nat. Nanotechnol. 2009, 5 (2), 138–142
20. Zhang, Y.L.; Chen, R.M.; Xu, L.; Ning, Y.; Xie, S.G.; Zhang, G.J. Silicon nanowire biosensor for highly sensitive and multiplexed detection of oral squamous cell carcinoma biomarkers in saliva. Anal. Sci. 2015, 31, 73–78
21. Shehada, N.; Bronstrup, G.; Funka, K.; Christiansen, S.; Leja, M.; Haick, H.Ultrasensitive silicon nanowire for real-world gas sensing: noninvasive diagnosis of cancer from breath volatolome. Nano Lett. 2015, 15 (2), 1288–1295
22. Dai, X.; Zhou, W.; Gao, T.; Liu, J.; Lieber, C.M. Three-dimensional mapping and regulation of action potential propagation in nanoelectronics-innervated tissues. Nat. Nanotechnol. 2016, 11, 776–782
23. Puppo, F; Doucey, M.A.; Delaloye, J.F.;Moh, T.S.W.; Pandraud, G.; Sarro, P.M.; De Micheli, G.; Carrara S. Si-NW-FET in-air biosensors for high sensitive and specific detection in breast tumor extract. IEEE Sens. J. 2016, 16, 3374–3381
24. Lei, K.M.; Mak, P.I.; Law, M.K.; Martins, R.P. CMOS biosensors for in vitro diagnosis - transducing mechanisms and applications. Lab on a Chip 2016, 16, 3664-3681
25. Doucey, M. A.; Carrara, S. Nanowire Sensors in Cancer. Trends in biotechnology 2018. DOI:https://doi.org/10.1016/j.tibtech.2018.07.014
26. Gao, N.; Zhou, W.; Jiang, X.; Hong, G.; Fu, T.M.; Lieber, C.M. General strategy for biodetection in high ionic strength solutions using transistor-based nanoelectronic sensor, Nano Lett. 2015, 15 (3), 2143-2148
27. Nakatsuka, N.; Yang, K.A.; Abendroth, J.M.; Cheung, K.M.; Xu, X.; Yang, H.; Weiss, P.S. Aptamer–field-effect transistors overcome

Debye length limitations for small-molecule sensing. Science 2018, 362 (6412), 319-324

28. Bunimovich, Y.L.; Shin, Y.S.; Yeo, W.S.; Amori, M.; Kwong, G.; Heath, J.R. Quantitative real-time measurements of DNA hybridization with alkylated nonoxidized silicon nanowires in electrolyte solution. J. Am. Chem. Soc. 2006, 128 (50), 16323-16331
29. Nagrath, S.; Sequist, L.V.; Maheswaran, S.; Bell, D.W.; Irimia, D.; Ulkus, L.; Smith, M.R.; Kwak, E.L.; Muzikanski, A.; Ryan, P.; Balis, U.J.; Tompkins, R.G.; Haber, D.A.; Toner, M. Isolation of rare circulating tumor cells in cancer patients by microchip technology. Nature 2007, 450, 1235-1239
30. Stern, E.; Wagner, R.; Sigworth, F.J.; Breaker, R.; Fahmy, T.M.; Reed, M.A. Importance of the Debye screening length on nanowire field effect transistor sensors. Nano Lett. 2007, 7 (11), 3405–3409
31. Ishikawa, F.N.; Curreli, C.; Chang, H.K.; Chen, P.C.; Zhang, R.; Cote, R.J.; Thompson, M.E.; Zhou, C.A. Calibration Method for Nanowire Biosensors to Suppress Device-to-Device Variation. ACS Nano 2009, 3, 3969–3976
32. Noor, M.O.; Krull, U.J. Silicon nanowires as field-effect transducers for biosensor development: A review. Anal. Chim. Acta 2014, 825, 1-25
33. Luye, M.; Ye, C.; Sawtelle, S.D.; Wipf, M.; Xuexin, D.; Reed, M.A.; Silicon Nanowire Field-Effect Transistors: A Versatile Class of Potentiometric Nanobiosensors, Access IEEE 2015, 3, 287-302
34. Zafar, S.; D'Emic, C.; Jagtiani, A.; Kratschmer, E.; Miao, X.; Zhu, Y.; Mo, R.; Sosa, N.; Hamann, H.; Shahidi, G.; Riel, H. Silicon Nanowire Field Effect Transistor Sensors with Minimal Sensor-to-Sensor Variations and Enhanced Sensing Characteristics. ACS Nano 2018, 12, 6577–6587
35. Pradeep, A.; Nair, R.; Muhammad, A. Dimensionally Frustrated Diffusion towards Fractal Adsorbers. Phys. Rev. Lett. 2007, 99 (25), 256101

36. Li, Z.; Chen, Y.; Li, X.; Kamins, T.I.; Nauka, K.; Williams, R.S. Sequence-Specific Label-Free DNA Sensors Based on Silicon Nanowires. Nano Lett. 2004, 4 (2), 245-247
37. Nguyen, T.C.; Schwartz, M.; Vu, X.T.; Blinn, J.; Ingebrandt, S. Handheld readout system for field-effect transistor biosensor arrays for label-free detection of biomolecules. Phys. Status Solidi A 2015, 212 (6), 1313-1319
38. Phu Tran, D.; Thanh Phan, T.T.; Wolfrum, B.; Offenhausser, A.; Thierry, D. CMOS-Compatible Silicon Nanowires Field Effect Transistor Biosensor: Technology development Towards Commercialization. Materials 2018, 11 (5), 785
39. Chen, S.; Bomer, J.G.; Carlen, E.T.; van den Berg, A. Al_2O_3/Silicon NanoISFET with Near Ideal Nernstian Response. Nano Lett. 2011, 11, 2334-2341
40. Rajan, N.K.; Routenberg, D.A.; Reed, M.A. Optimal signal-to-noise ratio for silicon nanowire biochemical sensors. APPL. Phys. Lett. 2011, 98, 264107-1
41. Vu, X.T. Silicon nanowire transistor arrays for biomolecular detection. Master of Materials Science Thesis, Aachen University, Aachen, Germany, 7 September 2011
42. Poghossian, A; Baade, A; Emons, H.; Schoning, M.J. Application of ISFETs for pH measurement in rain droplets. Sens. Actuators B 2001, 76, 634-638
43. Dun, Y.; Ya-dong, W.; Gui-hua, W. Time dependent response characteristics of pH-sensitive ISFET. Sens. Actuators B 1991, 3, 279-285
44. van Hal, R.E.G.; Eijkel, J.C.T.; Bergveld, P. A novel description of ISFET sensitivity with the buffer capacity and double-layer capacitance as key parameters. Sens. Actuators B 1995, 24 (1-3), 201-205

Supplementary Information to chapter 3

SI3.1 Details of sample fabrication

A thin layer of SiO_2 (used as mask) was thermally grown on top of our substrates using a Rapid Thermal Chemical Vapour Deposition (RTCVD) reactor with a pure oxygen flow of 200 sccm at atmosphere and 1050 °C during 340 seconds to obtain an oxide layer of 50 nm. We spin-casted ma-N2043 negative electron beam (e-beam) resist at 2000 rpm for 1 minute to obtain a 300 nm thick layer. The resist coated substrate was post baked at 120 °C for 5 minutes. The Fin-FET design was patterned using a FEI-HELIOS microscope equipped with XENOS lithography system. After developing (ma-D developer for 1 minute with manual stirring) patterns were transferred by Reactive Ion Etching (RIE) using a CF_4 plasma at 25 W power and 75 mTorr pressure for 15 minutes to leave a few nm of un-etched SiO_2 outside the patterns, which was later removed by dilute (2%) HF isotropic treatment to leave smooth silicon surface. Thereafter, we etched our samples in a 25 %wt Tetramethylammonium hydroxide, 8.5 %vol of Isopropanol water solution at 43 ± 1°C under automatic stirring (250 rpm). Etching was carried out until the device layer was completely removed outside the patterned areas. After removing the SiO_2 mask with HF we thermally grew 20 nm of oxide layer using the RTCVD mentioned above. We used scanning UV sacrificial laser lithography (SLL) to pattern ohmic contacts. A second SLL was used to define lead contact for the devices. These were deposited with a combination of e-beam evaporation (5 nm of Ti followed by 50 nm of Au), followed by 100 nm of conformal sputtering used to overcome the step of the ohmic contacts. Finally UV lithography on SU8 was used to protect outside the sensing areas of the wires, opening windows of 14 x 50 μm^2. The sample was then mounted on a printed circuit board and wire bonded with a TPT HB16 semiautomatic wire bonder. The metal wires were passivated using a commercial liquid epoxy with medical grade Loctite Hysol M-31CL.

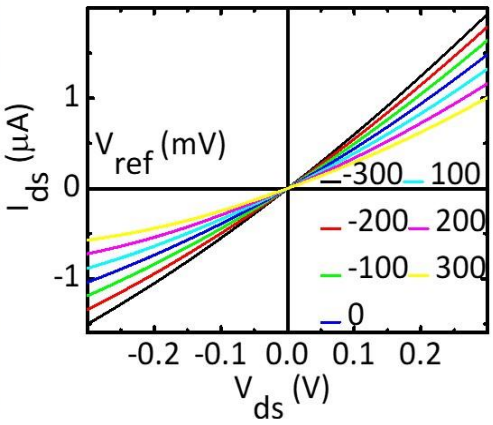

Figure SI3.1 (LEFT) pH measurements set-up with the Faraday cage, the PCB with the chip immersed in the buffers connected to the switching box and the Keithley sourcemeter used for the electric measurements.

Figure SI3.2 (RIGHT) Representative output characteristic at pH=7 from the device with width of 170 nm, at different fixed values of the reference electrode voltage.

SI3.2 pH titration

During the experiments titration was used to change the pH from acidic to basic and vice versa. All the chemicals were purchased by Sigma Aldrich. First we prepared a solution of potassium phosphate, citric acid and boric 0.1M all. Then we prepared another solution of potassium phosphate 0.1M. The chemicals were weighted and transferred into two 1L bottles. Milli-Q water was the solvent for all the buffers. The two solutions were mixed in a 1:1 ratio volume. From this mixture a buffer with a pH of 2.5 is obtained. To increase the pH a 0.1M KOH solution in water was added using a pipette 1 mL at a time and the change in the pH was monitored through a pH meter immersed in the solution. Contrarily, to swap from basic to acidic pH, the 1:1 mixture mentioned above was added.

SI3.3 Electrical characterization

We used a Keithley 2614HB DC source-meter using two-wire configuration to obtain the current-voltage (I-V) curves. We polarised the devices using a calomel reference electrode (BioLogic R-XR300). We used a commercial calibrated pH sensor (Sentron S1600) to monitor the pH and temperature

stability. We used a bath placed on a hotplate to stabilise the temperature of the experiments. All the measurements were performed in a Faraday which provided screening from noise. The software Labber was used to set the electrical parameters. Figure SI3.1 shows the measurement set-up used during the pH sensing experiments.

SI3.4 Output characteristics at neutral pH

To characterise the response of our sensors, we measured the output characteristics at neutral pH (=7) in a range of drain source voltages between -300 and 300 mV at different fixed values of reference electrode voltages between -300 and 300 mV in steps of 100 mV. Figure SI3.2 is a representative graph from the 170 nm wide wire. This characterization aimed at finding the linear range in term of source drain voltages and reference electrode voltages response to fix the working point lately used for the pH sensing. This linear range was identified to be around V_{ds} voltages between -100 and 100 mV and V_{ref} voltages between -200 and 200 mV, but the range lately used for pH sensing was chosen to be between -50 and 50 mV V_{ds} since regardless such low potentials the devices exhibit a good signal to noise. The conductance of the devices (given by slope of the curves) decreases with increase in applied gate voltage as expected in a p-type FET where the positive charge carriers are experiencing a repulsive electric field which depletes them.

SI3.5 Derivation of the flat-band voltage

To study the sensitivity of the silicon oxide to pH we followed the shift of the threshold voltage (V_t). As explained in section 2.1 of chapter 2 in an ISFET, like in MOSFET, the threshold voltage is (eq. 2.2 in chapter 2):

$$\boldsymbol{V_t = V_{FB} - \frac{Q_B}{C_{ox}} + 2\phi_F}$$

Where V_{FB} is given by the following expression (eq. 2.3 in chapter 3):

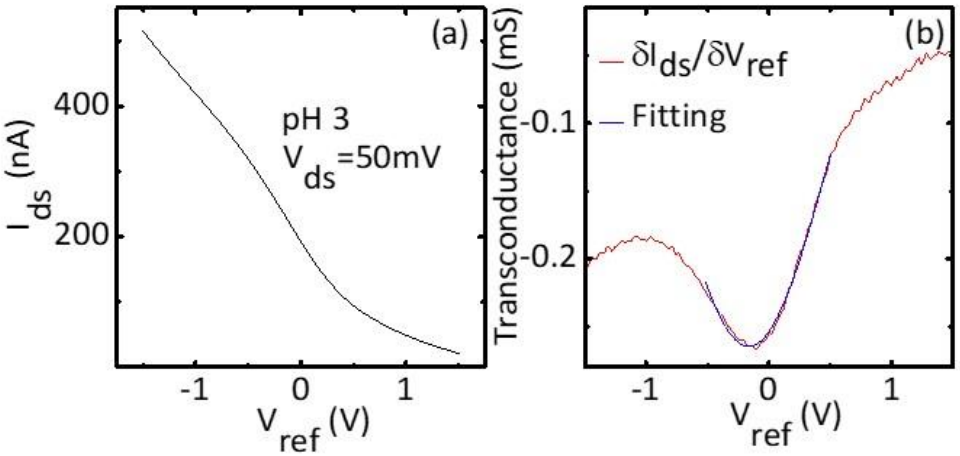

Figure SI3.3 (a) and (b) Example of transfer characteristic and its first derivative used for the extrapolation of the flat band voltages. The blue curve in (b) represent the Gaussian fitting of the peak of minima transconductance.

$$\boldsymbol{V_{FB} = V_{ref} - \Psi_0 + \chi_{sol} - \frac{\phi_{Si}}{q} - \frac{(Q_{SS} - Q_{ox})}{C_{ox}}}$$

In this last expression V_{ref} represents the contribution of the reference electrode, χ_{sol} the surface dipole potential of the solution, φ_{Si} the silicon electron work function an q the elementary charge. Q_{SS} and Q_{OX} represent the semiconductor/oxide interface charges and fixed charges in the oxide respectively. All these parameters can be considered as constants (assuming the same band bending condition in the semiconductor) except for the surface potential at the oxide-solution interface Ψ_0 which makes V_{FB} and thus V_t dependent on the pH. We calculated the values of V_t as function of the *pH* from the minimum of the transconductance $(\delta I_{ds}/\ \delta V_{ref})$[1]. To get a more accurate position of the minimum we fitted the transconductance with a gaussian peak. An example of a transfer and transconductance curves and fitted peak is shown in figs. SI3.3 (a) and (b), respectively. The same method explained here was used on all the transfer characteristics recorded.

SI3.6 Theoretical model

We developed a model to derive an expression for the depletion region width (W_D) inside the semiconductor, which we used to calculate the variation of

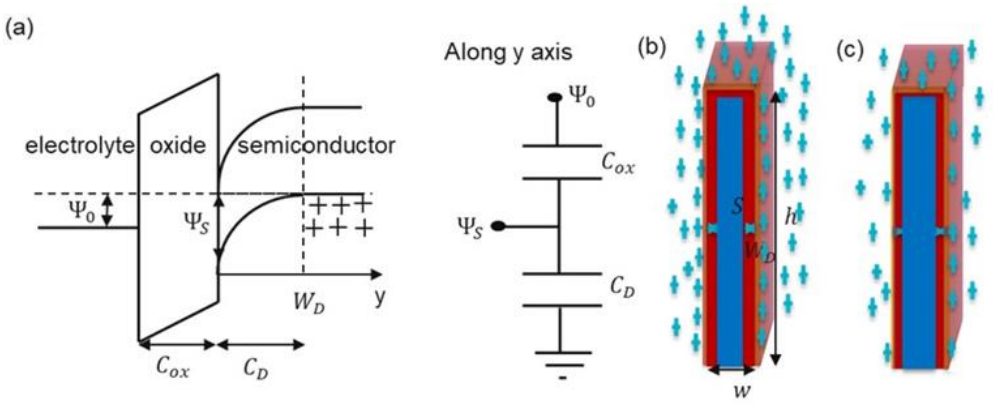

Figure SI3.4 (a) Schematic of the electrolyte/oxide/p-type semiconductor and two capacitors model. (b) and (c) Cross section of the Fin-FETs devices in acidic and basic conditions respectively with the depletion width. The silicon oxide, bulk silicon and depleted region are coloured in purple, blue and red respectively.

the conductance with the pH according to the ohmic law. The model takes into consideration the chemical and electrostatic equilibriums. The first effect is the interaction of the protons with the silanol groups on the sensing silicon oxide surface, which can be protonated or deprotonated. At the chemical equilibrium there will be a charge on the surface which generates a surface potential Ψ_o. The relation between this surface potential and the pH is described by the Nernst equation[2]:

$$\delta\Psi_0 = -2.303\frac{kT}{q}\alpha(pH_B - pH_{zc}) \qquad \text{Eq. SI3.1}$$

where k, T, q and pH_{zc} are the Boltzmann constant, the absolute temperature, the elementary charge and the point of zero charge of the oxide (2 for SiO_2) respectively. pH_B represents the pH of the bulk and α is a sensitivity parameter which takes into account the buffer capacity of the oxide and the double layer capacitance. The electrostatic equilibrium is reached with the redistribution of the charges inside the semiconductor due the surface potential Ψ_o. This can be described with the Poisson equation (eq. SI3.2)[3]:

$$\frac{d^2\Psi_S}{dx^2} = -\frac{\rho}{\varepsilon_{Si}\varepsilon_0} = -\frac{qN_A}{\varepsilon_{Si}\varepsilon_0} \qquad \text{Eq. SI3.2}$$

where Ψ_s is the potential at the oxide/semiconductor interface and ρ is the charge density inside the semiconductor that in the approximation of total depletion is equal to the doping (N_A in $(cm^3)^{-1}$). The relation between the two equilibrium phenomena is described through the two capacitors model where the oxide and the depleted region are considered as two capacitors in series, as illustrated in fig SI3.4 (a). At the equilibrium, the charge at the plate of the two capacitors (Q_{ox} and Q_D) must be the same (eq. SI3.3):

$$Q_{ox} = (\Psi_0 - V_{fg} - \Psi_S)C_{ox} = \Psi_S C_D = Q_D \qquad \text{Eq. SI3.3}$$

where V_{fg} is the front gate potential, normally applied to the electrolyte through a reference electrode, and C_{ox} and C_D represent the areal capacitance:

$$C_{ox}\left(\frac{F}{m^2}\right) = \frac{\varepsilon_0 \varepsilon_{SiO2}}{t_{ox}};\ C_D\left(\frac{F}{m^2}\right) = \frac{\varepsilon_0 \varepsilon_{Si}}{W_D} \qquad \text{Eq. SI3.4}$$

Here t_{ox} is the thickness of the oxide. Combining equations SI3.1 to SI3.4 it is possible to derive an expression for W_D dependent on the *pH* through Ψ_o and on fabrication parameters such as the doping density N_A of the semiconductor and the thickness t_{ox} of the sensing oxide:

$$W_D(N_A, t_{ox}, \Psi_0) = -\frac{\varepsilon_{Si}}{\varepsilon_{ox}} t_{ox} + \sqrt{\frac{\varepsilon_{Si}^2}{\varepsilon_{ox}^2} t_{ox}^2 + 8\frac{\varepsilon_{Si}\varepsilon_0(\Psi_0 - V_{fg})}{qN_A}} \qquad \text{Eq. SI3.5}$$

For a p-doped semiconductor in acidic conditions (higher concentration of protons) the width depleted of the positive charge carriers is higher than in basic condition due to the more protonated silicon oxide surface, which creates a repulsive electric field for the positive charge carriers inside the semiconductor. A schematic of the depletion width in acidic and basic conditions is provided in fig. SI3.4 (b) and (c) where the sensing silicon oxide is represented in purple colour, the bulk p-type semiconductor in blue and the depleted area W_D in red. We calculated the variation of the conductance

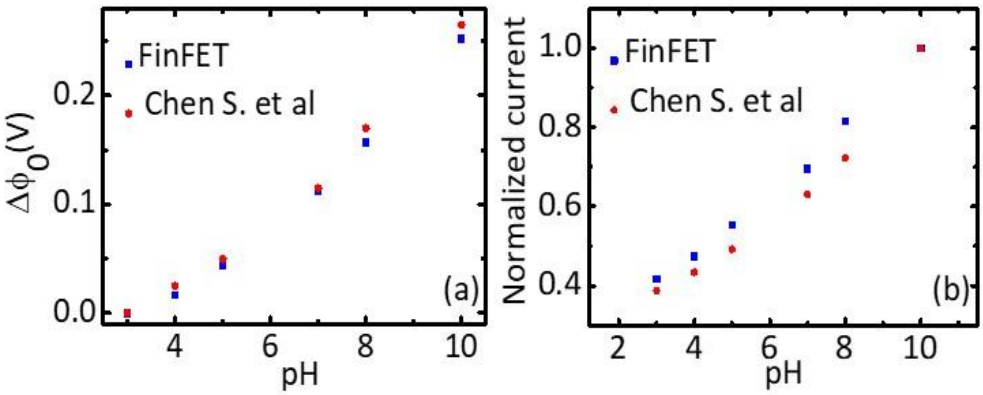

Figure SI3.5 (a) Experimental silicon oxide (20 nm both cases) response to pH in terms of surface potential ϕ_0 variation from our experiments and the couple of triangular nanowires from Chen S. (b) Correspondent experimental normalized output current.

(*G*) through the Ohms law, using W_D to calculate the change in the cross-section of the conducting area:

$$\Delta G = \sigma \frac{\Delta S}{L} = \sigma \frac{wh-(w-2W_D)(h-W_D)}{L} = \sigma \frac{wh-(wh-wW_D-2hW_D+2W_D^2)}{L} \quad \text{Eq. SI3.6}$$

where σ represents the conductivity of the bulk silicon, ΔS and L represent the variation of the conductive cross section along the channel and the length of the channel, and w and h represent the width and height respectively. While the oxide response depends on the surface characteristics of the oxide, the transduction depends on the total cross sectional area and how it varies with the pH through the depletion width (opening and closing the channel). Considering the variation of the cross sectional area available to the conduction as ΔS in eq. SI3.6 in the case of NWs (w~h) the quadratic term dominates the equation, while in the case of high aspect ratio Fin-FETs, as h is few orders of magnitude bigger than W_D the linear term is dominant.

SI3.7 Comparison with nanowires reported in literature

The linearity of ISFETs in literature (including in the concept to NWs) usually refers to the chemical sensitivity of the oxide layer, which is reflected in the transfer characteristics as variation of the surface potential with the pH. The transduction of the oxide sensitivity on the output current depends

intrinsically on the geometry of the sensor, which is linear in the case of planar ISFETs and quadratic in the case of NWs. This behaviour is shown in the calculations in the supporting information SI3.6. Since the current output characteristics depend on the properties of the oxide, doping and geometry parameters, it is difficult to find in literature an experiment in which all of them can be compared, so in the article we used the calculations shown in figure 3.4 in the chapter. Nevertheless, to allow a comparison with results on NWs reported in literature we include data from another Fin-FET in which we had a higher transfer response, which could be better compared. We report the new data of a Fin-FETs (150 nm wide, 2 µm high) with a 20 nm thick silicon oxide and $\Delta\Psi_o/pH$ = 46 mV/pH in the linear most sensitive part (7< pH <10). These data were compared with the results reported on two triangular nanowires in parallel by Chen S. et al, Nano Lett. 2011, 11, 2334-2341 with 20 nm thick silicon oxide as well. The oxide sensitivities and correspondent output currents for the two experiments are shown in fig. SI3.5 (a) and (b). We normalised the currents to the cross sectional area of the devices to be able to compare. The data were fitted with a linear fitting as well as a quadratic one. The residual sum of squares was considered as an estimation of the goodness of the fitting. The data from our experiment resulted in a fitting with a residual sum of squares of 70 and 15 for the linear and quadratic fitting respectively, while from the fitting on the data reported for the nanowires we obtained 176 and 8, showing that Fin-FETs have a more linear behaviour in the output characteristics.

To compare a situation within the same oxide conditions, we used the calculation in fig. 3.5 (b) in the chapter and calculate the residuals. The quadratic fitting on the Fin-FET and the nanowire in this case gave a residual sum of squares of 1.9 and 6.2 respectively showing that the Fin-FET has an improved linear behaviour.

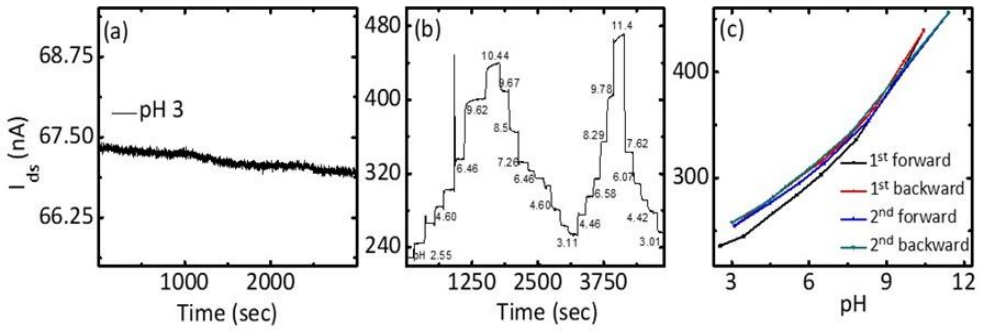

Figure SI3.6 (a) Drift in the drain current in 50 minutes time at pH 3 and fixed source drain and reference electrode voltages (50 mV and 0 mV respectively). (b) Real-time characteristic: source drain current vs time in device 2 (170 nm width) for two ramps of the pH from acidic to basic and vice versa at fixed source drain and reference electrode voltages (200 mV and 100 mV respectively). (c) Effect of hysteresis and drift on the current at different pH extrapolated from data in (b).

SI3.8 Study of hysteresis and drift

To study the stability of the output current in time at constant pH we recorded the source drain current of one of our devices at pH 3 for 50 minutes at fixed source drain voltage (50 mV) and reference electrode voltage (0 V), as shown in fig. SI3.6 (a). A drift less than 1 nA was observed over this period of time. The real-time response of the drain current was also studied when changing the pH of the solution by manual titration. Figure SI3.6 (b) represents the drain current versus time recorded for the device 2 (width of 170 nm) when sweeping the pH back and forward twice, at a fixed source drain voltage (200 mV) and reference electrode voltage (100 mV). The different values of the currents obtained for the same value of pH in the two ramps can be attributed to a combination effect of hysteresis and drift considering the long measurement time (1h30min). The maximum value of difference was estimated to be of 15 nA a pH 3, as shown in fig. 3.6 (c). From the data recorded about the drift in fig. SI3.5 (a) we recognize the hysteresis effect as main contribution, probably due to imperfections while growing the silicon oxide, surface defects, or the penetration of ions from the electrolyte.

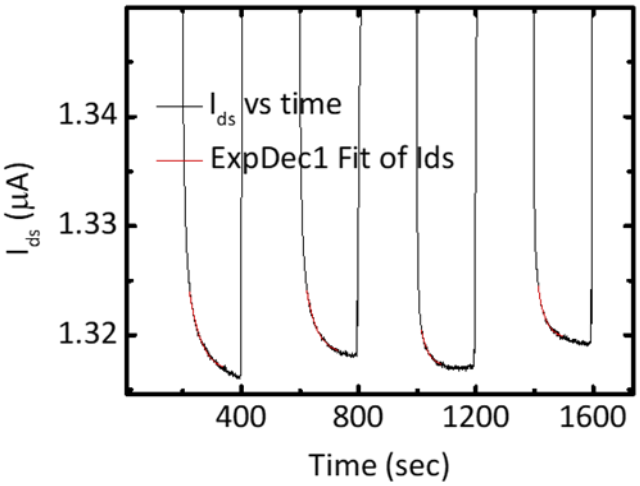

Figure SI3.7 An example of the exponential decay fitting performed on the time response characteristic of the device in order to derive the settling time from a fitting parameter.

SI3.9 Derivation of the settling time

The settling time necessary to achieve a steady state signal was derived from the fitting of the time response curve to the change of pH with a first order exponential decay formula:

$$y = A1e^{(-\frac{x}{t1})} + y_0$$

performed at the start of the bending of the curve, before reaching the stable current. Figure SI3.7 shows a highlight of the area where the fitting has been performed, and of the fitted curves (in red) as an example. From the fitting three parameters are derived (A1, t1 and y_0). We considered the time constant t1 as the settling time, as reported in the paper.

SI3.10 Quantitative evaluation of diffusion

To provide a rough quantification of the mass transport of molecules for different FET geometries, we considered the 43 seconds that takes to our sensors to reach equilibrium at pH 10 ($C=4\cdot10^{-10}$ M), as shown in fig. 3.5 (b) in the chapter. We calculated the diffusion length from the diffusion coefficient (D):

$$L = \sqrt{2Dt}$$

Using the case of protons we calculated the corresponding volume V around the sensor body from where analytes are within the diffusion length:

$$V_{FinFET} = \big(2L(h_{FinFET} + L)\big) + w_{FinFET}L) \cdot l_{FinFET}$$

Being $w_{Fin\text{-}FET}$, $h_{Fin\text{-}FET}$ and $l_{Fin\text{-}FET}$ the width, height and length of the Fin-FET respectively. Using the detected concentration (C) we calculated the number of analytes (N) which were within the reach of the sensor and therefore could have contributed to the signal.

$$N = C \cdot V_{FinFET}$$

Fin-FET	D (m^2/s)	L in 43sec (m)	V (m^3)	N	C (M) for 43s	Time (s) For 10^{-10}M
Protons	$9 \cdot 10^{-9}$	$8.8 \cdot 10^{-4}$	$2.2 \cdot 10^{-11}$	$8.7 \cdot 10^{-18}$	$4 \cdot 10^{-10}$	43 s

Making a rough approximation that other analytes contribute similarly in different biosensors (similar affinity constants and that the charge has the same order of magnitude), then the number of molecules needed for sensing would be also similar. Using the volume obtained for 43 seconds for other diffusion coefficients (we chose the D's of haemoglobin and DNA strands although they could contribute with different charges), and same N, we calculated the concentrations that we could have detected within the same time, and the time it would take to detect 0.1 nM (similar concentration than the one detected in the case of protons).

Results are reported in the table below.

Fin-FET	D (m^2/s)	L in 43sec (m)	V (m^3)	N (same as protons)	C (M) for 43s	Time (s) For 10^{-10} M
Hemoglobin (in water)	$6.9 \cdot 10^{-11}$ (4)	$7.7 \cdot 10^{-5}$	$1.71 \cdot 10^{-13}$	$8.7 \cdot 10^{-18}$	$5.1 \cdot 10^{-8}$	$2.25 \cdot 10^{4}$
DNA (in water)	$5.3 \cdot 10^{-11}$(5)	$6.7 \cdot 10^{-5}$	$1.32 \cdot 10^{-13}$	$8.7 \cdot 10^{-18}$	$6.6 \cdot 10^{-8}$	$2.92 \cdot 10^{4}$

With the same approximations and considering different FET geometries having similar transducing properties (same oxide, same doping density…), we approximated that the number of analytes N providing similar signal per sensor area has to be the same in all cases. We used the Fin-FET to calculate that number of analytes per surface area, and we used this to calculate the concentration of analytes measured after 43 seconds, and the time needed to have an equilibrium signal for a concentration of 10^{-10} M, using the same rational than the previous calculations. As examples, we considered a planar square ISFET of 500 µm width and a NW with a square cross section and same width and length of the Fin-FET of 170 nm and 14 µm respectively.

The diffusion volume within the diffusion length from the sensor was calculated as follow for the ISFET and the NW:

$$V_{ISFET} = (2L^2 + L(w_{ISFET} + 2L)) \cdot l_{ISFET}$$

$$\mathrm{V_{NW}} = \big(2\mathrm{L}(\mathrm{h_{NW}} + \mathrm{L})\big) + \mathrm{w_{NW}L}) \cdot \mathrm{l_{NW}}$$

Being w_{ISFET} and l_{ISFET} the width and length of the ISFET respectively and w_{NW}, h_{NW} and l_{NW} the width, height and length of the NW respectively.

Results listed below.

ISFET	D (m^2/sec)	L in 43sec (m)	V (m^3)	N (number of molecules)	C (M) for 43s	Time (s) For 10^{-10} M
Protons	$9 \cdot 10^{-9}$	$8.8 \cdot 10^{-4}$	$9.94 \cdot 10^{-10}$	$3.72 \cdot 10^{-14}$	$3.74 \cdot 10^{-8}$	$2 \cdot 10^{4}$
Hemoglobin (in water)	$6.9 \cdot 10^{-11}$	$7.7 \cdot 10^{-5}$	$2.52 \cdot 10^{-11}$	$3.72 \cdot 10^{-14}$	$1.48 \cdot 10^{-6}$	$2.7 \cdot 10^{6}$
DNA (in water)	$5.3 \cdot 10^{-11}$	$6.7 \cdot 10^{-5}$	$2.14 \cdot 10^{-11}$	$3.72 \cdot 10^{-14}$	$1.74 \cdot 10^{-6}$	$3.4 \cdot 10^{6}$

Nanowires	D (m^2/sec)	L in 43sec (m)	V (m^3)	N (number of molecules)	C (M) for 43s	Time (s) For 10^{-10} M
Protons	$9 \cdot 10^{-9}$	$8.8 \cdot 10^{-4}$	$2.17 \cdot 10^{-11}$	$1.06 \cdot 10^{-18}$	$4.8 \cdot 10^{-11}$	21
Hemoglobin (in water)	$6.9 \cdot 10^{-11}$	$7.7 \cdot 10^{-5}$	$1.67 \cdot 10^{-13}$	$1.06 \cdot 10^{-18}$	$6.36 \cdot 10^{-9}$	$2.74 \cdot 10^{3}$
DNA (in water)	$5.3 \cdot 10^{-11}$	$6.7 \cdot 10^{-5}$	$1.28 \cdot 10^{-13}$	$1.06 \cdot 10^{-18}$	$8.3 \cdot 10^{-9}$	$3.6 \cdot 10^{3}$

This reinforces our conclusion that for low concentrations Fin-FETs approaches the performance of NWs.

References

1. Ortiz-Conde A., Garcia Sanchez F.J., Liou J.J., Cerdeira A., Estrada M., Yue Y., A review of recent MOSFET threshold voltage extraction methods, Microelectronica reliability 42, 583-596 (2002)
2. Bergveld P., ISFET, Therory and Practise, IEEE SENSOR CONFERENCE TORONTO (2003)
3. Butt H.J., Karlheinz G., Michael K., Physics and Chemistry of Interfaces, Wiley-VCH Verlag & Co. KGaA ISBN: 3-527-40413-9
4. Mortimer, R.G.. Physical Chemistry Third Edition. Elsevier Academic Press 2008, page 474
5. Milo, R.; Phillips, R. Cell Biology by numbers. Garland Science, Taylor & Francis Group, Chapter 4, pp. 259

Chapter 4

HIGH PERFORMANCE FIN-FET ELECTROCHEMICAL SENSOR WITH HIGH-K DIELECTRIC MATERIALS

In this chapter I present the integration of Fin-FETs devices with SiO_2, aluminium oxide (Al_2O_3) and hafnium oxide (HfO_2) as pH sensitive layer. I compare the pH sensitivity of such oxides and relate it to intrinsic material properties. I comment on the output characteristics of Fin-FETs with different oxides (SiO_2 and HfO_2) but similar dimensions and the improvements that high dielectric constant materials bring to the device. I fit the experimental data with the developed electrochemical model as described in the supporting information of chapter 3 to extrapolate the dielectric constant of HfO_2. I deploy the devices to study the acidity of citrus juices and comment on the oxides stability.

This chapter is based on the published paper in Sensors and Actuators B: Chemical "High Performance Fin-FET electrochemical sensors with high-K dielectric materials", S. Rollo, Dipti Rani, W. Olthuis, C.P. García, arXiv:1907.11022.

4.1 Abstract

In this work we combine a Fin Field Effect Transistor (Fin-FET) characterised by a high height to width aspect ratio with high-k dielectric materials to study the optimized design for chemical-FETs to provide higher transconductance (and thus a better signal to noise ratio), increased dynamic range and chemical stability. We used pH sensing to verify the design. We explored the sensitivity and response linearity of silicon dioxide, alumina and hafnium oxide as dielectric materials sensing pH, and compared their chemical stability in different acids. The high aspect ratio fin geometry of the sensor provides high currents, as well as a planar conduction channel which makes them more reproducible towards fabrication than traditional silicon nanowires. The hafnium oxide Fin-FET configuration performed the best delivering the most linear response both for the output and transfer characteristics, providing a wider measurable dynamic range. Hafnium oxide also showed the best chemical stability. Considering analysis of sensor response time to analytes with the diffusion coefficient of DNA and proteins, the Fin-FETs configuration improves the mass transport at low concentrations and reduces the footprint enabling higher multiplexing capability with respect to planar ISFETs and NWs arrays. Also, it improves linearity of the output signal with concentration, reproducibility towards fabrication and results of the assays, and intensity of the output signal with respect to NWs. Overall we think this can represent the best compromise to FETs electrochemical sensors.

4.2 Introduction

Bio-Field Effect Transistors (Bio-FETs) are FET based sensors combined with a biological recognition element able to sense biomolecules. They are an interesting alternative for label free detection of biomarkers in the fields of genomics[1-3] and proteomics[4-6] for applications in medical diagnostics, drug discovery and basic research, offering multiplexing capability, portability and

miniaturisation, real-time analysis, selectivity, low cost. Despite these desirable features, there is not yet a portable, low cost device in the market based on this technology. In fact, there are challenges to overcome when scaling up from the lab to the industry level related to the reliability of the performance among devices, the functionalization with the bio-recognition element and the chemical stability of the surface[7-9] in particular for applications that require an extended contact over time of the sensor surface with the sample fluid. To improve the performance of Bio-FETs and chemical-FETs in general the original design of planar devices evolved into nano-sensors like nanowires[10], and new materials were introduced to increase the transduced signal and chemical stability of the interface[11-13]. Owing to the miniaturisation achieved by nanowires, the limit of detection of label free sensing increased from µM to fM and the incubation time needed for heavy molecules to reach the equilibrium decreased from days to hours or minutes[14,15]. Nevertheless the lower detection limits of nano devices come at the cost of impacting negatively the signal to noise ratio since the small variation of the signal (nA or pA) in the order of the noise are more difficult to attribute to the biorecognition event, as well as smaller currents require more sophisticated instrumentations. Also, the nano dimensions impact the variability of the current signal among devices and thus the reproducibility of the assay[16,17]. Recently we proposed a Fin-FET design with a high aspect ratio of the height to width (>10), in which the width of the sensor was comparable to that of nanowires, but due to the bigger height, it resulted in a planar conduction channel[18]. This change in the geometry improved the signal to noise ratio and the linearity of the output signal, and provided a higher surface area, which is favourable for the reliability of the functionalisation as compared to nanowires. The device design provides a compromise to increase the total signal, while providing a good response time for assays at low concentrations, for which the sensing is diffusion limited[19].

The dielectric interface of the FET in contact with the electrolyte is a key component of the sensor as it determines its chemical stability[20] as well as

the transduction. It can be used as receptor for simple molecules or ions in solution such as protons[21,22] or as the support for the functionalisation of biorecognition layers that improve the selectivity of the sensor[23]. In the case where the interface is directly used to capture molecules, the surface chemical properties of the dielectric itself determine the surface potential that regulates the conductivity of the transistor across the source to drain channel. The conduction is also affected by the dielectric constant (k) of the material that determines the capacitance effect between the sensor surface and the conduction channel. The fabrication of devices with silicon dioxide (SiO_2, ε_{SiO2} ~3.9) as dielectric interface is convenient but it is not preferable since SiO_2 has low pH buffer capacity in comparison to other dielectric materials and it suffers from drift, hysteresis, leakage currents, and penetration of ions when in contact with the electrolyte for an extended period of time[24,25]. Other dielectrics such as aluminium oxide (Al_2O_3)[11,12,26] , hafnium oxide (HfO_2)[12,27] and tantalum pentoxide (Ta_2O_5)[28,29] can be used to improve the sensor properties, being more resistant to ion penetration and providing a higher dielectric constant (~9, ~25, ~22 for Al_2O_3, HfO_2 and Ta_2O_5 respectively) that increases the transconductance further by increasing the capacitive effect in the semiconductor even with physically thicker layers. Combining the design of a high aspect ratio Fin-FETs with high-k dielectrics can enhance their specific advantages, improving the superior linear response of the output current and increasing the sensitivity and signal to noise ratio by improved transconductance responsible of the signal transduction. The whole device design also take advantage of the better chemical performances of high-k materials, which improves reliability and stability. Materials with better chemical performance meaning higher intrinsic buffer capacity, while also being more resistant to dissolution in both acidic and basic conditions have the potential to provide reliability and stability for the device.

To measure the impact of the dielectric in FETs, the detection of the acidity of a solution in aqueous electrolytes (pH) has been used as a direct

comparison of the performance among different oxides[30,31]. The response of the dielectric towards pH can be described using the combined Gouy-Chapman-Stern and Site-Binding (GCS-SB) models, where the GCS model describes the electrical double layer that forms at the oxide interface, and the SB model describes the grade of ionization (protonation or deprotonation) of the surface chemical groups of the dielectric barrier[32]. Using both models it is possible to derive the relationship between the bulk pH and the potential at the oxide surface (Ψ_0), characterised by the oxide sensitivity $\Delta\Psi_0/\Delta pH$, which determines the chemical response of the material. Silicon oxide shows pH sensitivities of 20 to 40 mV/pH depending on the quality of the grown layer, and a nonlinear response in a wider pH range due to its low intrinsic buffer capacity[33-36]. Al_2O_3,HfO_2 and Ta_2O_5 have shown sensitivities equal or higher than 55 mV/pH, and improved linearity in a wide pH range[11,12,30,37]. HfO_2 and Ta_2O_5 have similar values of the dielectric constant but the conduction band offset with silicon is 0.34 and 1.4 respectively for the two materials[38]. Higher band offsets are preferable in order to have low leakage currents. This makes HfO_2 a better choice than Ta_2O_5, which also suffer of light induced drift[39]. An ultimate design of a FET sensor has to combine the sensor geometry with the effect of the dielectric material on the transduction of the surface properties on the chemical performance (sensitivity and stability).

In this work we combine a p-doped high aspect ratio Fin-FET design with different dielectrics as thermally grown SiO_2 and atomic layer deposited Al_2O_3 and HfO_2 on a thin SiO_2 interface layer, which were the oxides available in our facilities. ALD deposited Al_2O_3 has been widely used as sensing dielectric layer in electrochemical FET sensors so we could compare our grown material with the existing literature. HfO_2 is a higher-k material than alumina, with better chemical stability, which promises the best performance. We have studied the pH sensitivity in terms of variations of Ψ_0, which we relate to the intrinsic properties of the material (dissociation constants of the surface active groups and surface density of the surface reactive sites). We also compare the effects

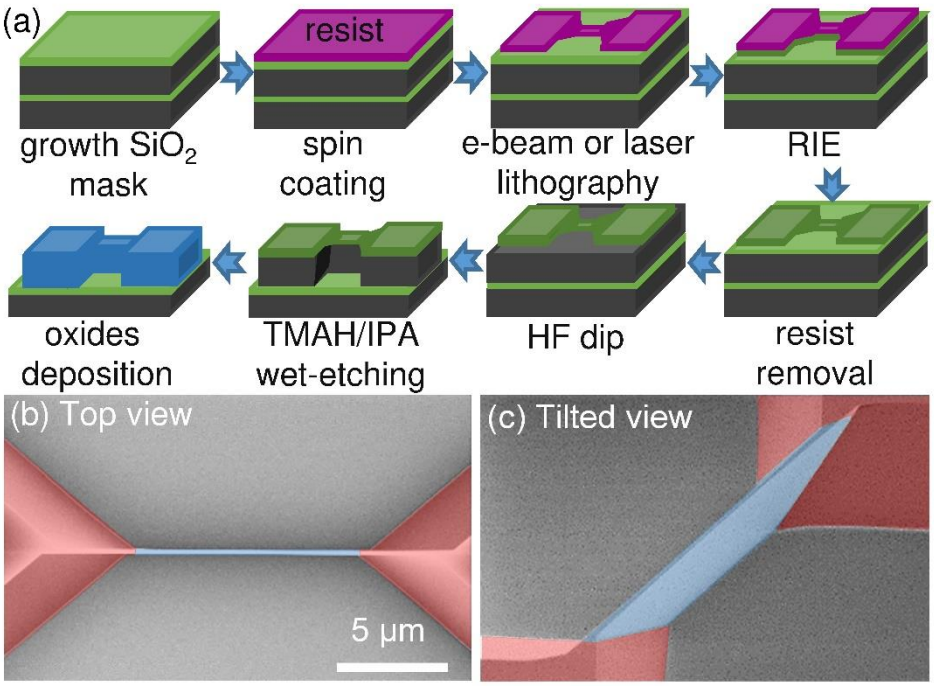

Figure 4.1 (a) Schematic representation of the fabrication process of Fin-FETs on SOI substrates based on laser or e-beam lithography on a negative resist, and wet etching in a TMAH/IPA wet etching solution. Silicon is represented in dark grey while silicon oxide is represented in green. The resist is depicted in purple and the final oxide as sensing layer in blue. (b) and (c) Top and tilted SEM pictures respectively of one representative Fin-FET device after fabrication. The silicon body of the device standing on the grey buried oxide and the contacts are shadowed in blue and red, respectively.

of transducing the variations of Ψ_0 within two similar Fin-FET devices with SiO_2 and HfO_2, respectively. Using a Nernst-Poisson model[18], we calculate the effective dielectric constant of the stack SiO_2/HfO_2. Finally, we test the stability of the three oxides comparing a controlled citric acid buffer with natural citrus juices. We proved that while Al_2O_3 represent an improvement to SiO_2, HfO_2 provides the best chemical stability in time and overall enhances the transduction properties of the Fin-FETs. Owing to the combination of the high aspect ratio of the sensors configuration with the high-k and chemically stable HfO_2 we report the highest performance of this configuration of an electrochemical sensor, with results comparable to literature.

4.3 Experimental methods

4.3.1 Silicon Fin-FETs fabrication

We fabricated silicon Fin-FETs by anisotropic wet etching of p-doped silicon on insulator (SOI) substrates with a 2 ± 0.1 and 3 ± 0.1 µm thick silicon device layer (<110> oriented) with resistivity of 0.115 Ω·cm (equivalent doping $10^{17}/cm^3$) and a 1 µm thick buried SiO_2 procured from Ultrasil Corporation. The substrates were diced in chips of 1 x 1 cm^2 before starting the fabrication of the Fin-FETs. Briefly, we used Maskless photolithograpy (MLA 150 Heidelberg Instruments) and e-beam lithography (FEI Helios electron microscope) on the negative resist ma-N 2403 to pattern lines with widths ranging from 400 to 700 nm on a thermally grown thin SiO_2, oriented along the <110> direction parallel to the primary flat of the substrate in order to get the desired shape after wet etching. The Fin-FET shape originates from the different rates at which the <110> and the <111> planes are etched. The device lateral walls lay on the <111> planes. The etching along the vertical direction (<110> plane) is about 10 times faster than along the <111> planes. Knowing the plane dependent etching rates[36] and device layer thickness of Si, lithography mask was designed with defined line widths to have final wire width on the chips. The connection between the lines and the contact pads was achieved through approaching pads with a triangular footprint designed at the angles of ≈54.7° and 35.3° with respect to the primary flat to provide a smooth profile between the channel and the pads after etching. This pattern was then transferred to the previously thermally grown oxide by Reactive Ion Etching (RIE) through a CF_4 process of 15 minutes at a pressure of 75 mTorr and power of 25 W. The samples were then treated with HF to remove the excess of oxide outside the lithographed area and to obtain a smooth surface. The anisotropic etching was achieved with a 25 % wt Tetramethylammonium hydroxide, 8.5 %vol of isopropanol water solution lasting for ≈23 and ≈30 minutes for the complete etching of the 2 and 3 µm thick substrates, respectively. After a 1 minute dip in HF to remove the SiO_2 mask, samples were ready for the deposition of the gate oxide stacks. We used 20 nm of

thermally grown SiO_2, and 10 nm atomic layer deposited (ALD) Al_2O_3 and HfO_2 with 7 nm of SiO_2 thermally grown as interlayer between the silicon and the ALD grown oxides, measured by ellepsometry, to have the pH sensitive layers. First we grow a thin layer of SiO_2 on our devices to ensure a smoother interface, which would also reduce pin-holes and leakages. Then we deposited the same thickness of Al_2O_3 and HfO_2 to approximately the same value as the devices with SiO_2. Indeed, all of them can be considered of similar values within the error margins of our thickness measurement equipment (3nm)." Figure 4.1 (a) schematically shows the fabrication steps. Figure 4.1 (b) and (c) show Scanning Electron Microscope (SEM) pictures of a representative device with top and tilted views respectively. The high aspect ratio Fin-FET channel is shadowed in blue between the source and drain contact pads which are shadowed in red. The ohmic contacts and the leads necessary for the integration into a plastic circuit board (PCB) were defined by optical lithography on regions of the devices shadowed in red part. The ohmic contacts were a Ti/Al/Au stack (2/160/5 nm) e-beam evaporated, while the leads were Au 150 nm. Another lithography step on an epoxy (SU8) allowed to open windows on the Fin-FET region while protecting the contacts. After wire bonding to the PCBs dipstick, the samples were protected with a medical grade epoxy glue (Loctite EA M-31CL, Henkel). The final devices had a length of 14 µm at the middle of the Fin-FET and width ranging from 150 to 400 nm. Each chip contained eleven Fin-FETs. Table 4.1 summarizes the characteristics of thickness of the deposited oxide (t_{ox}), average width (w) of the devices on the same chip with the same oxide, and height (h) of the fabricated devices.

Table 4.1 Characteristics of thickness of the deposited oxide (t_{ox}), and width (w) and height (h) of the fabricated devices.

Device oxide	t_{ox} (nm)	w (nm)	h (µm)
SiO_2	20	≈170	2
Al_2O_3	10	≈400	2
HfO_2	10	≈200	3

4.3.2 pH sensitivity characterization

Experiments of pH sensitivity were carried out in buffer solutions with pH ranging from 3 to 11 in step of 1. The buffers were prepared by mixing a solution of KH_2PO_4, citric and boric acids at 0.1 M all, with a KNO_3 0.1 M solution in equal volume proportion, for a final pH of 2.5. More basic pH were obtained by addition of a 0.1 M solution of KOH. All the solutions were prepared using Milli-Q water as solvent. With this procedure, the total ionic strength remained constant at 0.1 M. For the electrochemical characterization the chips were immersed into the buffer solutions with a calomel reference electrode (BioLogic R-XR300) for biasing the electrolyte and a commercial pH meter (Sentron SI600) to check the pH throughout the measurements. We used a Keithley 2614HB DC source meter to apply the voltage between the source and drain contacts and to the reference electrode. We used a multiplexer Keithley 3706A System Switch/Multimeter connected to a switching box to characterize the devices in sequence.

4.3.3 Measurements of acidity in citrus juices

We prepared a solution of citric acid 0.01M by dissolving 0.48 g in 250 mL of Milli-Q water. The resulting solution had an acidic pH of 3 measured with a commercial pH meter. The lemon and orange juices were obtained from freshly squeezed fruits and filtering the pulp. Their pH was also measured first with the pH meter, resulting in pH 2.7 and 4.1 for the lemon and orange juice respectively. For the measurements of citric acid we used the same set-up described in the paragraph above.

4.4 Results and discussion

4.4.1 Surface sensitivity of Fin-FETs with SiO_2, Al_2O_3, HfO_2

In order to determine the surface sensitivity of the grown oxides, we measured the transfer characteristics, source drain current (I_{ds}) *vs.* reference

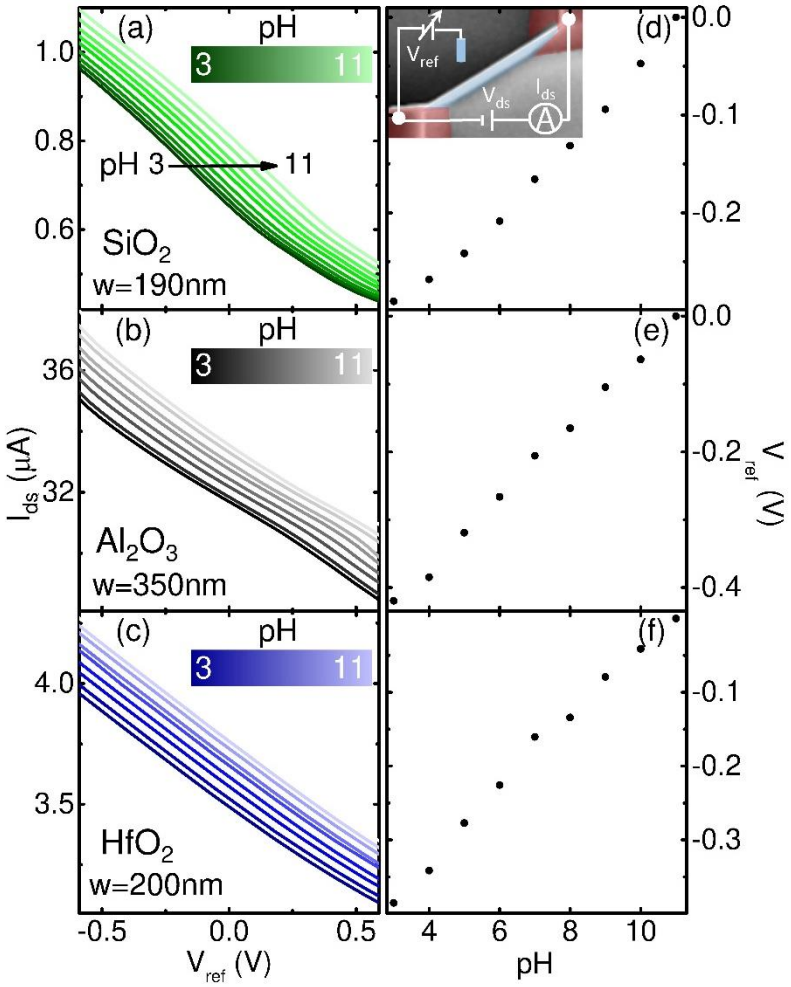

Figure 4.2 (a) to (c) Examples of transfer characteristics I_{ds} vs V_{ref} at fixed V_{ds}' for three representative devices with the three different oxides. The curves were measured in buffers at pH 3 to 11 represented with a coloured scales. The width of the devices is referred as w. The inset in (d) represent a schematic of the measurement setup. (d) to (f) V_{ref} vs pH measured from the curves in (a) to (c) as shifts of V_{ref} at each pH to maintain a constant current.

electrode voltage (V_{ref}), at constant source drain voltage (V_{ds}'). The inset of fig. 2 (d) reports a scheme of the measuring set up. The pH sensitivity ($\Delta V_{ref}/\Delta pH$) was evaluated from the shift of the transfer curves at a constant current with different buffers pH values. The variations of the reference electrode voltage (ΔV_{ref}) compensate (and correspond to) the changes in the surface potential ($\Delta \Psi_0$) induced by the different proton concentrations. The

choice of V_{ds} followed from a preliminary characterization performed at neutral pH and V_{ref}' = 0 V. For this characterization we measured the output characteristics I_{ds} *vs.* V_{ds} from all devices. At higher V_{ds} values we observed a bending of the curves which we interpreted as the pinching off of the carrier density in the channel. We restricted the study to the linear range of I_{ds} versus V_{ds} in order to be able to explain the variation of the conductance of the device with the ohmic contribution of the conducting channel cross section, and its dimensions. To this objective, for the characterization we used the maximum V_{ds} value beyond which we started observing a variation from linearity, being a V_{ds}' of 0.1 V for the narrower devices (like the ones reported for SiO_2 and HfO_2), and 0.5 V for the wider ones (like the ones reported for Al_2O_3), while V_{ref} was swept in a range between -0.6 and 0.6 V in all cases. The transfer characteristics were acquired in a pH range between 3 and 11 in steps of 1 by immersing the samples into the buffer solutions. Multiple Fin-FETs on three different chips having the three oxides as pH sensitive layers were characterized with the same procedure. Figure 4.2 (a) to (c) show the transfer characteristics of three representative devices from each type family of dielectrics. At each oxide is attributed a colour and different shades are used to indicate the 1 unit pH change between the measurements, according to the coloured scales as shown in fig. 4.2 (a) to (c). The width of the tested devices (w) is also specified, which is not relevant in this study of pH sensitivity related to the dielectric. In each case we observed a shifting of the transfer characteristics toward more positive V_{ref} while moving from acidic to basic buffers. This is because the majority carriers in the semiconductor channel are holes affected by Ψ_0. When the pH increases there are less protons interacting with the oxide surface, thus lower Ψ_0 compared to more acidic conditions. Therefore higher V_{ref} is required to compensate the electrostatic potential at the oxide liquid interface to maintain a constant current flowing through the channel. Figures 4.2 (d) to (f) show the shift of V_{ref} with pH in the curves in fig. 4.2 (a) to (c) derived as the V_{ref} necessary to keep the value of I_{ds} at pH = 11 at V_{ref}=0 V constant, which corresponds to the variations of Ψ_0 due to the different proton concentrations. The relation between the surface

potential and the pH is derived by combining the electrostatic interactions at the dielectric surface and the distribution of ions inside the electrolyte starting from the oxide surface, which was found earlier[30]:

$$\frac{\Delta\Psi_0}{\Delta pH_B} = -2.303\frac{k_B T}{q}\alpha \qquad \text{Eq. 4.1}$$

Where pH_B, k_B, T and q represent the pH in the bulk electrolyte, the Boltzmann constant, the absolute temperature and the elementary charge, respectively. α is a sensitivity parameters with a value varying between 0 and 1 depending on intrinsic properties of the oxide. For α=1 the sensor has a so called Nernstian sensitivity of 59.2 mV/pH at 298 K. We obtained an estimation of the sensitivity of the different oxides from the linear fit of the curves like the ones showed in fig. 4.2 (d) to (f) acquired from all the devices, obtaining the average value of the sensitivity, and the standard deviation for each type of oxide. We found that the response of the dielectrics to different proton concentrations, which experimentally translates into a shift of the transfer characteristics at different pH values, were qualitatively similar among Fin-FETs with the same oxide. Al_2O_3 provided the best performance in terms of sensitivity with 54.2 ± 1.9 mV/pH, while the one for HfO_2 was 49.8 ± 0.6 mV/pH. For both oxides the experimental results are in agreement with other values of sensitivities reported in literature[11,12,26,27]. While Al_2O_3 and HfO_2 have an approximately linear response in the pH range considered, SiO_2 has a lower sensitivity in acidic conditions compared to basics due to the lower intrinsic buffer capacity of the oxide surface at low pH where the groups at the surface interacting with the protons in electrolyte are close to saturation and are not able to buffer the changes of proton concentration. In the pH range between 6 and 11, where silicon oxide has the highest sensitivity, we estimated a value of 42.1 ± 0.5 mV/pH. Close to saturation (i.e. at the point of zero charge of the oxide surface, pH_{pzc}) at pH lower than 6, we estimated a sensitivity of 30.2 ± 1.1 mV/pH. These values are also in agreement with other values reported in literature[31-34].

The origin of the different pH sensitivities among the different oxides can be explained in terms of the acidic and basic dissociation constants (K_a and K_b, respectively) of the reactive groups (hydroxyls –OH able to exchange protons) from each oxide surface, and the surface density of surface reactive sites (N_s). The combination of the Site Binding model which describes the reactivity of the hydroxil groups with the Gouy-Chapman-Stern model, which describes the formation of an electrical double layer at the oxide/electrolyte interface gives an expression for the sensitivity parameter α in eq. 1 containing the differential capacitance C_{diff} and the intrinsic buffer capacity β_{int}.

$$\alpha = \frac{1}{\frac{2.303kTC_{diff}}{q^2\beta_{int}}+1} \qquad \text{Eq. 4.2}$$

The differential capacitance depends on the electrolyte (solvent dielectric constant and ionic strength), while β_{int} depends on K_a, K_b, and N_s and is linked to the ability of the oxide to buffer small changes of surface charge[32]. Higher values of β_{int} are related to more reactive surfaces, thus improved sensitivities. From the experimental pH sensitivities, we evaluated α using eq. 1. We also estimated C_{diff} using the estimation of C_{diff} presented in literature by Van Hal et al. that modelled C_{diff} as the series capacitance of the Stern capacitance C_{St} (the contribution of the layer of charges in closest contact with the oxide) and the diffuse layer capacitance C_{DL} (from Gouy and Chapman)[32]. C_{St} has been theoretically calculated for different ionic strengths of the electrolyte[41], and we used the same value considered by Van Hal et al. of 0.8 F/m^2. For the estimation of C_{DL} it is assumed that the total charge in the diffuse layer (σ_{DL}) is equal to the charge at the oxide surface (σ_0), which yields the expression for C_{DL} derived by Van Hal et al.[32]:

$$\sigma_{DL} = -(8kT\varepsilon_0\varepsilon_w n^0)^{1/2} sinh\left(\frac{zq\Psi_0}{2kT}\right) = -C_{DL}\Psi_0 = -\sigma_0 \qquad \text{Eq. 4.3}$$

Where ε_0, ε_w and n^0 are the vacuum and water relative permittivities and the number concentration of each ion of the electrolyte, respectively. Using eq. 4.3 we calculated the experimental C_{diff} for an electrolyte with a 0.1 M ionic

strength as the one we used in our experiments, and combining with the experimental sensitivity in eq. 2 we calculated the experimental buffer capacity β_{exp}. We compared β_{exp} with the intrinsic buffer capacity calculated using literature values of the acidic and basic dissociation constants of the surface reactive groups (K_a, K_b), and surface density of surface reactive sites (N_s)[30,32,42] according to the expression for β_{int} given by Van Hal et al., as reported in SI 4.1. We obtained β_{exp} of 0.6 x 10^{18}, 1.5 x 10^{18} and 1.7 x 10^{18} groups/m^2, for SiO_2, Al_2O_3 and HfO_2 respectively, compared to the theoretical values β_{th} of 0.9 x 10^{18}, 3.7 x 10^{18} and 2.8 x 10^{18} groups/m^2, respectively. In each case we noticed that the experimental values of intrinsic buffer capacity are lower than the theoretical ones. The difference may be attributed to the different way the oxides are grown, the presence of impurities on the oxide surface and defects coming from the deposition step that affect the total number of reactive sites.

4.4.2 Relevance of Fin-FETs integration with high-k dielectrics

Higher k dielectrics yield improvements to the sensor. Fin-FETs with high aspect ratio show more linear and higher transconductance $\Delta I_{ds}/\Delta pH$, respect to SiNWs[18]. We expect that higher k dielectrics will further improve the output characteristics of these devices. We compared the conductance of two Fin-FETs devices with the two oxides having the most different dielectric constants, meaning the ones with 20 nm thermally grown silicon oxide and the one with 10 nm of hafnium oxide grown on a 7 nm silicon dioxide interface layer, for a total thickness of about 17 nm. Both devices had approximately the same base width and length (190 nm and 14 µm, respectively), and heights of 2.16±0.1 and 2.90±0.1 µm for the SiO_2 and HfO_2, respectively (measured by profilometry). Despite the different heights of the two devices, we could compare the results by normalizing with respect to their cross section, which excluded the contribution of the different heights. The output characteristics I_{ds} vs V_{ds} were explored in a pH range from 3 to 11

with V_{ref}' = 0 V . We choose this value of V_{ref} since at neutral pH I_{ds} was linear in a range of V_{ref} between -200 and 200 mV, which is the variation of surface potential expected in the considered pH range. Thus I_{ds} can be described with the ohmic contribution of the non-depleted region with a Nernst-Poisson model. I_{ds} was acquired sweeping V_{ds} between -100 and 100 mV. I_{ds} had a linear behaviour in that range as shown in fig. 4.3 (a) for the devices with SiO_2 and HfO_2 using colour scales for pH between 3 and 11 with steps 1. The measuring setup is also shown schematically in the inset of fig. 4.3 (a). From the data in fig. 4.3 (a) we estimated the conductance (G) as the slope of the linear fittings. In fig. 4.3 (b) we report the conductance of the two Fin-FETs with the different sensing oxides normalized by the cross section of the device, to take into account the difference in height between both devices and allow a comparison. The experimental data are represented as green triangles and blue dots for the devices with SiO_2 and HfO_2, respectively. The conductance increases towards more basic pH values in both cases as I_{ds} depends on the surface potential Ψ_0 which depends on the proton concentration as already explained. The variation of the conductance we obtained was of 522 ± 12mS/pH and of 912 ± 19mS/pH per unit area for the SiO_2 and the HfO_2 devices respectively. The effect of enhanced variation of the conductance in the device with HfO_2 is due to the contribution from the higher intrinsic sensitivity of the material $\Delta\Psi_0/\Delta pH$, and to the higher dielectric constant, which increases the transconductance in the device. The higher linear response of the HfO_2 pH surface sensitivity is transfer to the output response. The higher sensitivity offered by HfO_2 through the whole acidity range combined with the high aspect ratio fin geometry of the sensor channel offers better performances in a wider dynamic range.

We estimated the dielectric constant of the HfO_2 layer (ε_{HfO2}) using a Nernst-Poisson model to fit the experimental data (blue line in fig. 4.3 (b)) combined

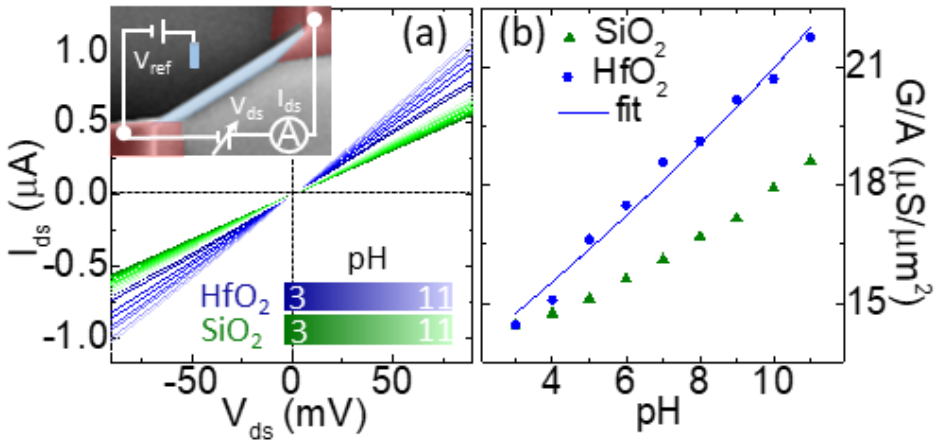

Figure 4.3 (a) Output characteristics I_{ds} vs V_{ds} at fixed V_{ref}' = 0 V for the SiO_2 and HfO_2 Fin-FETs respectively. The curves at different pH are coloured according to the scales in the inset. A schematic of the measuring setup is also shown as inset. (b) Normalized conductance vs pH for the Fin-FETs having approximately the same width with SiO_2 and HfO_2 as pH sensitive layers, calculated from the curves in fig. 3 (a). The fitting of the experimental data with the Nernst-Poisson model used to estimate the dielectric constant of the deposited HfO_2 is represented as a blue line.

with the experimental sensitivity parameter α retrieved from the $\Delta V_{ref}/\Delta pH$. The model is based on eq. 4.1 to describe the dependence of Ψ_0 with pH that modulates the Poisson distribution of charges determining the depleted region that lastly controls the output current (a detailed description was provided in the supporting info of chapter 3). The effective dielectric constant ε_{eff} of the SiO_2/HfO_2 stack was modelled with two capacitors in series from each oxide layer with known thicknesses (t_{SiO2}= 7 nm and t_{HfO2} =10 nm measured during the growth in a dummy sample with ellipsometry):

$$\varepsilon_{eff} = \frac{(t_{SiO2}+t_{HfO2})\varepsilon_{SiO2}\epsilon_{HfO2}}{t_{SiO2}\varepsilon_{HfO2}+t_{HfO2}\varepsilon_{SiO2}} \qquad \text{Eq. 4.4}$$

Considering the dielectric constant for SiO_2 ε_{SiO2} = 3.9 we obtained ε_{eff} of 7.4 and thus from eq. 4.4 $\varepsilon_{HfO2} \approx 20$, which is in agreement with other values in literature for ALD deposited HfO_2[37,43]. The integration of high aspect ratio Fin-FETs sensors with high-k materials provided the best performance in the output currents for linearity and sensitivity.

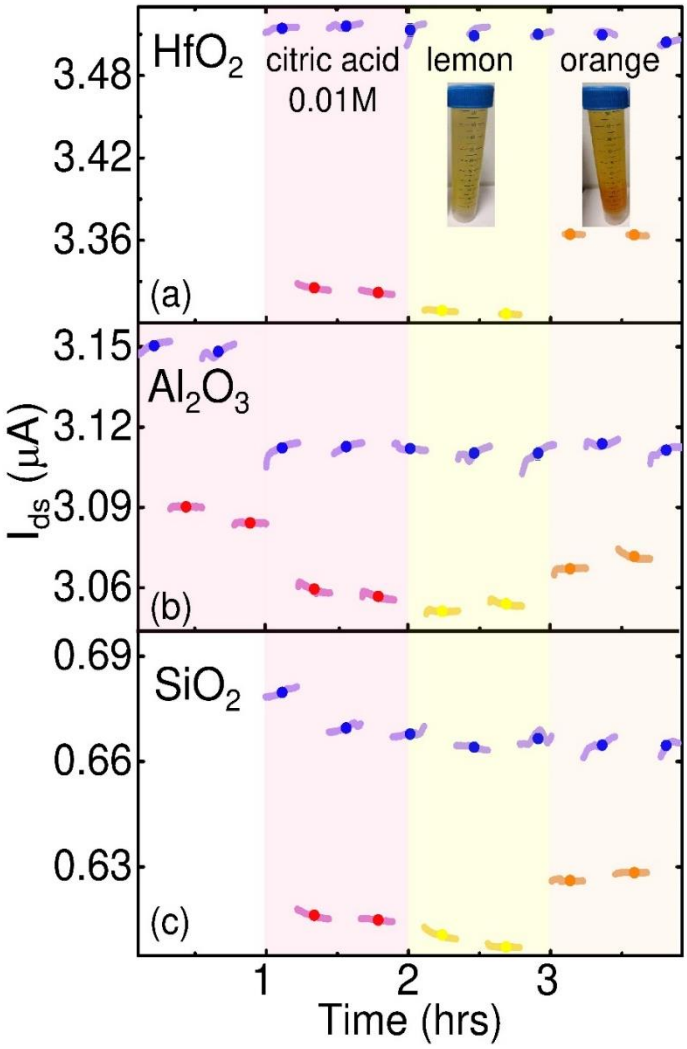

Figure 4.4 (a) to (c) Output current I_{ds} vs time from three Fin-FETs devices with the three different oxides in different media represented in different colours. The current was recorded for 15 minutes after each change of fluid after five minutes of stabilization time. In the same graphs the current data are also reported as average value of I_{ds} and standard deviation in the 15 minutes of the measurement. Pictures of the citrus juices used in the experiments are shown as an inset.

4.4.3 Stability of the oxides in different acidic media

To study the stability over time of the different oxides in contact with fluids, we used the Fin-FETs with the three different interfaces to sense the acidity of squeezed lemon and orange juices where the main component responsible of the acidity is citric acid (7%, and 4-5%, concentration for lemon and orange

juice, respectively). We compared the behaviour of the devices in citric juices with a 0.01 M citric acid buffer (pH 3) monitoring the fluctuations of the output current while moving the sensors from one liquid to another. We tested a family of devices for each oxide with a common external reference electrode moving the devices alternatively between water and the other acid solutions every 15 minutes and waiting five minutes before starting the next measurement to allow the stabilization of the sensor. To avoid cross contamination the sensors were rinsed with deionized water and blow dried with nitrogen in between each exchange of solutions. Figure 4.4 shows the output currents and average values (using dots) for each cycle of the same devices shown in fig. 4.2. The water, citric acid buffer, lemon and orange juices solutions are represented with blue, red, yellow and orange colours, respectively. The insets shows pictures of the juices liquid samples used in the experiments. HfO_2 showed a very reproducible behaviour throughout the measurements. The current returned to approximately the same values

depending on the pH of the solution with a drift < 10 nA (~5% of the measured range) along three hours of measuring time. This was not the case for Al_2O_3 and SiO_2. Specifically the current in the device with Al_2O_3 showed an abrupt change of about 40 nA (> 60%) after 1 hour followed by an stabilisation. Then the device behaved similarly to the SiO_2 one, which in three hours had a drift of 12 nA (~15%). We attribute the abrupt change in the Al_2O_3 to the corrosion by citric acid which provokes the detachment of material especially in the pH range 3-6 as reported in literature[44]. After the Al_2O_3 layer was totally corroded the SiO_2 beneath was exposed stabilizing the device. In the transfer characteristics recorded after the experiment we noticed a decrease of the pH sensitivity in line with values reported for SiO_2 (see SI 4.2), which support our hypothesis. In the SiO_2 device the drift during the first hour is attributed to the intrinsic drifting normally observed in silicon oxide[24,45]. SiO_2 suffers issues of ions reactions and incorporation when in contact with electrolyte for an extended period of time which affects the oxide stability until an equilibrium is reached between the reactive groups at the oxide

surface and ions in the solution, and the stability restored[24]. As discussed before, we obtained higher total average sensitivity for the HfO_2 Fin-FETs with a $\Delta R/R$ = 6.9% (R refers to resistance of the device) between pH 7 and 2.8 compared to that of the SiO_2 FinFETs of $\Delta R/R$ = 5.9% in the same range (after normalization to the cross section to take into account for the different heights).

4.5 Conclusions

In this work we investigated the surface sensitivity of different dielectric materials and the way they influence the transconductance in high aspect ratio Fin-FET chemical sensors. The chemical affinity of the different hydroxyl groups at the surface of the dielectrics provides the surface sensitivity of the material, which was tested by acidity measurements in a pH range from 3 to 11. We obtained surface sensitivities of 54.2 ± 1.9 mV/pH, 49.8 ± 0.6 and 37.5 ± 1.3 mV/pH for Al_2O_3, HfO_2 and SiO_2 respectively. While Al_2O_3 and HfO_2 had an approximately linear variation of the surface potential throughout the range investigated (pH 3-11), SiO_2 showed a lower sensitivity in acidic conditions attributed to the saturation of the reactive groups on the surface at low pH, next to the pH_{PZC}. We evaluated the experimental intrinsic buffer capacity (β_{int}) of the three oxides observing the poorer sensitivity of SiO_2 among the three oxides. We also investigated the effect of SiO_2 and HfO_2 on the transconductance of the Fin-FETs and observed an almost doubled response for the HfO_2, which we attribute to the enhanced surface sensitivity of the material as well as to the higher dielectric constant. This high aspect ratio Fin-FET/HfO_2 dielectric combination allows to increase the linearity of the output current and thus the dynamic range of the devices.

We investigated the stability of the three oxides when exposed to liquids for a long period of time by monitoring the fluctuations of the output currents of the three Fin-FET families of oxides. We measured the acidity of different liquids other than ideal buffer solutions, more specifically citrus juices, where

the acidity is mainly provided by the citric acid. In the device with HfO_2 the output current was stable, coming back at the same value after each change of the media. Along the three hours of the experiments we measured a drift of less than 5% of the measured range. For the device covered with Al_2O_3 we observed an abrupt change of more than 60% of the measured range after one hour, which we attributed to the corrosion of the material by the citric acid. The device with SiO_2 showed a drift of 15% of the measured range in the first hour, attributed to reactions of ions at the surface and ion incorporation, while the stability was restored after one hour.

In conclusion combining the Fin-FET geometry which intrinsically benefits an improved linearity in the transduction due to the 2D depletion along the width of the device, with high-k materials providing higher transconductance, improves the FET/dielectric material system offering higher performances of sensitivity and linearity of the sensors response to provide wider dynamic ranges and long term stability in liquid environment. These properties are all desirable features for biosensing applications and FET based biosensors development.

References

1. Y-C. Suy, W-E. Hsu, C-T. Lin, Review—Field-Effect Transistor biosensing: devices and clinical applications, ECS Journal of Solid State Science and Technology, 2018, 7 (7), Q3196-Q3207.
2. Q. Li, N. Lu, L. Wang, C. Fan, Advances in nanowire transistor-based biosensors, Small Methods, 2018, 2, 1700263.
3. H-Y Park et al., M-DNA/transition metal dichalcogenide hybrid structure based Bio-FET sensor with ultrahigh sensitivity, Scientific Reports, 6:35733, DOI: 10:.1038/srep35733.
4. R. Ahmad, T. Mahmoudi, M-S. Ahn, Y-B. Hanh, Recent advances in nanowires-based Field-Effect Transistors for biological sensor applications, Biosensors and Bioelectronics, 2018, 100, 312-325.
5. B. Ibarlucea et al., Gating hysteresis as an indicator for silicon nanowire FET biosensors, Applied Sciences, 2018, 8, 950.
6. I. Sarangadharan, S-H. Huang, W-C. Kuo, P-H. Chen, Y-L. Wang, Rapid detection of NT-proBNP from whole blood using FET based biosensors for homecare, Sensors & Actuators: B. Chemical, 2019, 282, 209-215.
7. G.A. Urban, Micro- and nanobiosensors—state of the art and trends, Measurements Science and Technology, 2009, 20, 012001.
8. M.J. Schöning, A. Poghossian, Bio FEDs (Field-Effect Devices): state-of-the-art and new directions, Electroanalysis, 2006, 18 (19-20), 1893-1900.
9. C. Siontorou, F.A. Batzias, V.A. Tsakiri, Knowledge-based approach to online fault diagnosis of FET biosensors, IEEE Transactions on Instrumentation and Measurements, 2010, 59 (9), 2345-2364.
10. M. Schwartz, T.C. Nguyen, X.T. Vu, P. Wagner, R. Thoelen, S. Ingebrandt, Impedimetric sensing of DNA with silicon nanowire transistors as alternative transducer principle, Physica Status Solidi A, 2018, 215, 1700740.
11. S. Chen, J. Bomer, E.T. Carlen, A. van der Berg, Al2O3/Silicon nanoISFET with near ideal Nernstian response, Nano Letters, 2011, 11, 2334-2341.

12. K. Bedner et al., pH response of silicon nanowire sensors: impact of nanowire width and gate oxide, Sensors and Materials, 2013, 25 (8), 567-576.
13. K. Malsagova et al., Micro-Raman spectroscopy for monitoring of deposition quality of high-k stack protective layer onto nanowire FET chips for highly sensitive miRNA detection, Biosensors, 2018, 8, doi: 10.3390/bios8030072.
14. J. Hahm, C.M. Lieber, Direct ultrasensitive detection of DNA and DNA sequence variations using nanowire nanosensors, Nano Letters, 2004, 4 (1), 51-54.
15. K.S. Kim, H-S. Lee, J-A. Yang, M-H. Jo, K. Hahn, The fabrication, characterization and application of aptamer-functionalized Si-nanowire FET biosensors, Nanotechnology, 2008, 20 (23), doi: 10.1088/0957-4484/20/23/235501.
16. S. Vitusevich, I. Zadorozhnyi, Noise spectroscopy of nanowire structures: fundamental limits and application aspects, Semiconductor Science and Technology, 2017, 32, 043002.
17. T.W. Wu, A. Alharbi, K-D. You, K. Kisslinger, E. Stach, D. Shahrjedi, Experimental study of the detection limit in dual-gate biosensors using ultrathin silicon transistors, ACS Nano, 2017, 11, 7142-7147.
18. S. Rollo, D. Rani, R. Leturcq, W. Olthuis, C. Pascual García, High aspect ratio Fin-Ion Sensitive Field Effect Transistor: compromises toward better electrochemical biosensing, Nano Letters, 2019, doi: 10.1021/acs.nanolett.8b04988
19. A. Alam, P.R. Nair, Performance limits of nanobiosensors, Applied Physics Letters, 2006, 88, 233120.
20. P.D. van der Wal, D. Briand, G. Mondin, S. Jenny, S. Jeanneret, C. Milon, H. Roussel, C. Dubourdieu, N.F. De Rooij, High-k dielectrics for use as ISFET gate oxides, IEEE SENSORS, 2004, 24, doi:10.1109/ICSENS.2004.1426257

21. Y-H. Chang, Y-S. Lu, Y-L. Hong, S. Gwo, J.A. Yeh, Highly sensitive pH sensing using an Indium Nitride Ion-Sensitive Field-Effect Transistor, IEEE Sensors Journal, 2011, 11 (5), 1157 – 1161.
22. J. Artigas, A. Beltran, C. Jimenez, A. Baldi, R. Mas, C. Dominguez, J. Alonso, Application of Ion Sensitive Field Effect Transistor based sensors to soil analysis, Computers and Electronics in Agriculture, 2001, 31, 281-293.
23. N. Chartuprayoon, M. Zhang, W. Bosze, Y-H. Choa, One-dimensional nanostructures based bio-detection, Biosensors and Bioelectronics, 20156, 3, 432-443.
24. I. Park, Z. Li, A.P. Pisano, R.S. Williams, Top-down fabricated silicon nanowire sensors for real-time chemical detection, Nanotechnology, 2010, 21, 015501.
25. S. Kum, D.W. Kwon, S. Kim, R. Lee, T-H. Kim, H-S. Mo, D.H. Kim, B-G. Park, Analysis of current drift on p-channel pH-sensitive SiNW ISFET by capacitance measurement, Current Applied Physics, 2018, 18, 568-574.
26. J-C. Chou, C-Y. Weng, Sensitivity and hysteresis effect in Al2O3 gate pH-ISFET, Materials Chemistry and Physics, 2001, 71 (2), 120-124.
27. C-S. Lai, T-F. Lu, C-M. Yang, Thickness effects on pH response of HfO2 sensing dielectric improved by rapid thermal annealing, JPN. J. Appl. Phys., 2006, 45, 3807-3810.
28. J-W. Kang, W-J. Cho, Improved pH sensitivity and reliability for extended gate Field-Effect Transistor sensors using high-k sensing membranes, Journal of Nanoscience and Nanotechnology, 2019, 19, 1425-1431.
29. T. Akiyama, Y. Ujihira, Y. Okabe, T. Sugano, E. Niji, Ion-Sensitive Field-Effect Transistors with inorganic gate oxide for pH sensing, IEEE TRANSACTIONS ON ELECTRON DEVICES, 1982, ED. 29, NO. 12, 1936-1941.
30. A. Tarasov et al., Understanding the electrolyte background for biochemical sensing with Ion-Sensitive Field-Effect Transistors, ACS Nano, 2012, 6 (10), 9291-9298.

31. P.V. Bobrov, Y.A. Tarantov, S. Krause, W. Moritz, Chemical sensitivity of an ISFET with Ta2O5 membrane in strong acid and alkaline solutions, Sensors and Actuators B: Chemical, 1991, 3 (1), 75-81.
32. R.E.G. Van Hal, J.C.T. Eijkel, P. Bergveld, A general model to describe the electrostatic at electrolyte oxide interfaces, Advances in Colloid and Interfaces Science, 1996, 68, 31-62.
33. D. Rani, V. Pachauri, A. Mueller, X.T. Vu, T.C. Nguyen, S. Ingebrandt, On the use of scalable nanoISFET arrays of silicon with highly reproducible sensor performance for biosensor applications, ACS Omega, 2016, 1, 84-92.
34. S. Chen, J. Bomer, W. van der Wiel, E.T. Carlen, A. van der Berg, Top-down fabrication of sub-30 nm monocrystalline silicon nanowires using conventional microfabrication, ACS Nano, 2009, 3 (11), 3485-3492.
35. Y. Cui, Q. Wei, H. Park, C.M. Lieber, Nanowire nanosensors for highly sensitive and selective detection of biological and chemical species, Science, 2001, 293 (5533), 1289-1292.
36. S. Kim et al., Silicon nanowire Ion Sensitive Field Effect Transistor with integrated Ag/AgCl electrode: pH sensing and noise characteristics, Analyst, 2011, 136, 5012-5016.
37. B.R. Dorvel, B. Reddy, J. Go, C.D. Guevara, E. Salm, M.A. Alam, R. Bashir, Silicon nanowires with high-k hafnium oxide dielectrics for sensitive detection of small nucleic acid oligomers, ACS Nano, 2012, 6 (7), 6150-6164.
38. S. Rigante, High-k dielectric FinFETs on Si-bulk for ionic and biological sensing integrated circuits, 2014, EPFL, Thesis No. 6134
39. I. Yoshitaka, Long-term drift mechanism of Ta2O5 gate pH-ISFETs, Sensors and Actuators B: Chemical, 2000, 64 (1-3), 152-155
40. S. Rollo, D. Rani, W. Olthuis, C. Pascual García, Single step fabrication of silicon resistors on SOI substrate used as thermistors, Scientific Reports, 2019, 9 (1), doi: 10.1038/s41598-019-38753-x.

41. X. Liu, F. Hu, W. Ding, R. Tian, R. Li, H. Li, A how-to approach for estimation of surface/Stern potentials considering ionic size and polarization, Analysts, 2015, 140, 7217-7224.
42. T. Akiyama, Y. Ujihira, Y. Okabe, T. Sugano, E. Niki, Ion-Sensitive Field-Effect Transistors with inorganic gate oxide for pH sensing, IEEE TRANSACTIONS ON ELECTRON DEVICES, 1982, 29 (12), 1936-1941.
43. S. Rigante et al., Sensing with advanced computing technology: Fin Field-Effect Transistors with high-k gate stack on bulk silicon, ACS Nano, 2015, 9 (5), 4872-4881.
44. Šeruga, D. Hasenay, Electrochemical and surface properties of aluminium in citric acid solutions, Journal of Applied Electrochemistry, 2001, 31, 961-967.
45. T-E. Bae, H-J. Jang, J-H. Yang, W-J Cho, High performance of silicon nanowire-based biosensors using a high-k stacked sensing thin film, ACS Applied Materials & Interfaces, 2013, 5, 5214-5218.

Supplementary Information to chapter 4

SI4.1 Calculations of the differential double layer capacitance C_{diff} and intrinsic buffer capacity β_{int} for SiO_2, Al_2O_3 and HfO_2

In our calculations we refer to Van Hal et al.[1] which derive an expression for the differential double layer capacitance combining the Site Binding (SB) and the Gouy-Chapman-Stern (GCS) models which explain the interaction of the oxide surface reactive groups with the ions in the electrolyte and the formation of an electrical double layer into the fluid starting from the oxide surface. C_{diff} is considered as the series capacitance of the Stern capacitance C_{St} (the contribution of the layer of charges in closest contact with the oxide) and the diffuse layer capacitance C_{DL} (from Gouy and Chapman), as shown in eq. 1:

$$\frac{1}{C_{diff}} = \frac{1}{C_{St}} + \frac{1}{C_{DL}} \qquad \text{Eq. SI5.1}$$

C_{St} has been calculated for electrolytes at different ionic strenghts[2]. For our calculations we use the same value considered by Van Hal et al. for describing ISFETs pH response of 0.8 F/m^2. To derive C_{DL} it is assumed that the total charge in the diffuse layer σ_{DL} (the Stern layer by definition does not contain charges) compensate for the charge at the oxide surface σ_0. With this assumption Van Hal et al. report the following expression:

$$\sigma_{DL} = -(8kT\varepsilon_0\varepsilon_w n^0)^{1/2} sinh\left(\frac{zq\Psi_0}{2kT}\right) = -C_{DL}\Psi_0 = -\sigma_0 \qquad \text{Eq. SI5.2}$$

Where k, T and q are the Boltzmann constant, the absolute temperature and the elementary charge respectively. ε_0, ε_w and n^0 are the vacuum permittivity, the relative permittivity of water and the number concentration of each ion of the electrolyte respectively. By combining eq. SI5.1 and SI5.2 it is then possible to calculate C_{diff}.

For the calculations of the intrinsic buffer capacity of the different materials we refer to the same paper[1]. β_{int} depends on the intrinsic characteristics of

the dielectrics, being the acidic and basic dissociation constants of the surface reactive groups (K_a, K_b), and surface density of reactive sites (N_s) and it represents the ability of the surface to buffer small changes of charge. Considering the number of surface groups and their interactions with the protons in the solution it is possible to quantify the intrinsic buffer capacity in terms of groups/unit area. The expression is reported by eq. SI5.3:

$$\beta_{int} = N_s \frac{K_b a_{H+}^2 + 4K_a K_b a_{H+} + K_a K_b^2}{(K_a K_b + K_b a_{H+} + a^2)^2} 2.3 a_{H+} \qquad \text{Eq. SI5.3}$$

Where K_a, K_b and N_s are oxide dependent and a_{H+} is the activity of protons which is linked to the pH through the expression:

$$pH = -\log(a_{H+})$$

In the following table we specify the values reported in literature[2,3] which we used for our calculations of β_{int} for the different oxides.

	pK_a	pK_b	N_s (groups/m^2)
SiO_2	6	-2	$5 \cdot 10^{18}$
Al_2O_3	10	6	$8 \cdot 10^{18}$
HfO_2	7	7	$5 \cdot 10^{18}$

SI4.2 Transfer characteristics of Al_2O_3 Fin-FET after pH measurements in citric acid

We measured the transfer characteristics of the Fin-FET device with Al_2O as sensing layer after the measurements of acidity in the citric juices. The I_{ds} vs V_{ref} curves were acquired in buffers at pH between 3 to 11.5 at a fixed V_{ds}' voltage of 300mV and sweeping the reference electrode voltage between -600mV and 600mV. Figure SI4.1 reports the measured curves. We evaluated the shift of the V_{ref} to keep the current at pH 11 at V_{ref} =0 V constant and we obtained a value of 27 mV/pH which is much lower than the one obtained prior the use in citric juices of 54 mV/pH. We noticed also that a loss of the linearity of the shift of the transfer curves with the pH. We believe that due

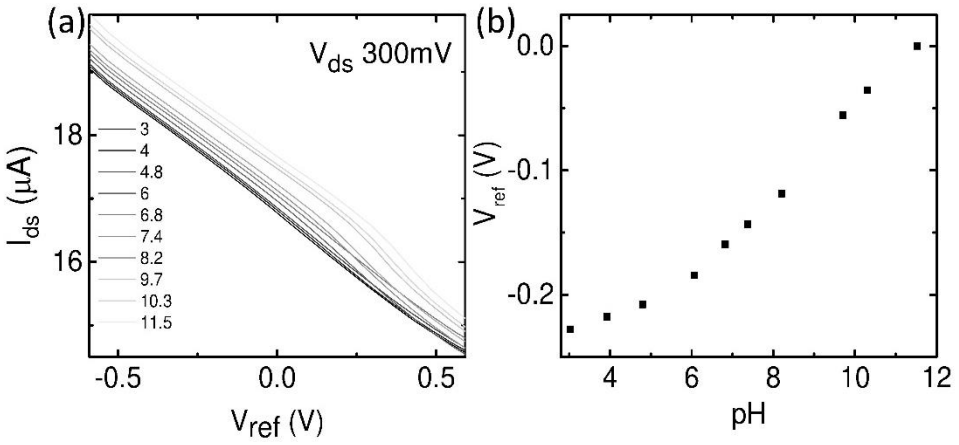

Figure SI4.1 (a) Transfer characteristics at pH between 3 and 11.5 of the Fin-FET with Al_2O_3 as sensitive layer after 4 hours in citric juices. (b) Evaluation of the transfer curves shift as voltage that needs to be applied to the reference voltage to keep a constant current.

to the reported corrosion of aluminium in citric acid, the prolonged exposure of the dielectric to the citric liquids may have completely corroded the Al_2O_3 revealing the SiO_2 oxide layer below, which explains the pH sensitivity and loss of linearity observed after the experiment. We performed EDX spectroscopy on samples processed together with the sensors, with the same Al_2O_3/SiO_2 bilayer, before and after exposure for 24h to the same citric acid solution used during the experiments. The spectra were acquired with a FEI Helios microscope with a beam energy of 5kV and a current of 200pA. We notice that the signal from Al disappears in the sample exposed to citric acid, confirming further our hypothesis of corrosion of the alumina.

References

1. R.E.G. Van Hal, J.C.T. Eijkel, P. Bergveld, A general model to describe the electrostatic at electrolyte oxide interfaces, Adv. Colloid Interfaces Sci., 1996, 68, 31-62
2. X. Liu, F. Hu, W. Ding, R. Tian, R. Li, H. Li, A how-to approach for estimation of surface/Stern potentials considering ionic size and polarization, Analysts, 2015, 140, 7217-7224
3. T. Akiyama, Y. Ujihira, Y. Okabe, T. Sugano, E. Niki, Ion-Sensitive Field-Effect Transistors with Inorganic Gate Oxide for pH Sensing, IEEE TRANSACTIONS ON ELECTRON DEVICES, 1982, 29 (12), 1936-1941

Chapter 5

SINGLE STEP FABRICATION OF SILICON RESISTORS ON SOI SUBSTRATES USED AS THERMISTORS

In this chapter I show an application of the developed fabrication protocol for Fin-FETs on <110> oriented Silicon On Insulator (SOI) substrate. First I present a study of the etching characteristics (etching rates and etching profile) of <110> SOI depending on the mask orientation relative to the wafer primary flat and I use these information to apply the fabrication protocol to fabricate resistors with rectangular and triangular cross section on the same substrate in a single wet etching process. I deploy the differently shaped resistors as temperature sensors (silicon thermistors) and established their accuracy. I comment on the effect of the shape of the resistor on the thermalization with the surrounding environment.

This chapter is based on the publication S. Rollo, D. Rani, W. Olthuis, C.P. García, "Single step fabrication of Silicon resistors on SOI substrates used as Thermistors", *Sci. Rep.*, 9, 2019, article number 2835.

5.1 Abstract

Temperature sensing is one of the important features of Micro Electro Mechanical Systems (MEMS) and a monolithic integration provides advantages for both fabrication simplicity and performance. The use of Silicon On Insulator substrates allows simple fabrication of integrated wires that can be used as thermistors. We fabricated rectangular and triangular silicon wires with different dimensions in a single step fabrication process based on the wet etching of a <110> Silicon On Insulator substrate. We determined the experimental resistivity of the two kinds of devices and tested their performance as thermistors in a temperature range between 24 and 100°C. The accuracy and normalized sensitivities of our devices were 0.4°C and 0.3-0.5%/°C, respectively. The potential of the proposed method resides in the possibility of having devices with different shapes in a single step process and therefore a single fabrication line.

5.2 Introduction

Online and real-time measurements of temperature are fundamental for many applications in different domains ranging from bio-sensing, environment, electronics, etc.[1-2]. In this context the drive for miniaturisation demands possibilities to integrate thermometers together with other electronic components. The most often used options include thermocouples[3,4] and resistive thermometers (thermistors)[5-6], the later ones offering robust and cost-effective manufacturing with a considerably good stability and accuracy (reaching <0.01°C for metallic thermistors). Silicon thermistors, although they are not as sensitive as the metallic, can be attractive because they can be integrated into electronic circuits like Complementary Metal Oxide Semiconductor (CMOS) circuits, MEMS, and Lab-on-a-Chip (LoC) devices taking advantages of the well-established silicon fabrication techniques. Furthermore, the monolithic

integration of electronics and sensors with an optimised design that improves the surface area in contact with the object to measure is a way to improve the thermalization and the performance of the thermometers.

Since the implementation of fin field effect transistors (FinFETs) for high speed electronics[7,8] and the development of new MEMS[9,10,11], Silicon on Insulator (SOI) substrates based technologies are replacing conventional silicon substrates ones for the most demanding applications. In the last three years the global SOI market has doubled due to the advantages related to the buried oxide (commonly SiO_2) underneath the top silicon device layer, which reduces parasitic capacitances and leakage currents due to the different electrical and thermal conductivities of Si and SiO_2 (twelve and two orders of magnitude respectively larger in silicon). The difference in the thermal conductivity also opens the door to new architectures in which the temperature sensor can thermalize with other device components (like liquids in microfluidic devices, or a thermally conductive coating) or the own operating circuit, and not mainly with the substrate as traditional thermometers.

Tailoring the shape of a thermometer with anisotropic etching can be appealing in order to have the flexibility to optimize the surface area in contact with the object to measure. Anisotropic etching can be accomplished by either dry or wet processes[12,13], both requiring a mask with high selectivity relative to the substrate. Dry processes are used for anisotropic etching of high aspect-ratio structures. However, they are known to induce unwanted defects and roughness coming from the ion bombardment. On the other hand, wet etching of Si can provide both anisotropic and isotropic structures, even in the same process, due to the dependency of the etching rates on the crystallographic orientation of the planes exposed to the solution[14,15,16]. Wet etching also provides smoother surfaces and less defects. Producing different

structures within a single process can also increase the efficiency and reliability of the fabrication, reducing variability between devices. <100> oriented substrates are commonly used for the fabrication of triangular structures by wet etching[17,18]. Fabrication of rectangular structures can be achieved on the same substrates by dry etching[19]. Structures with other shapes can also be obtained by subsequent steps of oxidation and etching of the grown oxide[18]. However wet etching of <110> avoids some of the damaging introduced by dry etching, and can create simultaneously different shapes within the same process.

In this work we present a single step fabrication process of silicon resistors with different shapes on a SOI chip, following the study of the etching rates of tetramethylammonium hydroxide (TMAH) solutions on different crystallographic directions on the <110> silicon device layer, to produce both triangular and rectangular devices. We tested them as silicon thermistors and extrapolated the first order thermal coefficient. Additionally we calculated the accuracy of our devices (~0.4°C) and the normalized sensitivity (~0.3-0.5%/°C), which is comparatively better than the one of commercially available silicon thermistors[20,29]. The proposed method offers customization possibilities to produce devices with different geometries and contact areas to monitor better the temperature dependent process of interest.

5.3 Materials and methods

We used a 3 inches prime quality p-doped SOI substrate from Ultrasil Corporation, with a 2 ± 0.5 µm thick silicon device layer <110> oriented, and a 1 µm thick buried SiO_2, both for the optimisation of the etching process producing different shapes, and for the final fabrication of the silicon thermistors.

5.3.1 Sample patterning

The as bought substrate was sent for dicing into 1cmx1cm chips to Siegert Wafer. After dicing we cleaned a chip with solvents (acetone, isopropanol and deionized water). Then a 50 nm film of SiO_2 was grown as masking material by thermal oxidation of the silicon top layer at 1000°C and atmospheric pressure, with a 200 sccm flow of oxygen during 190 seconds. We used a FEI Helios electron microscope with the electron beam energy of 30 keV to expose specific designs on a negative resist ma-N2043 spun at 2000 rpm. The samples were developed for 1 minute in ma-D developer with manual stirring. The resulting resist patterns were then transferred into the underlying SiO_2 by Reactive Ion Etching (RIE) using CF_4 plasma (19 sccm) with a power of 25W and a pressure of 75mTorr.

To eliminate the irregularities produced during RIE we carried out the etching until few nm of SiO_2 were left outside the patterns. Thereafter we removed the resist mask by keeping the sample into remover PG for 10 minutes and rinsing it well with isopropanol and deionized water. After that we removed the leftover SiO_2 using HF (2%) treatment for 1 minute which left a flat clean surface of Si. Before the HF treatment of the leftover SiO_2 we removed the resist mask keeping the sample in remover PG for 10 minutes and rinsing it with isopropanol and deionized water.

5.3.2 TMAH wet etching

A wt.25 % TMAH solution, with addition of vol.8.5 % of isopropanol (IPA) was used as etchant. We heated the solution to 43 ± 1°C and performed the etching under stirring at 250 rpm. The process was carried out in a borosilicate beaker with 35 ml of etching solution placed on top of the stirrer-hot plate. The temperature was controlled by an external thermometer immersed in the etching solution.

5.3.3 Calibration of the <110> silicon wet etching rates

In order to have information about the etched profiles and rates on the SOI <110> we made a pattern consisting of a set of crosses in which the arms of

the crosses rotated by 0.5° closer in each step. The dimensions of the crosses arms were 0.8 x 18 μm^2. In each cross we obtained the information from four angles with respect to the primary flat (see SI5.1). For the calibration of the etching rates in the selected orientations resulting in rectangular and triangular walls we prepared samples with patterned rectangles 40 µm long and widths ranging from 500 nm to 3 µm, in steps of 500 nm, which were etched at different etching times with intervals of 2 minutes up to the complete etching of the device layer. The obtained information was finally used to prepare the sample with the rectangular and triangular resistors to be applied as temperature sensors.

5.3.4 Ohmic contacts

In order to measure the resistors by an external measurement set-up we needed to fabricate ohmic contacts. These were patterned by a Maskless Laser Aligner (MLA150) set-up (Heidelberg Instrument) with a wavelength of 365 nm exposing on a double layer resist consisting of LOR10A and Shipley1813 spun at 1000 and 2000 rpm for 30 and 60 seconds respectively, to obtain a thickness of ≈ 4 µm for the complete coverage of the 2 µm high patterned silicon structures. Then a stack of Ti(5nm)/Al(160nm)/Au(50nm) was deposited by electron beam evaporation under high vacuum ($<10^{-7}$ mTorr). The annealing was carried out under vacuum at 400°C for 5 minutes in a reductive atmosphere made by N_2/H_2 (5%). Then, wider metallic leads for electrical characterization were defined by a second MLA process. For these, we first evaporated a layer of 5 nm of Ti and 50 nm of Au by electron beam evaporation, followed by 50 nm of Au deposited by conformal sputtering, to assure electrical continuity between the leads and the ohmic contacts.

5.3.5 Electrical and Thermal characterization

Electrical transport experiments were carried out using a Keithley 2614HB DC source-meter. Current-Voltage (I-V) curves were acquired for multiple devices with different shapes and dimensions using two wire

characterisation. The thermal characterization of the sample was made on the CascadeMicrotech PM8 probe station with a heated sample holder. The temperature was set to the desired value from the controller of the heating stage. We monitored the temperature of the substrate using a type K thermocouple from DOSTMANN electronic GmbH fixed on a silicon chip close to the sample using Kapton® tape. The I-V curves were recorded only after the stabilisation of the temperature as measured from the probe.

5.4 Results and discussion

5.4.1 Design and fabrication of differently shaped wires within a single process

The anisotropic etching of Si is well understood[20,21,22,23] but a recipe to obtain different shapes in a single step process requires the calibration of the simultaneous etching rates depending on the plane orientation. We analysed the different profiles obtained by different pattern orientations from the etched crosses described in section 5.3.3. Figures 5.1 (a) to (d) show representative scanning electron microscope (SEM) pictures of crosses ((a) and (b) are the top view and (c) and (d) are tilted images). The initial SiO_2 mask is shadowed in blue, while the etched profile is shadowed in green. The directions parallel (<112>) and at 55 ± 2° (<110>) with respect to the primary flat resulted in perpendicular and 36° tilted walls (<111>) with respect to the substrate, respectively. They also showed smoother etched surfaces compared to the other orientations. These results are consistent with the ones reported in literature[24,25]. In fig. 5.1 (e) we schematically represent the high symmetry etching planes and their resulting etching profiles depending on the alignment of the mask on the top silicon device layer. As expected from TMAH wet etching studies of Si, the plane along the <110> direction was etched faster, while the planes along the <111> direction were almost unaffected[21].

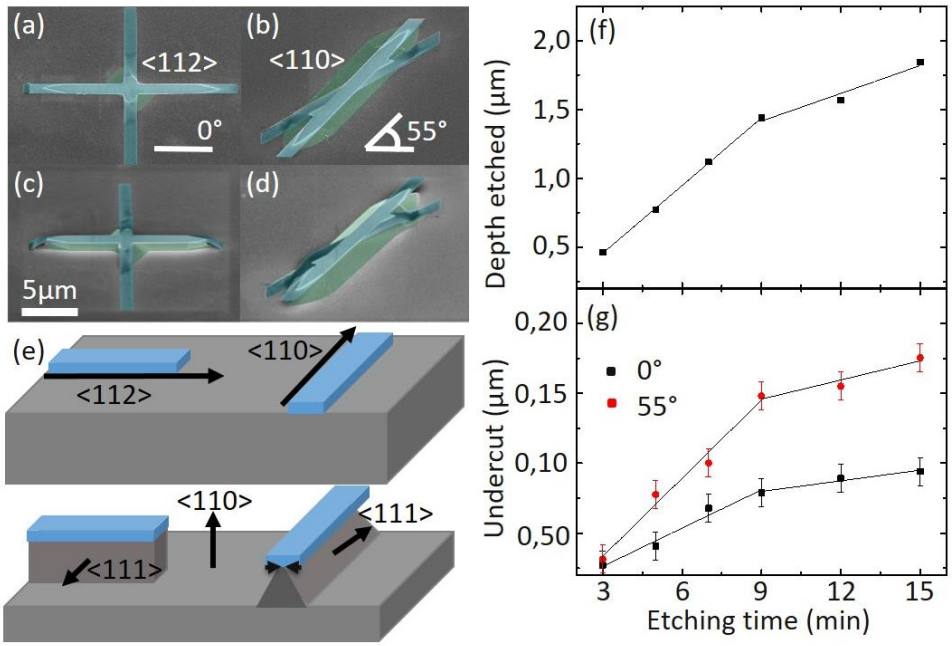

Figure 5.1 Top view ((a) and (b)) and tilted ((c) and (d)) scanning electron microscope pictures of the crosses with arms aligned in the two directions giving rectangular and triangular etched profiles. The SiO_2 mask is shadowed in blue. (e) Schematic of etching masks aligned in the chosen crystallographic directions and resulting etching profiles. (f) Depth etched in the direction perpendicular to the substrate and (g) undercut observed for the directions parallel to the primary flat and 55° that resulted in rectangular and triangular wires, respectively.

Using samples specifically designed with the two selected orientations we measured the etching rates and undercut with a KLA Tencor P-17 profilometer and SEM, respectively. Figure 5.1 (f) and (g) show the results of six samples etched at different times with intervals of 2 minutes. Initially the vertical etching rate was 163.9 nm/min, and the undercut 9.1 nm/min and 18.1 nm/min for the <112> and <110> orientations respectively. After nine minutes these values decreased to 67.3 nm/min, 2.5 nm/min and 4.6 nm/min, respectively. We attribute the slowdown of the rates to the saturation of the etching solution, as in other experiments we recovered the initial rate by refreshing the etchant. As the changes in the etching rates were proportional in all directions the final shapes and roughness were unaffected.

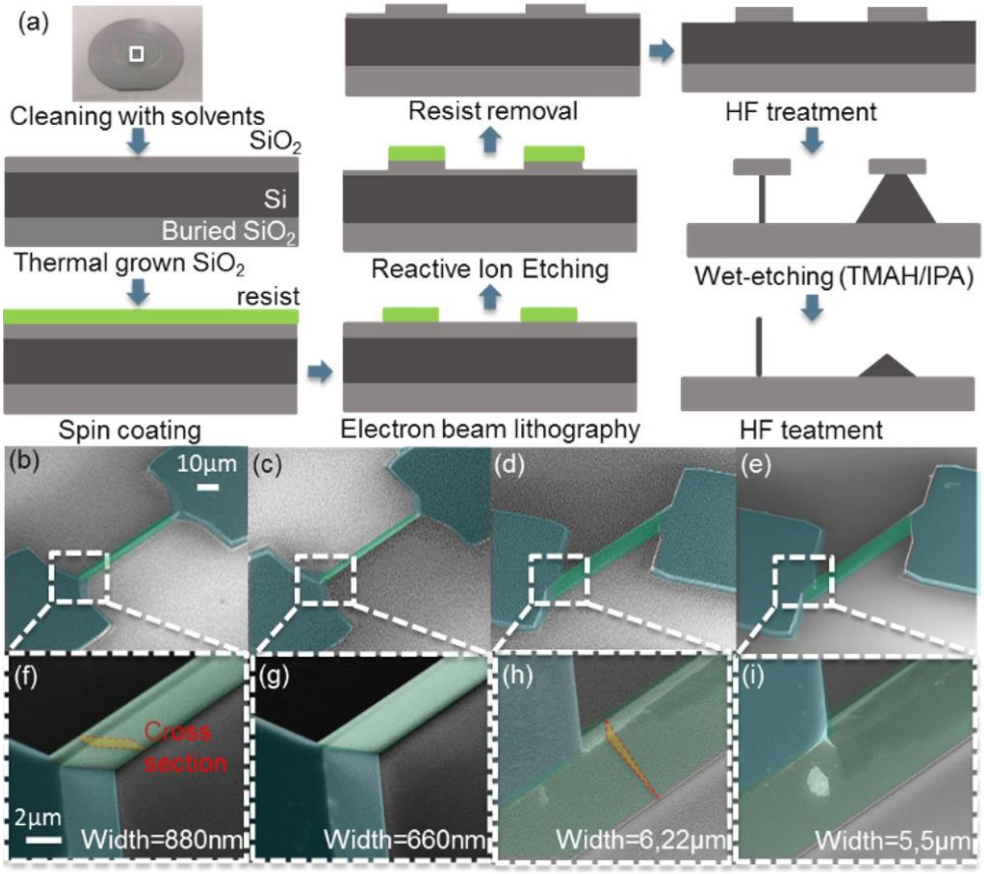

Figure 5.2 (a) Schematic representation of the fabrication protocol for the realization of rectangular and triangular wires. (b) to (e) Top view SEM pictures of representative rectangular and triangular wires ((b), (c) and (d), (e), respectively). (f) to (i) magnifications showing the detailed shape of the wires in (b) to (e). The wires and the contacts have been shadowed in the SEM pictures in green and blue respectively. The cross section in perspective has been indicated in figures (f) and (h). The scale bars are common in both rows.

Therefore, we used the same solution throughout the whole etching process for the fabrication of the *Si* resistors.

Si resistors with different shapes were obtained in a single step process combining different orientations of the mask and following the protocol schematized in fig. 5.2 (a). Briefly, we cleaned the sample with solvents (acetone, isopropanol and deionized water) before the growth of the SiO_2 layer used as mask. We spin coated ma-N negative resist and patterned the

wires with electron beam lithography. The patterned designs were transferred into the SiO_2 by RIE leaving a thin layer of SiO_2 outside the pattern areas. We removed the leftover resist with solvents. After that, we performed a 1 minute HF treatment to remove the remaining SiO_2 outside the pattern areas and open a flat surface on the Si to be etched. Then we proceeded with TMAH wet etching. At the end, we performed a HF treatment to fully remove the leftover SiO_2.

To simplify the electrical characterisation we chose the dimensions of the wire that would produce a resistance orders of magnitude bigger than the typical one from contacts (tens of kΩ versus few hundreds of Ω). We fixed the length of the wire to 60 µm and we added square contact pads of 60 x 60 μm^2. Based on resistivity provided by the fabricant (0.12 Ω·cm) we estimated that we needed widths after etching in the range of few hundreds nm and a few µm for the rectangular and triangular structures respectively to obtain the desired resistance. To achieve these dimensions we needed 23 minutes of etching time to ensure a complete etching of the top silicon layer in the vertical direction resulting in undercuts of 240 nm and 460 nm for the <112> (rectangular wires) and <110> (triangular wires) orientations, respectively. We lithographed masks with widths from 800 nm to 1.1 µm, and 200 nm to 400 nm in steps of 100 nm, aligned in the two chosen directions and connected to two squared contact pads. Small approaching pads connecting the silicon wires and the pads were designed with a triangular footprint with angles of ≈54.7° and ≈35.3° with respect to the primary flat to maintain smooth slanted walls between the channel and the walls coming from the etching of the pads. At the end of the process we obtained silicon wires with widths between 660 and 880 nm, and 5.5 and 6.2 µm for the rectangular and triangular structures respectively.

Figure 5.2 (b) to (i) are representative SEM images corresponding to the bigger and smaller devices for both the rectangular and the triangular wires. Figures 5.2 (b) to (e) show the top view of whole devices with the contact pads and wires shadowed in blue and green, respectively. Figures 5.2 (f) to (i)

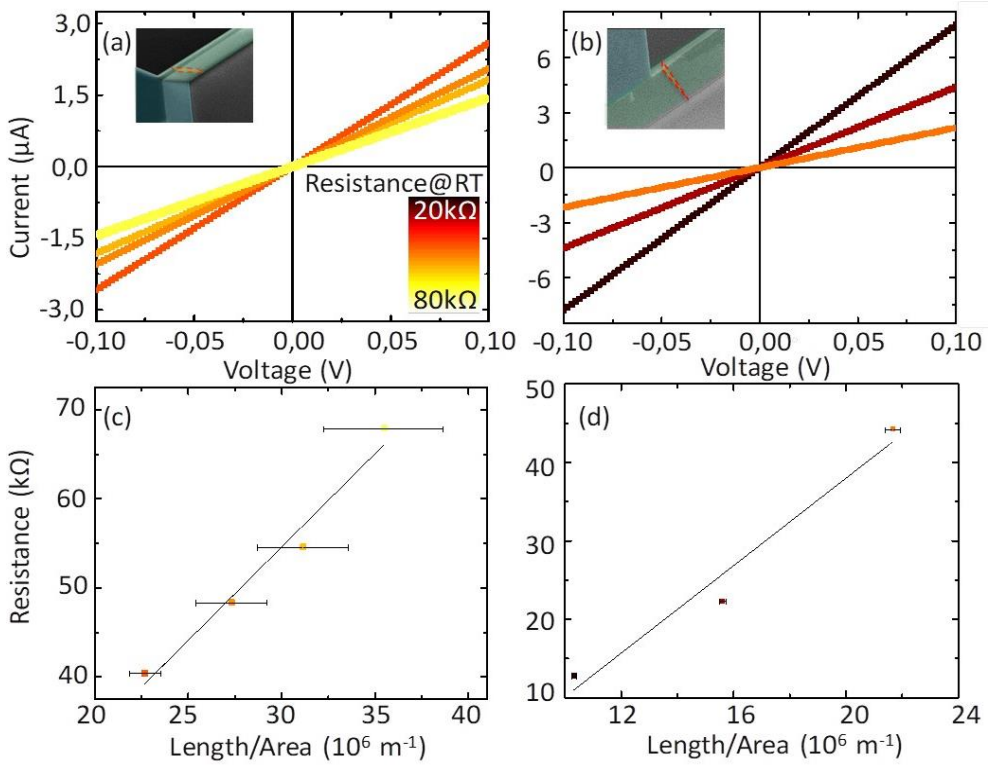

Figure 5.3 (a) and (b) Two probes current versus voltage (IV) curves of the rectangular and triangular wires, respectively. Each curve has a different colour according to the resistance scale in (a). (c) and (d) Plot of the resistances calculated from the curves in (a) and (b) versus the dimensional parameter length divided by area of the wires, for rectangular and triangular structures respectively. Error bars represent the propagation of the experimental uncertainty of the dimensions (length, area). The fitting lines y=ax+b for the derivation of the resistivity of the wires are also shown.

show zoomed in regions close to the contacts and the cross section for the bigger wires of each class. It can be noticed that after the wet etching the rectangular wires have the same height as of the contacts (see in fig. 5.2 (f) and (g)), while that of the triangular wires decreased. This makes that for similar footprint rectangular and triangular wires would have very different cross sections, and consequently different total resistance.

5.4.2 Transport and temperature dependent performance of the silicon wires

Figures 5.3 (a) and (b) show the two probes current versus voltage (I-V) curves of the rectangular and triangular wires, respectively. The I-V curves are linear crossing the zero of both axis, reflecting a good ohmic behaviour. We have identified each with a colour associated to the room temperature (RT) resistance using the scale in fig. 5.3 (a), which is also linked to their dimensions. The different aspect ratio between the wires provided a large variety of cross sections consequently having different resistance, yet the smallest triangular wire could be used in comparison with the two rectangular wires with middle resistances. The total measured resistances were in the range of 39.7 to 66.9 and 12.8 to 44.2 kΩ for the rectangular and triangular wires, respectively. In figs. 5.3 (c) and (d) we plotted the value of these resistances versus a dimensional parameter length divided by area for rectangular and triangular structures respectively. The errors come mainly from the propagation of the experimental uncertainty of the dimensions on the resistance. We obtained higher error values for the rectangular wires with high aspect ratio due to their small widths. From the slope in figs. 5.3 (c) and (d) the experimental resistivity were 0.19 ± 0.04 Ω·cm and 0.25 ± 0.01 Ω·cm for the rectangular and triangular structures, respectively. These values are slightly higher than expected according to the dimensions of the wires and the fabricant resistivity. We attribute the small difference with respect to the value of the provider to the impact of the fabrication defects at the surface. We noticed that the resistivity of the triangular wires was higher, which is consistent with a higher roughness in the slanted etched planes observed in SEM images (see representative images in SI at the end of the chapter).

Temperature measuring is a possible application of any resistor. To study the performance of our wires we recorded the I-V behaviour at different temperatures between 24°C and 100°C and extracted the resistance (see raw data in SI at the end of the chapter) reported in fig. 5.4 (a) and (b) for the square and triangular wires, respectively. The wires are identified with the

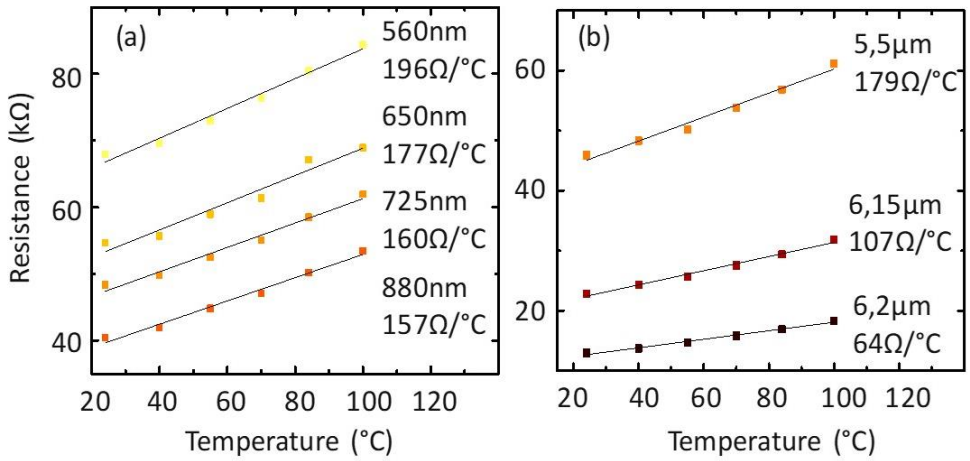

Figure 5.4 (a) and (b) Plot of the resistance versus temperature for the rectangular and the triangular wires respectively. The linear fitting was used to estimate the first order thermal coefficient of our devices. Each line corresponds to a specific device with the base width specified along with the first order thermal coefficient.

colour associated to their RT resistance according to the colour map introduced in fig. 5.3. We observed a linear behaviour in all the cases and therefore we used the slope to extract the first order temperature coefficient (*k*) with a linear fitting obtaining values between 64 and 196 Ω/°C as indicated in fig. 5.4. The first order thermal coefficient (*k*) decreases with increasing dimensions of the wires, and is linked to the original resistance of the wires. The accuracy of the wires as thermometers was calculated based on the uncertainty in *k* from the fit in fig. 5.4 and was found to be ±0,4°C for both the rectangular and triangular wires. The main contribution to *k* is attributed to the variation of the resistivity and in particular to the change in the mean free path. We observed this as the change in resistivity was consistent with data in literature[26] and as the thermal expansion coefficient of silicon is $2.6 \times 10^{-6} °C^{-1}$, and its effect was estimated to contribute in 1 ppm to the variation of the resistance in the considered temperature range (see details in supporting information). We also estimated the normalized temperature sensitivity of our devices, which represents how much the resistance varies in percentage for one degree variation of temperature. This was accomplished by dividing the obtained first order thermal coefficient by the

RT resistance. Results are shown in table 5.1, and are comparable, even better regarding triangular thermistors, than commercially available devices[27,29].

We presume that due to the different ratio of surface area exposed to the substrate or to the surrounding, these devices can be optimised to have better thermal coupling efficiency with the substrate, the electronic circuit or with the outside. High aspect ratio rectangular thermistors devices could be better applied for tracking the temperature of the surrounding medium while triangular cross section ones would better thermalize with the connected circuits or the substrate.

Table 5.1 Normalized temperature sensitivity for our rectangular and triangular cross section silicon thermistors.

Rectangular wires		Triangular wires	
k (Ω/°C)	*ΔR/R(%/°C)*	*k(Ω/°C)*	*ΔR/R (%/°C)*
157	0.39	64	0.5
160	0.3	107	0.48
177	0.37	179	0.4
196	0.29		

5.5 Conclusions

We presented a single process for the simultaneous fabrication of rectangular and triangular silicon structures on a <110> SOI substrate and we tested their performance as silicon thermistors. The devices show a linear IV characteristics, with room temperature resistances in the range of a few kilo ohms. Their behaviour as resistors was well predicted from the bulk conductivity and the apparent dimensions of the devices. Results of measured resistivity showed that the process introduced some defects. In particular, triangular devices showed higher resistivity, which can be a result of higher roughness observed in the surface. Surface roughness could be further improved for a better performance of the device with the

optimisation of the etching solution for example, by the use of surfactants[28]. The resistance of the devices varied linearly with temperature in the explored range (RT to 100°C), with a first order thermal coefficient *k* between 63 and 196 Ω/°C, obtaining a change of the resistivity of 13.5% in the temperature range investigated. The higher resistances corresponded to higher values of *k* and for similar room temperature resistance the first order temperature coefficient did not depended on the shape of the wire. We estimated the accuracy of the fabricated silicon thermistors as 0,4°C, and the normalized temperature sensitivity for each device which were found to be in accordance or even better than normally expected for silicon based temperature sensors[27,29].

In summary, in this study we have shown a method that procides the possibility of fabricating devices with different shapes in a single step process. Therefore in a single fabrication line it is possible to engineer shapes, that could be used to either follow the change of the temperature of the substrate or of the surrounding medium, allowing multiple control over the integrated system.

References

1. Childs, P. R. N., Greenwood, J. R. & Long, C. A. Review of temperature measurement. Review of Scientific Instruments 71 (2000)
2. Liu, Y. & Dickt, R. P. Accurate Temperature-Dependent Integrated Circuit Leakage Power Estimation is Easy. IEEE Design, Automation and test in Europe Conference and Exhibition 1-3 (2007)
3. Kreider, K. G., Ripple, D. C. & Kimes, W. A. THIN-FILM RESISTANCE THERMOMETERS ON SILICON WAFERS. Meas. Sci. Technol. 20, 1–18 (2009)
4. Rosner, D. E. Soot Volume Fraction and Temperature Measurements in Laminar Nonpremixed Flames Using Thermocouples. Combustion and Flame 109, 701–720 (1997)
5. Butorac, J. & Ferkovic, L. Temperature measurements by means of NTC resistors and a two-parameter approximation curve. Measurement 41, 294–299 (2008)
6. Valvano, J. W., Cochran, J. R. & Diller, K. R. Thermal Conductivity and Diffusivity of Biomaterials Measured with Self-Heated Thermistors. International Journal of Thermophysics 6, 301-311 (1985)
7. Fossum, J. G., Zhou, Z., Mathew, L. & Nguyen, B. Solid-State Electronics SOI versus bulk-silicon nanoscale FinFETs. Solid State Electron. 54, 86–89 (2010)
8. Rigante, S. et al. High-k dielectric FinFETs towards Sensing Integrated Circuits. IEEE International Conference on ultimate integration on silicon, 73–76 (2013)
9. Shen, D. et al. Physical Micromachined PZT cantilever based on SOI structure for low frequency vibration energy harvesting. Sensors and Actuators A 154, 103–108 (2009)
10. Su, S. X. P., Yang, H. S. and Agogino, A. M. A resonant accelerometer with two-stage Microleverage Mechanisms Fabricated by SOI-MEMS Technology. IEEE Sensors Journal, 1-9 (2005)
11. Judy, J. W. Microelectromechanical systems (MEMS): fabrication ,

design and applications. Smart Materials and Structures 10, 1115-1134 (2014)
12. Prakash, A., Jency, J. G. & Mathew, M. C. A Review of various Wet Etching Techniques used in Micro Fabrication for Real Estate Consumption. Int. J. Comput. Appl. 975–8887 (2013)
13. Jansen, H., Gardeniers, H. & Boer, M. A survey on the reactive ion etching of silicon in microtechnology. J. Micromech. Microeng. 6, 14–28 (1996)
14. Seidel, H., Csepregi, L., Heusberger, A. & Baumgärtel, H. Anisotropic Etching of Crystalline Silicon in Alkaline Solutions: II. Influence of Dopants. J. Electrochem. Soc. 137, 3626–3632 (1990)
15. Theil, J. A. Deep trench fabrication by Si (110) orientation dependent etching. J. Vac. Sci. Technol. B Microelectron. Nanom. Struct. 13, 2145-2147 (1995)
16. Sato, K. et al. Characterization of orientation-dependent etching properties of single-crystal silicon: Effects of KOH concentration. Sensors Actuators A Phys. 64, 87–93 (1998)
17. Li, M., Chen, G. & Huang, R. High Performance GAA SNWT with a Triangular Cross Section : Simulation and Experiments. Appl. Sci. 8, 1553-(2018)
18. Pennelli, G., Piotto, M. Fabrication and characterization of silicon nanowires with triangular cross section. Journal of Applied Physics 100, 54507(2014)
19. Fatimah, S., Rahman, A., Yusof, N. A., Hashim, U. & Nor, M. N. Design and Fabrication of Silicon Nanowire based Sensor. Int. J. Electrochem. Sci. 8, 10946–10960 (2013)
20. Chen, P. H., Peng, H. Y., Hsieh, C. M. & Chyu, M. K. The characteristic behavior of TMAH water solution for anisotropic etching on both silicon substrate and SiO2 layer. Sens. Actuators A 93, 132–137 (2001)
21. Tokoro, K., Uchikawa, D., Shikida, M. & Sato, K. Anisotropic etching properties of silicon in KOH and TMAH solutions. IEEE Int. Symp. Micromechatronics Hum. Sci. 65–70 (1998)

22. Merlos, A., Acero, M., Bao, M. H., Bausells, J. & Esteve, J. TMAH/IPA anisotropic etching characteristics. Sensors and Actuators A Phys. 37–38, 737–743 (1993)
23. Brockmeier, A., Rodriguez, F. J. S., Harrison, M. & Hilleringmann, U. Surface tension and its role for vertical wet etching of silicon. J. Micromechanics Microengineering 22 (2012)
24. James, T. D., Parish, G., Winchester, K. J. & Musca, C. A. A crystallographic alignment method in silicon for deep, long microchannel fabrication. J. Micromechanics Microengineering 16, 2177–2182 (2006)
25. Debnath, K., Arimoto, H., Husain, M. K. & Prasmusinto, A. Low-Loss Silicon Waveguides and Grating Couplers Fabricated Using Anisotropic Wet Etching Technique. Frontiers in Materials 3, 1–7 (2016)
26. Morin, F. J. & Maita, J. P. Electrical Properties of Silicon Containing Arsenic and Boron. Physical Review 96, 28-35 (1954)
27. https://www.ephy-mess.de/en/products-and-solutions/product-overview/semiconductors-and-thermistors/
28. Cheng, D., Gosalvez, M. A., Hori, T., Sato, K. & Shikida, M. Improvement in smoothness of anisotropically etched silicon surfaces : Effects of surfactant and TMAH concentrations. Sensors and Actuators 125, 415–421 (2006)
29. O Shea, P. Silicon thermistors provide more accurate temperature sensing, optimizing system performance. EETimes Connecting the global electronic community. https://www.eetimes.com/document.asap?doc_id=1291878

Supplementary Information to chapter 5

SI5.1 Study of the etching profile on 110 silicon on insulator

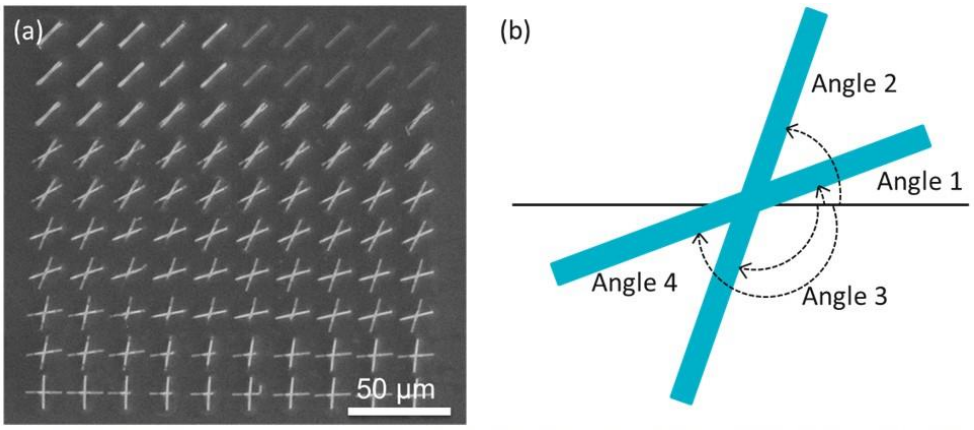

Figure SI5.1 (a) Pattern with crosses with arms oriented along all the 360° angles for the preliminary study of the etching profile on <110> SOI substrate. (b) Schematic representing a cross and the four angles about which it is possible to get information after etching.

In fig. SI5.1 (a) the crosses which have been patterned on the substrate for the study of the etching profiles as explained in section 5.3.3 are shown. Figure SI5.1 (b) is a schematic of a cross and the four angles about which it is possible to obtain information after etching. This applies for each cross. Figure SI5.2 (a) and (b) are high contrast SEM pictures of the etched walls with perpendicular and tilted angles respect to the substrate, respectively from a representative sample. Figure SI5.2 (c) shows the two etched planes

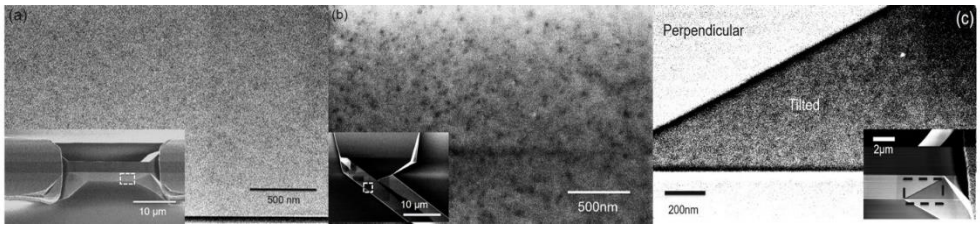

Figure SI5.2 (a) and (b) are high contrast SEM pictures of the etched walls with perpendicular and tilted angles respect to the substrate, respectively from a representative sample. Figure 2 (c) shows the two etched planes from one of the devices with vertical walls, at the junction. The pictures show the apparent higher roughness is observed for tilted walled as compared for perpendicular walls.

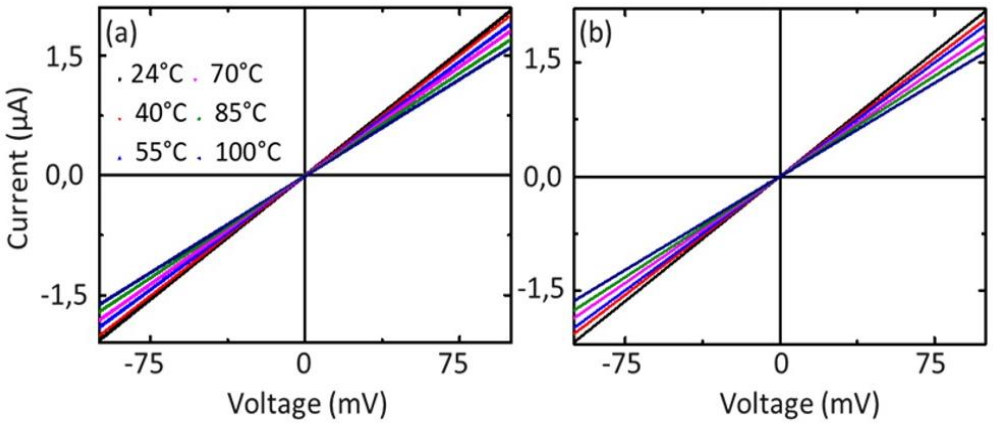

Figure SI5.3 (a) and (b) Temperature dependent I-V curves for a rectangular and triangular resistor respectively.

from one of the devices with vertical walls, at the junction. The pictures show the apparent higher roughness observed for tilted walls as compared with perpendicular walls.

SI5.2 Temperature dependent IV characteristics

In figs. SI5.3 (a) and (b) representative temperature dependent I-V curves for one rectangular and triangular resistors respectively are shown. These curves were used for the extrapolation of the resistance of the devices at each temperature through a linear fitting.

SI5.3 Calculations of the accuracy

To have information about the accuracy of our devices we considered the dependency of the temperature on the change of the resistance (ΔR) and the first order thermal coefficient (k) as shown in eq. SI5.1. When we determined these two parameters experimentally from linear fitting of the experimental data, they both were accompanied by an error. Taking this into account, we used the error propagation formula according to which the error on a quantity which depends on other quantities can be estimated from the square root of the sum of the fractional uncertainties on these latest ones. Therefore we applied eq. SI5.2 to calculate the accuracy (δT). Here, T_{RT} is the

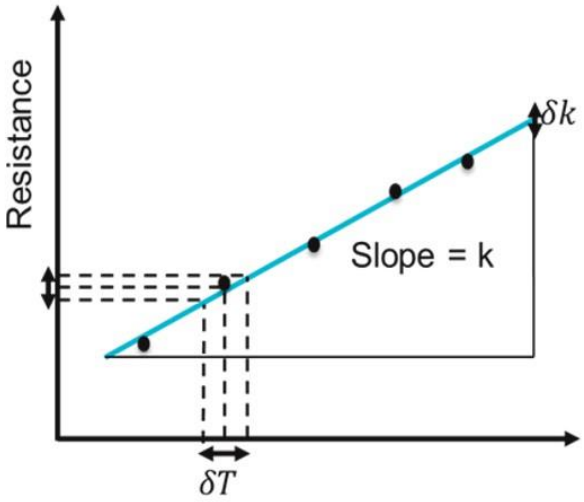

Figure SI5.4 Schematic representation of the meaning of accuracy and its calculation.

room temperature, and δk and δR are the errors on the first order temperature coefficient and on the resistance respectively.

$$\Delta T = \frac{\Delta R}{k} \qquad \text{Eq. SI5.1}$$

$$\delta T = T_{RT} \cdot \sqrt{\left(\frac{\delta R}{R}\right)^2 + \left(\frac{\delta k}{k}\right)^2} \qquad \text{Eq. SI5.2}$$

Figure SI5.4 is a schematic of the significance of accuracy and its calculation.

SI5.4 Comparison of the conductivity with literature data

As stated in the chapter the variation of the resistivity (therefore conductivity) of our devices with temperature was in agreement with literature data. We repeated the procedure explained in 5.4.2 to calculate the resistivity at each temperature and we calculated the conductivity as the inverse of the resistivity. Figure SI5.5 shows the plot of the conductivity with temperature for a representative device with rectangular cross section. These results were compared with literature[1] and they were found to be in agreement within the 15%.

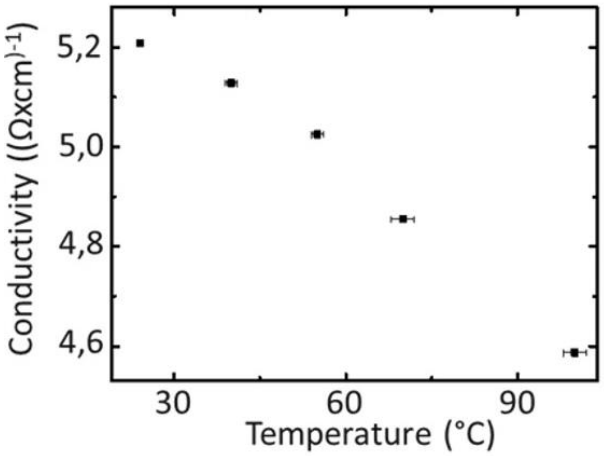

Figure SI5.5 Plot of the calculated conductivity vs temperature for a representative rectangular silicon thermistor (rectangular cross section and width of 880 nm).

References

1. Morin, F. J. and Maita, J. P. Electrical Properties of Silicon Containing Arsenic and Boron. Physical Review 96, 28-35 (1954)

Chapter 6

CONCLUSIONS AND OUTLOOK

6.1 Conclusions

This thesis describes the work done on the project NANOpH financed by the Luxembourg National Research Fund. It includes the development of a new sensor design based on silicon and a fabrication protocol resulting in reproducible devices using cleanroom facilities, the study of a transduction model, and the application of the fabricated devices as pH sensors deploying different dielectric materials.

The novel design was developed taking into account the challenges related to sensing such as reliability of the response among devices and thus to fabrication and functionalization, signal to noise, dynamic range, limit of detection and time for the assay. A fin configuration of a sensor with high aspect ratio of the height/width dimensions (>10) was identified as a good compromise for addressing these issues while keeping a good sensitivity. Fin-FETs with a width from 100 to 400 nm and a height of 2 or 3 µm were fabricated in a reproducible way on p-doped SOI wafers <110> oriented using a top-down approach based on conventional microfabrication techniques with cleanroom facilities. The fabrication followed a theoretical study of the transduction of the charge of the analytes at the dielectric surface into the semiconductor through a capacitive effect, based on the Nernst and the Poisson models. A relation between the conductance of the sensor channel and the thickness, dielectric constant and surface reactivity of the dielectric layer and doping of the semiconductor has been established. We approached the study of the sensors by testing them as pH sensors. We observed a decrease of the output current by moving towards more acidic pH due to the repulsive force experienced by the positively charged carriers provided by the more abundant protons at lower pH. As a result the conductance through the

channel increases with increasing pH and vice versa. The Fin-FETs were theoretically and experimentally compared with data reported in literature on Si-NWs pH sensors. Advantages of improved signal to noise ratio and linearity of the variation of the conductance with proton concentration in the same pH range were identified. The response time for sensing different proton concentrations until steady state signal was investigated, along with calculations for the detection time of DNA and proteins which were compared with the same calculations performed for planar Bio-FET and nanowires. The results suggested that at low concentrations the Fin-FETs could approach the time response of nanowires. Thermal grown SiO_2, and ALD deposited Al_2O_3 and HfO_2 were investigated as pH sensitive layers and they were compared in terms of surface sensitivity to protons, chemical stability in acidic conditions and their influence on the transconductance of the sensors. The differences in the response of the oxides was attributed to the different reactivity of the surface reactive groups with protons and the different number of surface reactive sites. The superior effect of the high-k dielectric HfO_2 on the transconductance has been demonstrated.

We explored the devices as temperature sensors by applying the study for the development of the fabrication protocol for the Fin-FETs to the fabrication of resistors with rectangular and triangular cross sections with widths from few hundred nanometers to few micrometers in a single wet etching process, which were investigated as temperature sensors (silicon thermistors) between 25° and 100°C. In this temperature range the resistance of the sensors varied linearly and an accuracy of 0.4°C has been estimated. Triangular structures showed higher values of the relative variation of the resistance compared to rectangular ones. We attributed this to the different shape of the sensors. The two geometries share a different surface area with the environment, and the circuit and substrate. Having a higher surface in contact with the substrate and circuit triangular resistors are more suitable to follow the substrate and circuit temperature, while the rectangular sensors would better thermalize with the surrounding.

In conclusion, we approached the problems of (bio)sensing from a sensor design point of view developing a novel configuration of device, and we

believe that the Fin-FETs represent an improvement to the state of art of Bio-FETs with promises of reliability to fabrication and functionalization with bioreceptors, good signal to noise ratio, improved linearity in the output response, wider dynamic range and efficiency at capturing slow diffusive molecules for the 2D configuration.

Further research is being carried out with the goal of integrating Fin-FETs chips within microfluidic devices, and their functionalization with bioreceptors to allow the detection of biomolecules in a multiplexed way. We expect to have data of limits of detections and time for the assays of Fin-FETs based biosensors in the next future.

6.2 Outlook on Biosensors Market

Throughout this dissertation I often referred to biosensors and their applications. As an overview of the relevance of the topic and its impact in the near future I report in fig. 6.1 the study from Global Market Insights, Inc. regarding the size of the global biosensors market and their applications, considering all the biosensors technologies. According to their report the worldwide biosensors market is expected to grow with an annual growth rate of the 8% over the period of 2016 to 2024. The medical application leads by contributing with the 66% of the revenue contribution in 2015 and will collect noticeable revenue over the years ahead. Among the different biosensing technologies, the electrochemical ones are the fastest growing. Electrochemical transduction presents considerable advantages over other detection methods (thermal, piezoelectric or optical) which include low detection limits, compatibility with new microfabrication technologies, disposability, low cost, ease to operate, independence from sample turbidity, and minimal power requirements. The increasing demands for homecare and point-of-care, and initiatives undertaken by governments to shorten hospital stays, along with the possibility of cutting human and infrastructure

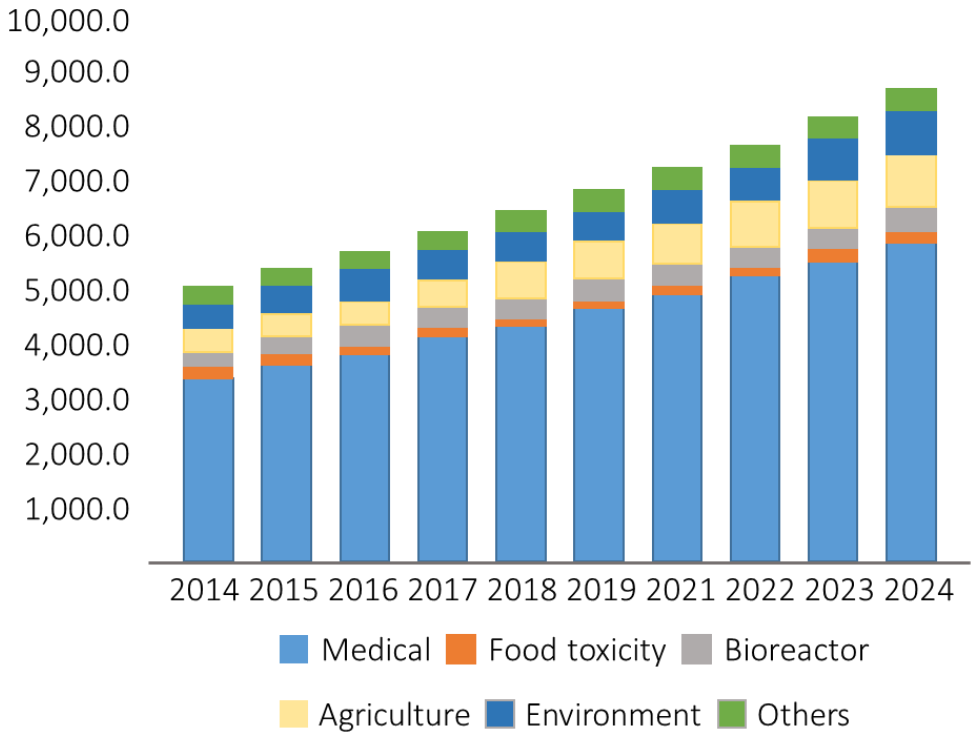

Figure 6.1. Worldwide biosensors market revenues divided by application.

resources, reducing samples processing before the assay and shortening the time for the response, are expected to drive the electrochemical Bio-FETs medical applications expansion.

CONTRIBUTIONS

Some of the results described in this thesis were achieved through productive discussions with collaborators. These people and their role in the contribution are mentioned below. Thanks to Dr. Cesar Pasucal García from the Luxembourg Institute of Science and Technology who provided inputs and guidance on a daily basis throughout all the work which is presented here, and to Dr. Wouter Olthuis from BIOS Lab on a Chip group in the University of Twente who contributed to the research with fruitful hints of thoughts, comments and suggestions.

Chapter 3

I would like to thank Dr. Dipti Rani from Luxembourg Institute of Science and Technology for contributing to the realization of this chapter content helping me during the experiments and supporting me during the paper writing. I also thank Dr. Renaud Leturcq from Luxembourg Institute of Science and Technology for thorough discussions and suggestions.

Chapter 4

Thank you to Dr. Dipti Rani for the help during the paper writing.

Chapter 5

I thank again Dr. Dipti Rani for the help during the experiments and the support during the paper writing.

SAMENVATTING

In dit proefschrift met de titel “A new design of an electrochemical (bio)sensor: high aspect ratio Fin-FET” stel ik een nieuw ontwerp van een elektrochemische sensor voor, gekenmerkt door een grote hoogte-breedte verhouding, geïntegreerd met high-k diëlektrische materialen. Ik verwijs naar deze sensoren als Fin-FETs. Het sensor ontwerp volgt op het modelleren van de elektrochemische omzetting van de lading aan het oxide sensor oppervlak in een verandering van de geleiding van een p-gedoteerd silicium kanaal, gestoeld op de Nernst en Poisson modellen, waarbij de oxidelaag en de laag die verarmd is van ladingsdragers beschouwd worden als twee capaciteiten in serie. Met deze theorie heb ik de afhankelijkheid vastgesteld van de breedte van de verarmde laag in de halfgeleider als functie van de dotering en de dikte, diëlektrische constante en oppervlaktereactiviteit van de diëlektrische laag. Ik laat onderzoeksresultaten zien van natte etssnelheden en etsprofielen van <110> georiënteerd p-gedoteerd silicium-op-isolator substraten afhankelijk van de maskeroriëntatie. Ik gebruik deze resultaten om een top-down vervaardigingsproces te ontwikkelen, gebruikmakend van gangbare cleanroom mogelijkheden zoals elektronenstraal- of laser lithografie om sensoren vorm te geven, en tevens TMAH/IPA gebaseerd chemisch etsen om de hoge aspect ratio te verkrijgen. De vervaardiging voorziet in reproduceerbare devices met uiteenlopende breedtes van 100 nm tot enkele micrometers. De insteek van het onderzoek aan de Fin-FETs is deze te beschouwen als pH sensor met siliciumoxide (SiO_2) als gevoelige laag. De resultaten tonen verbeteringen aan van de signaal/ruis verhouding, en van de lineariteit van de uitgangsstroom in vergelijking met nano pH-sensors, terwijl deze dezelfde footprint hebben. We rekenen dit toe aan de afmetingen van het kanaal, waar de verarming van de ladingsdragers in de halfgeleider ten gevolge van de lading aan het diëlektrische oppervlak de geleidbaarheid voornamelijk beïnvloedt via de breedte van het kanaal en nauwelijks via de hoogte. Tevens kan het toegenomen oppervlak van het kanaal de betrouwbaarheid met betrekking tot vervaardiging en

functionalisatie met bioreceptors verbeteren. Ik heb de afhankelijkheid van de responsetijd op protonconcentratie onderzocht als benodigde tijd om een stabiel signaal te verkrijgen. Tevens heb ik theoretisch de tijd berekend, die de sensoren nodig hebben om dezelfde concentratie aan biomoleculen zoals DNA of eiwitten te meten. Het resultaat van deze berekeningen toont aan dat de Fin-FET de responsetijd van nanosensors benadert bij lage concentratie van het analiet, wat we toerekenen aan 2D diffusie. Ik heb verscheidene diëlektrische materialen getest als pH-gevoelige laag, zoals aluminiumoxide (Al_2O_3) en hafniumoxide (HfO_2). Hun pH gevoeligheid koppel ik aan materiaaleigenschappen als reactiviteit en oppervlaktedichtheid van de groepen. Al_2O_3 en HfO_2 laten een hogere pH gevoeligheid zien dan siliciumoxide, wat we toeschrijven aan de hogere buffercapaciteit. Ook is de lineariteit beter ten gevolge van een verschillend point of zero charge. Ik vergelijk de eigenschappen van het Fin-FET/HfO_2 systeem met dat van het Fin-FET/SiO_2 systeem. Het Fin-FET/HfO_2 systeem laat de beste prestaties zien wat betreft uitgangsstroom versus protonconcentratie lettend op lineariteit en signaal/ruisverhouding, hetgeen het werkgebied van de sensor verbetert. HfO_2 verbetert tevens de transconductantie via de hogere diëlektrische constante en biedt voorts goede chemische stabiliteit.

Concluderend geloven wij dat de combinatie van high aspect ratio Fin-FET, die een grote stroom, intrinsieke lineariteit van het uitgangssignaal, betrouwbare manier van vervaardiging en functionalisatie oplevert, en die samen met goed presterende materialen als HfO_2 dat de transconductantie, oppervlakte gevoeligheid en chemische stabiliteit verbetert, het beste compromis biedt voor een Bio-FET ten aanzien van betrouwbaarheid, gevoeligheid, werkgebied en responsetijd, en bovendien label-free sensing biedt met de mogelijkheid van multiplexen.

APPENDIX

List of Symbols

α	Nernstian sensitivity parameter
a_{H+}	Proton activity
β_{int}	Intrinsic buffer capacity ($C/(m^2 \cdot pH)$)
C	Molar concentration (M)
C_D	Capacitance per unit area of the depleted region in the silicon (F/m^2)
C_{DL}	Capacitance per unit area of the electrical double layer in the electrolyte (F/m^2)
C_{diff}	Capacitance per unit area of the diffuse layer in the electrolyte (F/m^2)
C_{ox}	Capacitance per unit area of the oxide (F/m^2)
C_{St}	Capacitance per unit area of the Stern layer at the oxide/electrolyte interface (F/m^2)
D	Diffusion constant pf protons/molecules (m^2/s)
ε_{eff}	Effective dielectric constant of the SiO2/HfO_2 stack
ε_{ox}	Effective dielectric constant of the oxide
ε_{Si}	Effective dielectric constant of silicon
ε_w	Relative permittivity of water
ε_0	Vacuum permittivity (F/m)
ϕ_F	Fermi level in the semiconductor (eV)
ϕ_{Si}	Silicon electron work function (eV)
G	Electric conductance (S)

h	Height of the device (m)
I_{ds}	Source drain current (A)
k	Boltzmann constant (eV/K)
K_a, K_b	Acidic/basic dissociation constant of the oxide surface reactive groups
L	Length of the device (m)
μ	Mobility of electrons in the semiconductor ($m^2/V{\cdot}s$)
N	Number of molecules
N_A	Doping density of the semiconductor ($(cm^3)^{-1}$)
n^0	Number concentration of each ion in the electrolyte (M)
pH_B	Bulk pH of the electrolyte
pH_{zc}	pH of zero charge of the oxide
q	Electron elementary charge (C)
Q_D	Fixed charges in the depletion region of the semiconductor (C/m^2)
Q_{ox}	Fixed charge in the oxide (C/m^2)
Q_{ss}	Fixed charges at the semiconductor/oxide interface (C/m^2)
S	Cross section available to conduction in the semiconductor (m^2)
σ	Conductivity (S/m)
t	Time needed to the sensor for steady state signal (sec)
T	Absolute temperature (K)
t_{ox}	Oxide thickness (m)
V	Diffusion volume of the molecules around the sensor (m^3)
V_{ds}	Source drain voltage (V)
V_{fg}	Front gate voltage (V)
V_{FB}	Flat band voltage (V)

V_{gs}	Source gate voltage (V)
V_{ref}	Reference electrode voltage (V)
V_t	Threshold voltage (V)
w	Width of the device (m)
W_D	Width of the depleted region in the semiconductor (m)
χ_{sol}	Surface dipole potential of the electrolyte at the oxide (V)
Ψ_s	Potential at the semiconductor/oxide interface (V)
Ψ_0	Potential at the oxide/electrolyte interface (V)

ACKNOWLEDGEMENTS

Thanks to the FNR for funding the NANOpH project under the Attract program, fellowship number 5718158 NANOpH.

I would like to also acknowledge the people who contributed to the realization of this work by supporting me both professionally and personally. First I would like to thank my PhD supervisor at the Luxembourg Institute of Science and Technology (LIST), Dr. Cesar Pascual García for having chosen myself as his student and for believing in me and my capability to accomplish the goals. He guided me daily, putting me in front of my flaws and teaching me how to be scientifically curious and be a deep searcher to be able to explain science with simple words, like "if you have to explain it to your grandma". He thought me persistence, patience, resilience and how to be independent in my work managing tasks and time. Definitely after this PhD experience under his guidance I feel like a grown person both scientifically and personally.

I am also very grateful to Dr. Wouter Olthuis from the University of Twente, for making me feel his support throughout the years of the PhD, even in the toughest times, and for encouraging me. He was always an inspiration for scientific discussions which kept me interested and motivated. His kindness and belief in me kept my enthusiasm for accomplishing the goals. I also thank the promotor of the thesis Prof. Dr. Ir. Albert van den Berg from the University of Twente for believing in the project and make my work possible.

I thank the Director of the Materials and Technology research department at LIST Dr. Damien Lenoble, and all the engineers and researchers which supported me, especially at the beginning, introducing me to the knowledge needed to carry my job. Thanks to Kevin Menguelti, Stéphanie Girod, Noureddine Adjeroud, Renaud Leturcq, Mathieu Gerard, Oivier Bouton. They all contributed in some way to enriching my scientific background and making

things possible. Also thanks to the stuff of the IT department for their continuous availability.

I want to thank the members of the Nano Enabled Medicine and Cosmetic (NEMC) group in LIST to which I belonged. In particular I thank the group leader Dr. Sivashankar Krishnamoorthy for the continuous interest in my research and for the effort in carrying weekly meetings to share the most recent updates and promoting scientific presentations and interactions between the members.

A big thank you goes to the PostDoc researcher Dr. Dipti Rani who joined the project towards the end. She was a big support, personally encouraging me every day to be motivated in my work with her example of dedication. She also was a great support in the lab helping me with the fabrication and characterization of the sensors presented in this dissertation. Together we were able to speed up the work and get faster results.

I would like to thank all the other PhD students, old and new ones, with whom I shared the office. Among the old ones I especially thank David, Nohora, Alex. I had great time with them, talking about science as collegues and hanging out as friends. Special thank to Sunil for being an ever supporting colleague, a friend and a partner in life. Among the new ones thanks to Joao, Rishab, Matteo ,Thai, Sabrina and Divya for making office life like home. Thanks also to Dheeraj, a friendship born outside the working environment, for the nice time spent in Luxembourg and the deep discussione sbout life.

Finally I must thank all my family back to Italy, my mum and sister especially, for knowing each and every thing I have been through in these years and for supporting me always and give me strenght and love. Also I want to thank my italian colleagues from the time of the university Cinzia, Pasquale, Vitantonio, Valeria and Antonio. Even if we are far apart they were always part of my PhD life.

I am grateful that so many people were part of this journey and contributed somehow to the accomplishment of this work. At last I want to say a big thank you to myself too. I was my biggest supporter. The biggest strenght came from myself and my will of achieving what I was called for. I did my best throughout.

PUBLICATIONS LIST

Peer Reviewed Journal publications:

- S. Rollo, D. Rani, W. Olthuis, C. Pascual García, *Single step fabrication of Silicon resistors on SOI substrates used as Thermistors*, published in *Sci. Rep.*, 9, 2019, article number 2835

- S. Rollo, D. Rani, R. Leturcq, W. Olthuis, C. Pascual García, *High Aspect Ratio Fin-Ion Sensitive Field Effect Transistor: Compromises toward Better Electrochemical Biosensing*, published in *Nano Lett.*, 19 (5), 2019, 2879-2887

- S. Rollo, D. Rani, R. Leturcq, W. Olthuis, C. Pascual García, *High performance Fin-FET electrochemical sensors with high-K dielectric materials*, published in Sensors and Actuators: B Chemical (2019), arXiv identifier: 1907.11022

- S. Rollo, D. Rani, R. Leturcq, W. Olthuis, C. Pascual García, *The influence of geometry and other fundamental challenges for bio-sensing with Field Effect Transistors*, published in Biophysical Reviews (2019), doi:10.1007/s12551-019-00592-5

Contributions to conferences and Scientific Events:

- S. Rollo, N. Adjeroud, S. Girod, R. Leturcq, D. Lenoble, W. Olthuis, C. Pascual Garciá, *Nano-wires as wide range pH Sensors*, Micro and NanoSensors Summer School, DTU Copenhagen, 15th- 26th August 2016, poster presentation

- S. Rollo, N. Adjeroud, S. Girod, R. Leturcq, D. Lenoble, W. Olthuis, C. Pascual Garciá, *Nano-wires as wide range pH Sensors*, Mesa+ annual meeting,

Kinepolis, Colosseum 60, Enschede, 28th September 2016, poster presentation

- S. Rollo, N. Adjeroud, S. Girod, R. Leturcq, D. Lenoble, W. Olthuis, C. Pascual Garciá, *Nano-wires as wide range pH Sensors*, LIST PhD day, LIST, 8th December 2016, poster presentation

- S. Rollo, K. Menguelti, S. Girod, R. Leturcq, D. Lenoble, W. Olthuis, A. v.d. Berg, C. Pascual García, *Developing of Silicon Wires based pH sensors for integration in pH actuating devices*, LIST PhD day, LIST, 30th November 2017, poster presentation

- S. Rollo, Dipti Rani, W. Olthuis, C. Pascual García, Single Fabrication Process of Silicon Thermistors with different geometries on 110 SOI substrate, NANOTEXNOLOGY 2018, Thessaloniki, 3rd-6th July 2018, oral presentation

- S. Rollo, Dipti Rani, W. Olthuis, C. Pascual García, *Single Fabrication Process of Silicon Thermistors with different geometries on 110 SOI substrate*, LIST PhD day, LIST, 15th November 2018, poster presentation

- S. Rollo, Dipti Rani, C. Pascual García, granted NFFA proposal ID705 "Development and study of 3D Silicon Microwires Ion Sensitive Field-Effect Transistors", 3rd October 2018. Experiments carried out at the Centro Nacional de Microelectronica (CSIC-CNM), Bellaterra (Barcelona), 4th-8th February 2019.

- S. Rollo, Dipti Rani, C. Pascual García, *Customable one step fabrication method of silicon rectangular and triangular structures on SOI for sensing and bio-integration on chip*, Nanoengineering for Mechanobiology, Camogli, 24th-27th March 2019, poster presentation

- S. Rollo, My journey as a young researcher, event to promote science among teenagers “Chercheurs à l'école”, 29th March 2019, Luxembourg, Lycée Aline Mayrisch, oral presentation

- S. Rollo, D. Rani, R. Leturcq, W. Olthuis, C. Pascual García, *A high aspect ratio Fin-Ion Sensitive Field Effect Transistor: towards improved sensing capabilities for Lab on a Chip devices*, Lab-on-a-Chip & Microfluidics World Congress 2019, Coronado Island, California, 7th-9th October 2019, oral presentation